AN ABSTRACT OF THE DISSERTATION OF

Yu-Jen Chang for the degree of Doctor of Philosophy in Chemical Engineering presented on January 26, 2007.

Title: Investigation of Low Temperature Solution-based Deposition Process for Flexible Electronics

Abstract approved:

Chih-Hung Chang

The critical contribution of this dissertation is to provide a better understanding of the fundamental Chemical Bath Deposition (CBD) growth kinetic and mechanism for the well known II-VI semiconductor CdS using the newly developed continuous flow microreactor. This continuous flow microreactor provides the temporal resolution to control the homogeneous reaction of the chemical solution before it impinges on the substrate surface. This capability was used to decouple the homogeneous particle formation and deposition from the molecular level heterogeneous surface reaction to overcome the drawbacks associated with a conventional batch process. Transmission electron microscopy (TEM) analysis indicated an impinging flux without the formation of nanoparticles which could be obtained from this reactor in a short residence time. In addition, the reactor could be operated in a homogeneous particle formation regime. Size

increasing CdS nanoparticles grown by homogeneous reaction were clearly observed from TEM and SEM micrographs by increasing the residence time from 1 to 280 sec using pre-heated precursor solutions. The formation of CdS nanorod and arrayed nanorod bundle structures using the CBD recipe were also observed in some areas and reported here for the first time. The growth kinetics were studied using a particle-free flux. The deposition results suggest that HS^- ions formed through the thiourea hydrolysis reaction are the dominant sulfide ion source responsible for the CdS deposition rather than thioura itself that had been widely discussed in almost all of the previous literature. This finding could not be observed previously by a conventional CBD batch setup because all the reactant solutions were sequentially pulled into the reaction beaker and mixed all at once. An impinging flux without the formation of nanoparticles enables us to deposit extremely smooth and highly oriented nanocrystalline CdS semiconductor thin films at low temperature (80 ^{o}C). Enhancement-mode functional thin film transistors with an effective mobility of μ_{eff} =1.46 cm^2/V s, drain current on-to-off ratio of approximately 10^5 and turn-on voltage at 0 V were fabricated from the as-deposited films without any post annealing process. This microreactor could be adapted for the deposition of other compound semiconductor thin films such as highly transparent amorphous Indium Oxide (In_2O_3) thin films at low temperature (70 ^{o}C) using chemical solution deposition and opens a low-cost avenue to fabricate thin film flexible electronics on polymeric substrates.

Investigation of Low Temperature Solution-based Deposition Process for Flexible Electronics

by

Yu-Jen Chang

A DISSERTATION

submitted to

Oregon State University

in partial fulfillment of
the requirements for the
degree of

Doctor of Philosophy

Presented January 26, 2007
Commencement June 2007

Doctor of Philosophy dissertation of Yu-Jen Chang presented on January 26, 2007.

APPROVED:

Major Professor, representing Chemical Engineering

Chair of the Department of Chemical Engineering

Dean of the Graduate School

I understand that my dissertation will become part of the permanent collection of Oregon State University libraries. My signature below authorizes release of my dissertation to any reader upon request.

Yu-Jen Chang, Author

ACKNOWLEDGEMENTS

I would like to sincerely express my truthful gratitude and the deepest appreciation to Dr. Chih-Hung Chang for the enormous support and guidance that he has given to me during the past six years. Several years ago, he gave me an opportunity to join his group after I had finished my masters degree from Columbia University, in New York in 2000. I greatly appreciate his endless creative ideas, suggestions, encouragement, enthusiasm and support during my graduate studies and while writing this dissertation at Oregon State University, in Corvallis, Oregon. With his hard work, I was able to work on various projects funded through the Intel Corporation, the National Science Foundation, and the Hewlett Packard Corporation and was able to disseminate my research through several published journal papers, national and international conference presentations, and patent applications.

In addition, he has often invited me and other group members to have a cup of coffee or a beer, to join activities at his church, and even have dinner with his family. For me, he is not only an advisor, but also more like an elder brother or a family member.

I would also like to extend my appreciation to my PhD committee members: Dr. Shoichi Kimura, Dr. Goran Jovanovic, Dr. Sivaramakrishnan Subramanian, and Dr. Kaichang Li for their time and commitment to my PhD

program and to the other professors and staff in the Department of Chemical Engineering for their direct and indirect support.

I also would like to thank Dr. Gregory S. Herman, Dr. David T. Punsalan from Hewlett Packard Corporation, Dr. John F. Wager from the ECE department, Dr. Douglas A. Keszler from the chemistry department, and Dr. Janet Tate from the physics department for their suggestions and support in my research and for allowing me to use their facilities while I worked on the HP project. I am grateful to the past and present members of Chang's Group, Wager's Group, Keszler's Group, Tate's Group, and Paul's Group from the IME department for their valuable discussions and hands-on help with my experimental work, and for the technical support that I received from Nick Wannemacher, Andy Brickman, Chris Tasker and Manfred Dittrich.

Special thanks are due to: Dr. S. O. Ryu and Dr. T.-J. Lee from Yeungnam University in South Korea for their useful discussions to make many of my research publications become possible; Dr. Chunfei Li from Portland State University for his valuable assistance in the SEM and TEM measurements; Dr Philip Watson from the OSU chemistry department for his kindly assistance with the AFM measurements; and Dr. Augusto A. Morrone for his timely assistance with the TEM measurements.

Finally, I would like to express the deepest appreciation and sincere gratitude to my father, Chin-Kun Chang, mother, Lu-Chuan Cheng, and brother, Yu-Wen Chang; Dr. Wen-Yi Chen, Yu-Hui Lin, and Lisa Brutcher, my three

closet friends here at OSU, and many others for their endless love, support and encouragement during all these years of my education.

I have had a wonderful time here at Oregon State University, and I have lots of great memories from this quiet, organized, and lovely Corvallis campus. OSU will be remembered and cherished forever through out my whole life.

TABLE OF CONTENTS

TABLE OF CONTENTS (Continued)

TABLE OF CONTENTS (Continued)

LIST OF FIGURES

LIST OF FIGURES (Continued)

LIST OF FIGURES (Continued)

LIST OF FIGURES (Continued)

LIST OF FIGURES (Continued)

LIST OF FIGURES (Continued)

LIST OF TABLES

LIST OF APPENDICES

LIST OF APPENDIX FIGURES

LIST OF APPENDIX TABLES

DEDICATION

To my parents Chin-Kun Chang and Lu-Chuan Cheng

and

my brother Yu-Wen Chang

for their infinite love, support, and encouragement.

Investigation of Low Temperature Solution-based Deposition Process for Flexible Electronics

CHAPTER 1

INTRODUCTION

In recent years, flexible electronics [1-3] has dramatically received people's attention owing to its many potential applications, including its light-weight, low-cost, ability to flex, bend, curve, roll and fold or even wear for extreme portability for our daily use consumer electronics such as flat-panel displays for laptops, cell phones, and personal data assistant (PDA). In order to meet the requirement for fabricating the electronic devices on flexible polymeric substrates such as polyethylene terephthalate (PET) or polyimide (Kapton), the necessity of using low-temperature processing that is compatible with the low melting temperature polymeric substrates for the sequential deposition of thin films is the key to achieving this goal.

Chemical solution deposition also called chemical bath deposition (CBD) is a solution-based technique for thin film deposition. It provides a simple and low-cost method to produce uniform, adherent, and reproducible large area thin films that are suitable for fabricating large area electronic devices [4,5]. It is also capable of producing nano-, microcrystalline or even epitaxial thin films [6,7]. Many compound semiconductors (II-VI, IV-VI, V-VI, I-III-VI) have been

deposited by CBD techniques, and these techniques are primarily used in the process of fabricating Cu(In, Ga) Se_2 and CdTe based thin film photovoltaics [8,9].

Recently, we have reported our progress in fabricating Cadmium Sulfide (CdS) thin film transistors (TFTs) using CBD to deposit CdS channel layers. Device characteristics of an enhancement-mode CdS metal insulator semiconductor field-effect transistor (MISFET) with a field-effect mobility of ~1.5 cm^2/V s, a threshold voltage of V_T ~14 V and a current on-to-off ratio of ~10^6 were achieved [4]. Though CBD has many advantages, it suffers from some major drawbacks. In the case of the batch CBD process, the heat needed for chemical reaction is supplied from the solution bath to the sample surface, resulting in both heterogeneous nucleation at the surface as well as homogeneous particle formation in the bath. Moreover, the unequal bath-to-surface volume used to form the desired thin film generates a lot of waste and creates defects in devices. For a better understanding and optimization of the CBD processes, it is necessary to find a method to de-couple the homogeneous particle formation and deposition from the molecular level heterogeneous surface reaction. We have developed a continuous flow microreactor to overcome the drawbacks associated with conventional chemical bath deposition and have implemented it for the deposition of CdS thin films [10]. This novel reactor provides the benefit of introducing a constant flux of reactant solutions to the system (a continuous process) through an interdigital micromixer (IMM) to achieve efficient mixing of the reactant streams in a short residence time that allows a temporal control over the homogeneous reaction of

the chemical bath solution before the solution impinges on the substrate. We have successfully created a reactant flux that is free of particles by controlling the residence time. Using this particle-free flux, we were able to promote molecule-by-molecule heterogeneous growth mechanism and prevent particle-by-particle growth. In this way, unwanted deposition on the walls of the vessels and homogeneous CdS particle formation in the chemical bath can be minimized. Furthermore, the continuous process has resulted in a minimization of waste production and led to more uniform films with negligible occurrence of pinholes. Uniform, smooth, and highly oriented nanocrystalline CdS semiconductor thin films were successfully deposited on oxidized silicon substrates at a low temperature (80 ^{o}C) using this microreactor. Functional thin film transistors-enhancement-mode CdS MISFET with an effective mobility of 1.46 cm^2/V s and a drain current on-to-off ratio of approximately 10^5 were fabricated from the as-deposited films without any post annealing process [10].

A CdS homogeneous particle formation growth study was performed by taking advantage of this novel continuous flow microreactor. Size increasing CdS nanoparticles grown by homogeneous reaction were clearly found from TEM and corresponding SEM micrographs by increasing the residence time from 1 to 280 sec. The formation of CdS nanorod and arrayed nanorod bundle structures using the CBD recipe were also observed in certain areas and reported here for the first time. This new approach could be adopted for synthesizing nano-sized particles and depositing other compound semiconductor thin films at low-temperatures

using solution-based chemistry [11]. Furthermore, reaction conditions can be optimized by independently changing the temperature of the solution and the substrate, reactant concentration (the total concentration of precursors in the solution), the concentration of precursors relative to one another, and the flow rate (residence time).

CdS thin film morphology was able to be controlled by altering the impinging fluxes by means of the residence time here and deposition time. Thin film deposited at a very short residence time (1 sec) showed a very low growth rate with no clear deposition observed at the short deposition time using the original recipe from the SEM characterizations. While using pre-mixed $SC(NH_2)_2$ and NH_4OH system, a clear deposition with higher growth rate was observed. The deposition results suggest that HS^- ions formed through the thiourea hydrolysis reaction are the dominant sulfide ion source responsible for the CdS deposition rather than thioura itself that had been widely discussed in almost all previous literature. These results suggest that the term of thiourea concentration in the rate equation of CdS thin film growth needs to be replaced by HS^- concentration. This finding can not be found previously by a conventional CBD batch setup since all the reactant solutions are sequentially pulled into the reaction beaker and mixed all at once. However, using our reactor, we were able to control the mixing elements and sequence based on the design of experiments which could not be achieved by the batch CBD process. Uniform, dense, and compact CdS thin films were able to

deposit on an oxidized silicon wafer at a low temperature (~80 ^{o}C) using this continuous flow microreactor at certain reaction conditions. Furthermore, the process could be adopted for the deposition of other compound semiconductor thin films at low temperatures using chemical solution deposition and thus open a new low-cost avenue for fabricating thin film flexible electronics on polymeric substrates.

Due to environmental safety issues, other cadmium free semiconductor materials using solution-based deposition process were carried out. A newly developed precursor solution was used to deposit highly transparent amorphous Indium Oxide (In_2O_3) thin films through a solution-based deposition process at low-temperature (~70 ^{o}C). Depletion-mode In_2O_3 metal–insulator-semiconductor field-effect transistors (MISFETs) with the field-effect mobility (μ_{FE}) as high as 18.71 and 2.23 cm^2/V s were obtained for devices with and without postannealing process performed in the air for 1 hour at 300 ^{o}C, respectively. This demonstrated a promising way that is capable of fabricating transparent flexible electronics on polyethylene terephthalate (PET) or polyimide (Kapton) polymeric substrates using the solution-processed Indium Oxide (In_2O_3) thin films as the active channel layers.

CHAPTER 2

LITERATURE REVIEW

2.1 Chemical Bath Deposition

Chemical bath deposition (CBD) also called chemical solution deposition (CSD) or simply called chemical deposition (CD) is a soft solution process that is capable of producing high-quality thin films at relatively low temperature (usually lower then 80 ^{o}C). It is possible to deposit the thin films from a reaction occurring in a solution on various substrates such as glass slides, metal plates, or flexible substrates (polymeric plastics, flexible glass and stainless steel sheet) for flexible electronic applications. It is an aqueous analogue to chemical vapor deposition (CVD) and the fundamental CBD growth mechanism is similar to that of a CVD process; it involves mass transport of reactants, adsorption, surface diffusion, reaction, desorption, nucleation and growth. CBD provides a simple, easy to setup and low-cost method to produce uniform, adherent, and reproducible large area thin films for thin film electronic applications such as solar cells (photovoltaic) and thin-film transistors (TFTs).

2.1.1 Previous Works

As early as 1835, chemical bath deposition (CBD) started to draw people's attention when Liebig reported the deposition of silver (the silver mirror deposition) using this solution-based technique [12]. After that, the first reported deposition of a compound semiconductor film is the formation of "lüsterfarben"

(lustrous colors) on metals from thiosulphate solutions of lead acetate, copper sulfate, and antimony tartrate which resulted in “splendid” colored films of PbS, CuS and SbS with interference colors resulting from various thicknesses of the deposited thin films [13]. Several years later, this study was moved on to an electrochemical mechanism for thiosulphate depositions either on the metal substrate (standard electrochemical potential) or on a contacting non-noble metal (internal electrochemical deposition) [14-16]. PbS is probably the example case for CD process from an electrochemical or mixed electrochemical/chemical mechanism. A wide range of depositions from thiosulphate solutions (both CD and electrochemical) were also reported [16].

In 1884, J. E. Reynolds reported the first application of the CBD process [17] to the deposition of PbS thin films for the application of photoconductive detectors. He used thiocarbamide as a source of sulfur, and it could be easily desulfurized by certain metallic oxides and hydroxides to form the corresponding sulfides. He observed that when thiocarbamide was heated in a basic solution of lead hydrate, lead sulfide separated in a galenoid form and got firmly attached as an adherent layer on the sides of the vessel. This can be traced as the first attempt to deposit a material on the surface of a substrate.

Infrared photoconductivity of CBD PbS films was reported nearly a century ago [18,19] and this application has led to the subsequent investigations in lead chalcogenide films. The CBD PbS and PbSe films for infrared photoconducting detectors were further developed during World War II. The CBD

is still the main technique for making commercial products compared to the vacuum evaporation process.

CBD was limited to PbS and PbSe films for a long period of time. In 1961, the deposition of CdS was reported by Mokrushin *et al*. [20]. Since then, CdS has become the most widely studied material in CBD. Later on, thiourea was replaced by its selenium analogues, for example selenourea and dimethylselenourea. This opened the avenue for fabricating a series of various selenide compounds with the first compound being PbSe [21]. An extensive review was completed by Chopra and his co-workers. They discussed about 20 different compounds synthesized by CBD, and this is the first actual general review for CBD that was reported [22].

More recently, Nair et al. [23] prepared CdS thin films of very high photoconductivity by controlling the molar ratios of Cd ions and thiourea. They observed that the films produced by the equimolar ratio were of low quality. Nair and Nair [24] had carried out deposition directly under sunlight using cadmium acetate and thiourea at room temperature. During the initial stages of deposition, they observed the increased solar radiation absorption that darkened the bath solution. This photothermal reaction in the bath increased the bath temperature and thus increased the rate of deposition. High quality films showing excellent optoelectronic properties were obtained.

Several years later, a review by Lokhande [25] was published with an emphasis on the deposition of metal chalcogenides that covered sulphides and selenides of many metals and oxides, and some ternary compounds were also

included. Ortega-Borges and Lincot [26,27] used Quartz Crystal Microbalance (QCM) to study the initial rate for the first time. They identified three main deposition regimes. The first one is an induction regime where the reaction rate is slow and not evident. The second one is the compact layer growth regime through the molecular heterogeneous surface reactions. The high quality and tightly adhering film is grown in this regime. The third one is the porous layer regime due to the colloidal settling and sticking on the substrate created by homogeneous particle formation. After this the growth rate will reach saturation due to limited reagent concentration. A detailed review of chemical solution deposition of various chalcogenides including binaries and ternaries of sulfide and selenide compounds was done by Lincot *et al.* in 1998 [28]. They have given us an extensive analysis of the basic aspects of deposition along with the growth kinetic mechanisms involving quartz crystal microbalance (QCM) and impedance measurements. Finally, they have described the epitaxial growth of various semiconductors. For example, CdS epitaxial thin films could be deposited on InP single crystals [29].

Chemical bath deposition received a major attention after it was shown that chemically deposited CdS films onto CdTe films could be used to make superior photovoltaic cells (PV) compared with the earlier evaporated CdS. The first successful application of CBD CdS films used in PV cells was reported by Uda *et al*. [30]. Later on, researchers demonstrated their work by making high efficiency $CuInSe_2$ [31,32] and CdTe [33,34] based thin film cells. Two more reviews by

Nair *et al*.[8] and Savadogo [9] on their extensive work in the field with an emphasis on solar energy related issues were also published. Nowadays, CdS layer is almost universally used on both CdTe and $CuInSe_2$ thin film PV cells.

Chemical bath deposition is capable of depositing nanocrystalline thin films through very small nanocrystals. These crystals or the so called quantum dots exhibit quantum confinement effects when they reach nano-sized dimension [35,36] and their optical bandgap increases with decreasing crystal size, for example, the well known CdSe nanocrystals [37]. Furthermore, the changes in optical spectra that occurred as a function of nanocrystal size provided the information on the different mechanisms of the deposition process for the first time ever reported [38].

2.1.2 Growth Mechanisms

During the mid 1960's, Kitaev and co-workers, a group of Russian researchers, did extensive work on thin film deposition of CdS films based on the PbS deposition technique [39] and proposed a growth mechanism taking into account the formation of colloidal particles and their subsequent adsorption on a surface. They suggested that a solid phase precipitate, e.g. $Cd(OH)_2$, must be present in the solution to provide the catalytic surface for thiourea decomposition and CdS films can only be produced in the presence of this solid phase.

After that, Kitaev *et al* suggested the possibility of an alternative to the classical mechanism for CdS thin film formation. This alternative mechanism

involves the formation and adsorption of intermediate species on the substrate surface which was supported by quantum mechanical calculations [40] and radiochemical experiments [41]. However, the nature of the intermediate species mentioned was not clearly revealed by these experiments.

After a few years, Kaur *et al.* [42] studied the kinetics of CdS growth from alkaline solution. On the contrary, they found that $Cd(OH)_2$ was not necessary to obtain CdS films and believed that the thin films growth could take place either by ion-by-ion condensation of free Cd^{2+} and S^{2-} ions or by adsorption of colloidal particles of CdS formed in the bath, depending on the various deposition parameters and method of precipitation. They also mentioned that thin films growth by an ion-by-ion growth mechanism accounts for the thin, hard, adherent, and specularly reflecting films; however, the colloidal growth is responsible for the thick, powdery and diffusely reflecting films. The main results of their study were that the films prepared in the presence of $Cd(OH)_2$ in the solution were physically coherent and adherent and that vigorous stirring of the solution would decrease the powdery nature of films and increase adhesion. They also concluded that the higher deposition rate would generally result in lower terminal thickness.

According to their mechanism, first, free Cd^{2+} forms due to the dissociation reaction, where other Cd salt such as $Cd(NO_3)_2$, $Cd(CH_3COO)_2$, or $CdCl_2$ can also be used:

$$CdSO_4 \rightarrow Cd^{2+} + SO_4^{2-} \qquad [2.1]$$

In the presence of ammonium hydroxide, the following equilibrium reaction between ammonia and ammonium ion takes place:

$$NH_4^+ + OH^- \longleftrightarrow NH_3 + H_2O \quad [2.2]$$

Cd ion then complexes with ammonia, thus controlling the concentration of free cadmium ions:

$$Cd^{2+} + nNH_3 \longleftrightarrow Cd(NH_3)_n^{2+} \quad [2.3]$$

The coordination number of cadmium ion-ammonia complexes (n) ranges from 1 to 6. Where $Cd(NH_3)_4^{2+}$ is the dominant complex species, according to the highest values of the stability constants among the 6 coordination number [43].

The following reactions show the hydrolysis of thiourea, releasing free sulfide ions:

$$SC(NH_2)_2 + OH^- \longrightarrow HS^- + CN_2H_2 + H_2O \quad [2.4]$$

$$HS^- + OH^- \longleftrightarrow S^{2-} + H_2O \quad [2.5]$$

Free cadmium ions then react with free sulfide ions to form CdS:

$$Cd^{2+} + S^{2-} \longrightarrow CdS\ (s) \qquad [2.6]$$

When the ionic product exceeds the solubility product of CdS (~ 10^{-25}), the reaction of free cadmium ions and sulfide ions can occur in the bulk of the solution as colloids (homogeneous nucleation and particle formation) or at the surface of the substrate as film (ion-by-ion process).

Later, Lincot *et al* [26] for the first time used combined in situ quartz crystal microbalance (QCM) and electrochemical impedance techniques to study the chemical bath deposition of CdS layers. The important results about the covering properties of the film, its internal structure, and the evolution of this structure during the growth were clearly explained. Based on their results the film is shown to have a duplex structure with an inner compact layer (measured by capacitance) and an outer porous layer growing at longer reaction times. Also, having excess thiourea is found to be favorable for obtaining total coverage of the substrate with minimum thickness of CdS films.

Following the previous mentioned study made by Kitaev *et al*, Ortega-Borges & Lincot [27] proposed the first approach to the nature of intermediate species from growth kinetic study based on initial rate studies using a QCM and identified three main deposition regimes:

1. The induction regime

2. The coalescence and compact layer growth regime

3. The porous layer growth regime

The first one is an induction regime where the reaction rate is slow and no clear deposition is observed. This regime corresponds to short reaction times and is marked by the beginning of nucleation. The second one is the compact layer growth regime through the molecular heterogeneous surface reactions. The high quality and tightly adhering film is grown in this regime. When the growth process begins, it is characterized by a linear variation and any minute deviation in this process can be attributed to a coalescence period. The third one is the porous layer growth regime. When the reaction time gradually increased, a clear increase in the growth rate could be observed which corresponded to the growth of a porous layer. The appearance of this porous layer was due to the colloidal settling and sticking on the substrate created by homogeneous particle formation. However, this layer, unlike those compact layer, was weakly bonded to the substrate surface and hence could be removed easily either by sonication using ultrasonic bath or mechanical rubbing. After this, the growth rate would reach saturation and eventually stop due to the limited reagent concentration.

Based on those observations, Ortega-Borges *et al*. [27] proposed the global reaction for CdS deposition:

$$Cd(NH_3)_4^{2+} + SC(NH_2)_2 + 2OH^- \longrightarrow CdS + CH_2N_2 + 4NH_3 + 2H_2O \quad [2.7]$$

By performing initial rate studies using the QCM, they arrived at the following empirical rate equation:

$$r(\mu m/h) = K\frac{[Cd]^{0.6}[SC(NH_2)_2]^{0.8}}{[NH_3]^{3.3}[H^+]^{1.5}} \quad [2.8]$$

with $K = 10^{-14.7}$

Based on the above rate equation, they proposed a 3 step molecular level heterogeneous reaction mechanism given in equations 2.9 to 2.11.

1. Reversible adsorption of cadmium hydroxide species:

$$Cd(NH_3)_4^{2+} + 2OH^- + Site \xleftrightarrow{k_1, k_{-1}} Cd(OH)_{2ads} + 4NH_3 \quad [2.9]$$

2. Formation of a surface complex with thiourea:

$$Cd(OH)_{2ads} + SC(NH_2)_2 \xrightarrow{k_2} [Cd(SC(NH_2)_2)(OH)_2]^*_{ads} \quad [2.10]$$

3. Formation of CdS with site regeneration:

$$[Cd(SC(NH_2)_2)(OH)_2]^*_{ads} \xrightarrow{k_3} CdS + CN_2H_2 + 2H_2O + site \quad [2.11]$$

They assumed step 3, the decomposition of metastable intermediate complex, as the rate limiting step and the number of surface sites were constant and all other previous steps were in quasi-equilibrium, they then derived the following equation for growth rate:

$$r = \frac{k_1 k_2 [OH^-]^2 [Cd(NH_3)_4^{2+}][SC(NH_2)_2]}{k_{-1}[NH_3]^4 + k_1[OH^-]^2[Cd(NH_3)_4^{2+}] + k_2[SC(NH_2)_2] + \frac{k_1 k_2}{k_3}[OH^-]^2[Cd(NH_3)_4^{2+}][SC(NH_2)_2]} \quad [2.12]$$

A few years later, Doña and Herrero [44] modified the CBD CdS reaction mechanism based on previous proposed rate law by Ortega-Borges *et al*. [27]. They suggested the formation of an adsorbed dihydroxo-diammino cadimium complex, a different intermediate species on the surface instead of cadmium hydroxide. They arrived at the following experimental growth rate equation using initial rate studies:

$$r = \frac{K(T)[CdSO_4]^{0.9}[SC(NH_2)_2]^{1.1}[OH^-]^{1.7}}{[NH_3]^{1.8}} \quad [2.13]$$

According to the experimental growth rate equation, a modified reaction mechanism is given in equations 2.14 to 2.16.

1. Reversible adsorption of dihydroxo-diammino-cadmium complex:

$$Cd(NH_3)_4^{2+} + 2OH^- + site \xleftrightarrow{k_1, k_{-1}} [Cd(OH)_2(NH_3)_2]_{ads} + 2NH_3 \quad [2.14]$$

2. Adsorption of thiourea by formation of an intermediate metastable complex:

$$[Cd(OH)_2(NH_3)_2]_{ads} + SC(NH_2)_2 \xrightarrow{k_2} [Cd(OH)_2(NH_3)_2\ SC(NH_2)_2]^*_{ads} \quad [2.15]$$

3. Formation of CdS and site regeneration by the intermediate metastable complex decomposition:

$$[Cd(OH)_2(NH_3)_2\ SC(NH_2)_2]^*_{ads} \xrightarrow{k_3} CdS + CN_3H_5 + NH_3 + 2H_2O + site \quad [2.16]$$

This reaction, step 3, is considered the rate-limiting step in the mechanism. Based on this equation, they yielded the following theoretical growth rate equation for the mechanism:

$$r = \frac{k_1 k_2 C_s [Cd(NH_3)_4^{2+}][SC(NH_2)_2][OH^-]^2}{k_{-1}[NH_3]^2 + k_1[OH^-]^2[Cd(NH_3)_4^{2+}] + k_2[SC(NH_2)_2] + \frac{k_1 k_2}{k_3}[OH^-]^2[Cd(NH_3)_4^{2+}][SC(NH_2)_2]} \quad [2.17]$$

where C_s is the concentration of sites in the substrate surface.

This equation is almost identical to the one derived from the mechanism proposed by Ortega-Borges *et al*. shown in equation 2.12, the only difference being the exponent for the ammonia concentration, the exponent changes from 4 to

2 for this modified one. The rate law can be further simplified using the order of magnitude analysis for the solution with high ammonia concentration to obtain the following equation:

$$r = \frac{k_1 k_2 C_s [CdSO_4][SC(NH_2)_2][OH^-]^2}{k_{-1}[NH_3]^2} \qquad [2.18]$$

This equation is very similar to the experimental growth rate equation, which supports their theoretical mechanism.

For a long period of time, CBD was studied mainly focused on thin film deposition process, thin film characterizations, growth mechanisms, and its application of photovoltaic cells. However, as a study from an engineering point of view, the mathematical model simulation had still not been fully conducted.

Recently, Nair *et al*. [45] attempted to provide a mathematical model in order to simulate the growth of compound semiconductor thin films via CBD process. They identified three different stages in the CBD growth process: nucleation phase, growth phase, and terminal phase. Each of these phases depends on concentration of ions in the deposition bath, the deposition temperature, and the dissociation constants of metal complex ions. They showed that the proposed mathematical model could qualitatively account for most of the experimental growth curves with their experimental conditions for chemically deposited semiconductor thin films.

A year later, Kostoglou *et al* [46,47] reported a detailed and comprehensive mathematical model for the CBD CdS process. This model includes the rate of (a) nucleation, (b) particle growth, (c) coagulation and (d) particulate deposition in addition to the molecule-by-molecule film growth. The nucleation was modeled based on the classical theory of nucleation [48] as:

$$\alpha = \frac{1}{6}\pi\left(\frac{4V_m\sigma}{nRT\ln(s)}\right)^3 \qquad [2.19]$$

where α is the size of the stable nucleus, V_m is the molecular volume of CdS, σ is the interfacial tension, R is the ideal gas constant, T is the temperature, and S is the supersaturation.

Unlike other works, the modeling took into account the dependence of critical size on supersaturation. They used a simplified version of this model to compare with the experimental growth curves reported by Doña and Herrero [44]. This simplified model assumed the nucleation occurred instantaneously instead of the continuous one at a supersaturation point. Thus, there would be no particle formation before this point in the system and the film growth would slow down and eventually stop after this point by neglecting the film growth due to particle

formation. A good agreement between the experimental data and the values from the simplified model was obtained.

Based on the results from Carbonell and Riley's work [49], they modeled particle deposition as:

$$D(x) = \frac{0.3 D_p^{2/3} u_\infty^{1/2}}{W_d v^{1/6} L^{1/2}} \qquad [2.20]$$

where D_p is the diffusivity of particles of volume x, v is the kinematic viscosity of the solution, u is the characteristic velocity of the fluid, L is the characteristic length of the submerged surface and W_d is the stability ratio for particulate deposition.

They performed a comprehensive model analysis, and their preliminary calculations indicated that the resulting thickness of particulate deposition for the deposition stability ratio of W_d=1 is 2 orders of magnitude larger than the thickness contributed by ionic type deposition.

More recently, Kostoglou *et al* [50] suggested that initial nuclei are continuously generated on the substrate and grow as discrete "surface" particles. For a certain period of time, these particles tend to coalesce with their neighboring ones, while new nuclei keep forming and growing, resulting to the formation of coherent films based on the SEM micrographs of deposits formed through the

steady flow of the supersaturated solution with respect to CdS. A simple model which was capable of predicting the temporal thickness evolution including the "induction period" was developed. Where two cases of the growth pattern were conducted: one based on instantaneous surface nucleation (due to its simplicity), another with a constant surface nucleation rate that later appeared to be closer to the experimental observations.

Voss *et al*. [5] studied CBD CdS growth kinetics using QCM. They observed that the film growth could be limited at certain concentrations and temperatures (mass transport limited reaction) and the deposition rate and terminal thickness were strongly dependent on the stirring rate. Four distinct growth regimes were identified. An induction regime was following by a compact layer growth regime then transformed into a porous layer growth regime clearly observed by a "kink" in the growth curve. The final regime, the depletion regime, was a result of the depletion of the reactants and the film growth rate slowed down and eventually stopped. The ex-situ atomic absorption (AA) measurements indicated that the total Cd concentration in the solution changed dramatically in the linear growth regime with a constant deposition rate. One possible explanation was that the linear growth regime is actually a combination of molecule-by-molecule (ion-by-ion) and cluster-by-cluster growth mode. This hypothesis was further supported by real time dynamic light scattering and transmission electron microscopy measurements.

A schematic diagram that illustrates the CBD CdS growth mechanism based on our current understanding [27,46] is given in Figure 2.1. There are two major competing reactions in a CBD CdS growth process: homogeneous particle formation and heterogeneous surface reaction [46]. In the bulk, an alkaline solution consisting of ammonium hydroxide provides ammonia in the solution. The cadmium salt, such as $CdCl_2$, produces free cadmium ions, Cd^{2+}, through a dissociation reaction. The cadmium ions then complexes with ammonia to form the dominant tetra-ammino-cadmium complex ion, $Cd(NH_3)_4^{2+}$, controlling the concentration of free cadmium ions. Thiourea releases free sulfide ions through an equilibrium hydrolysis reaction. Free cadmium ions then react with free sulfide ions to form CdS particles in the bulk solution. On the surface, the tetra-ammino-cadmium complex ions react with hydroxide ions to form adsorbed cadmium hydroxide species, $[Cd(OH)_2]_{ads}$ on the surface. This adsorbed species then reacts with thiourea through a Rideal-Eley growth mechanism to form an adsorbed metastable complex, $[Cd(SC(NH_2)_2)(OH)_2]_{ads.}$ Finally, CdS is formed and a new surface site is regenerated through decomposition of the adsorbed metastable complex.

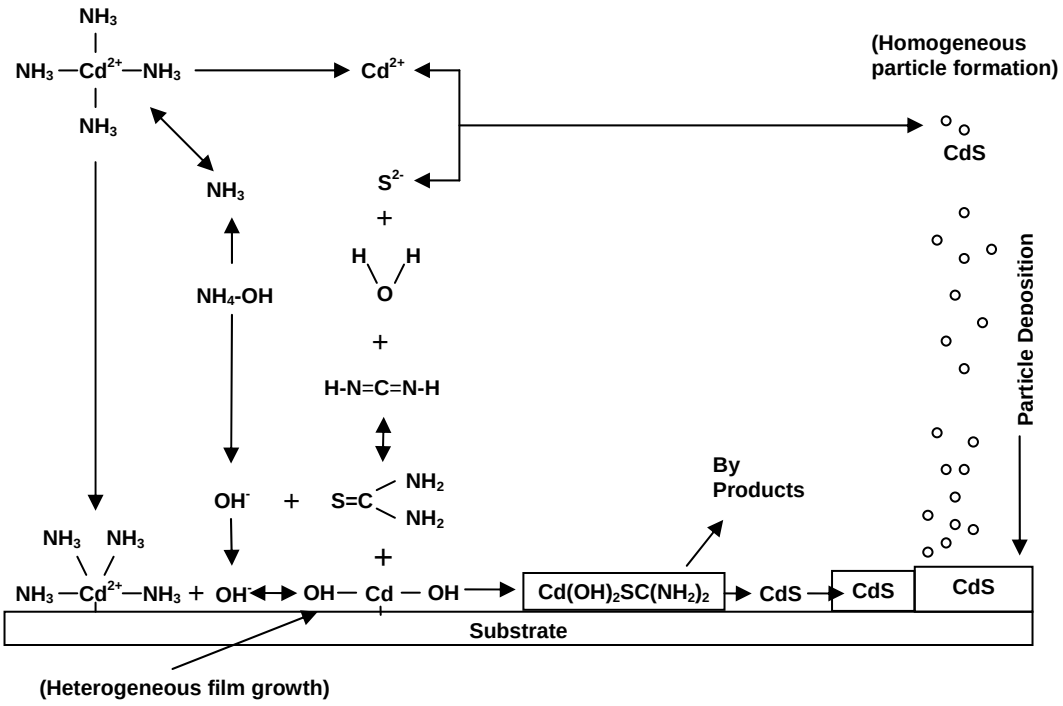

Figure 2.1 Schematic diagram of CBD CdS growth mechanism.

2.2 CdS MISFETs

CdS metal insulator semiconductor field-effect transistors (MISFETs) have been developed since the early 1960's. Vacuum evaporated CdS thin film is the major deposition method to prepare the active channel layer. Weimer [51] proposed the first successful vacuum-deposited field-effect transistor using CdS as the semiconductor in 1961. After that, CdS thin films deposited by CBD have been widely studied and primarily used as the window for thin-film solar cells and photovoltaic applications. Fabrication of thin-film transistors using CBD CdS thin films, however, still remains limited to date and only few literatures are reported.

2.2.1 Theoretical Background

A number of thin film transistor structures can be fabricated according to the position of the channel layer, gate insulator, and source/drain electrodes. A staggered TFT has the gate and source/drain electrodes on the opposite sides of the semiconductor with either gate electrodes on the top or bottom. (top-gate or bottom-gate structure). A coplanar TFT has the gate and source/drain electrodes on the same sides of the semiconductor also with either gate electrodes on the top or bottom. The inverted-staggered (or bottom-gate staggered) TFT is widely used in the manufacturing of Active-Matrix Liquid Crystal Display panels (AMLCD).

Figure 2.2 shows the two operational regimes for TFTs: triode (pre-pinch-off) regime and saturation (post-pinch-off) regime. At the very beginning, when gate voltage (V_G) is less than threshold voltage (V_T) (the minimum required gate voltage to induce a channel layer to let electrons move from the source side to the drain side or turn on the device), no drain current (I_D) is created. The drain current will increase when drain and gate voltage (V_D and V_G) continuing to increase. When $V_D = V_G - V_T$, the electron channel becomes completely pinched-off, and $V_D = V_{Dsat.}$ The drain current will saturate, when $V_D > V_G - V_{T.}$ In the triode regime, when drain voltage much smaller than gate voltage minus threshold voltage ($V_D << V_G - V_T$), the drain current will increase linearly with increasing drain voltage (linear region). On the other hand, the drain current is constant with increasing drain voltage for the saturation regime.

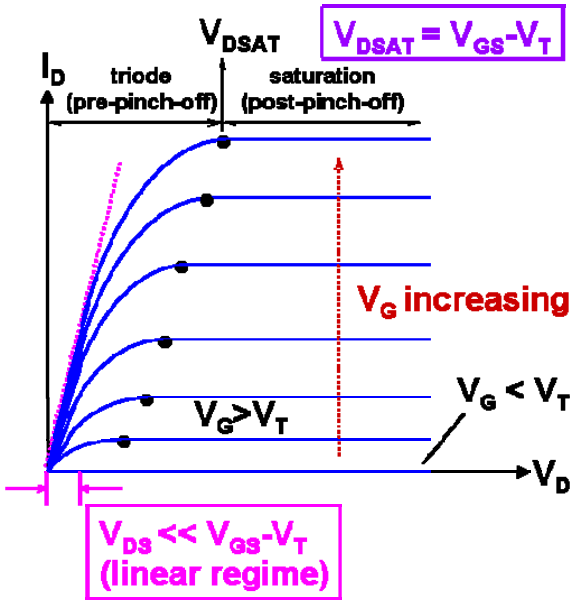

Figure 2.2 A typical TFTs I-V characteristics including two operational regimes: triode (pre-pinch-off) region and saturation (post-pinch-off) region.

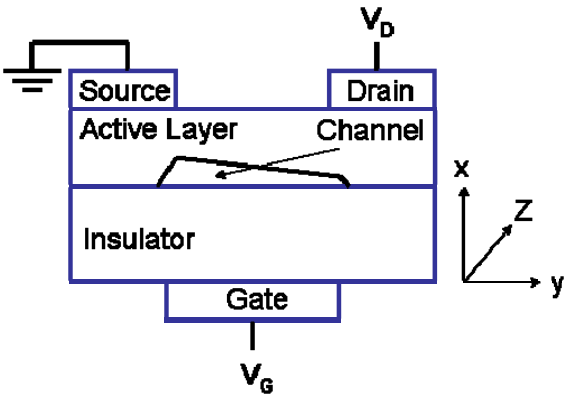

Figure 2.3 Schematic cross-sectional view of a TFT structure used to derive the gradual channel approximation.

A gradual channel approximation is assumed in the active layer (channel) of TFT. Figure 2.3 shows a schematic cross-sectional view of a TFT structure used to

derive the gradual channel approximation where x is the direction perpendicular to the active layer and y is parallel to the channel. The carrier density per unit area in the channel depends on the potential V(y) caused by the drain potential [52]. When the gate potential is higher than the threshold voltage, the mobile charge Q_I in the channel is related to the gate potential V_G [53].

$$Q_I = -C_{ins}(V_G - V_T) \qquad [2.21]$$

where C_{ins} is the gate insulator capacitance per unit area, $C_{ins} = \frac{\varepsilon_{ins} \times \varepsilon_o}{t_{ins}}$, ε_{ins} is the gate insulator dielectric constant, ε_0 is the permittivity of free space, and t_{ins} is the thickness of the gate insulator.

Since the induced mobile charge Q_I is a function of y, equation 2.21 is replaced by the following equation.

$$Q_I = -C_{ins}(V_G - V_T - V) \qquad [2.22]$$

Within the conducting channel the current flow is almost exclusively in the y-direction. The diffusion term (the second term on the right side) has been taken to be negligible from the current density formula.

$$J_n = \frac{I_n}{A} = q(\mu_n nE + D_n \frac{dn}{dx}) \qquad [2.23]$$

where J_n is the electron current density, I_n is the electron current, q is the electronic charge, μ_n is the electron mobility, n is the electron carrier concentration, E is the electric field, D_n is the electron diffusion coefficient.

The current passing through any cross-sectional plane within the channel will equal to I_D.

By integration of the current density from x=0 to channel thickness, and z=0 to channel width, W.

$$I_D = \iint J_n dxdz = W\mu_n Q_I E_y \qquad [2.24]$$

By substituting electrical field in y-direction, $E_y = -dV/dy$, and equation 2.22 into equation 2.24, we can obtain

$$I_D dy = W\mu_n C_{ins}(V_G - V_T - V)dV \qquad [2.25]$$

By integration of the current incremental from y=0 to L and from V=0 to V_D, the gradual channel approximation from the drain current can be obtained.

$$I_D = \frac{W}{L} C_{ins} \mu_n \left[(V_G - V_T) V_D - \frac{1}{2} V_D{}^2 \right] \quad [2.26]$$

In the linear region, $V_D << V_G - V_T$, the drain current can be written as

$$I_D = \frac{W}{L} C_{ins} \mu_n \left[(V_G - V_T) V_D \right] \quad [2.27]$$

In the saturation region, the saturation drain current can be obtained by substituting $V_D = V_G - V_T$ into equation 2.26 and yield:

$$I_D = \frac{W}{2L} C_{ins} \mu_n (V_G - V_T)^2 \quad [2.28]$$

For the TFTs device characterization, the drain current - drain voltage (I_{DS} - V_{DS}) characteristics (output characteristics) is the most common characterization for TFT devices. For a working device, the drain current will increase as increasing drain voltage and applied gate voltage causing gate-modulated transistor behavior to be obtained.

The threshold voltage is the minimum required gate voltage to produce a conductive channel, thereby enabling carriers to flow from source to drain. The threshold voltage for TFT device is approximated using a linear extrapolation

method with the drain current measured as a function of gate voltage (I_{DS} vs. V_{GS} plot) at a low V_{DS} (usually applied V_{DS}= 1 V) to ensure operation in the linear region. For *n*-type semiconductor material, with a positive threshold voltage, this device behaves as an enhancement-mode device that is initially off and requires a positive gate voltage to allow current to flow. With a negative threshold voltage, this device behaves as a depletion-mode device that is initially on and requires a negative gate voltage to turn off the device.

However, the precise identification of the threshold voltage to determine the device operation-mode (either enhancement or depletion-mode) is still somewhat ambiguous [54,55]. A more accurate and less ambiguous parameter for device characterization used here is turn-on voltage, the gate voltage at the onset of the initial sharp increases in drain current in a $\log(I_{DS})$-V_{GS} transfer characteristic [54]. With a positive turn-on voltage, this device behaves as an enhancement-mode device and a negative one indicating a depletion-mode device is obtained.

The drain current on-to-off ratio (transfer characteristics) determines the switching quality of the MISFET. It can be obtained by plotting $\log(I_{DS})$ versus V_{GS} at V_{DS} = 40 V.

The mobility of a MISFET refers to the carrier mobility that is proportional to the carrier velocity in an electric field [56]. This is the most often used parameter for determining the device performance. There are three different

mobilities usually used: field-effect mobility (μ_{FE}), effective mobility (μ_{eff}), and saturated mobility (μ_{sat}).

1. The field-effect mobility (μ_{FE}), $\mu_{FE} = \dfrac{g_m}{\dfrac{W}{L} C_{ins} V_{DS}}$ is determined from the transconductance, $g_m = \left.\dfrac{\partial I_{DS}}{\partial V_{GS}}\right|_{V_{DS}}$, of the device at a small V_{DS} value, usually we use 1 V to ensure that the mobility was extracted from the linear region, where W and L are the channel width and length, respectively.

2. The effective mobility (μ_{eff}), $\mu_{eff} = \dfrac{g_d}{\dfrac{W}{L} C_{ins} (V_{GS} - V_T)}$ is determined from the drain (or output) conductance, $g_d = \left.\dfrac{\partial I_{DS}}{\partial V_{DS}}\right|_{V_{GS}}$, of the device also at a small V_{DS} (linear range) and use the highest applied V_{GS} value here.

3. The saturated mobility (μ_{sat}), $\mu_{sat} = \dfrac{g_m}{\dfrac{W}{L} C_{ins} (V_{GS} - V_T)}$, is determined from the transconductance, but uses the highest applied V_{DS} and V_{GS} value here to ensure the g_m value is obtained from the saturation range.

2.2.2 Previous works

Gan and Shih [57,58] reported the first CBD CdS thin-film transistors fabricated on Si/SiO_2 (n-type) substrate with a field-effect mobility of 1 cm^2/V s and on glass slide using anodic gate dielectrics with the field-effect mobility of 0.2 and 2 cm^2/V s for Al_2O_3 and Ta_2O_5 , respectively. CdS channel layer was deposited using the $CdCl_2$, $SC(NH_2)_2$, NH_4Cl, and NH_4OH chemistry at a constant temperature of 80 ^oC. Both postannealing processes were performed by vacuum annealing in N_2 ambient for 3-6 mins at 400 ^oC, in order to improve the CdS thin film crystallinity and were required for the formation of ohmic contacts. Voss *et al* [59] reported a depletion-mode CdS TFTs with an effective mobility of 2 cm^2/V s and postannealing process was employed in the vacuum ambient for 30 mins at 200 ^oC. More recently, Mereu *et al* [60] reported a CBD CdS TFTs with a thin nanocrystalline CdS layer (~70 nm) deposited at 60 ^oC for 1 hour and a drain current on-to-off ratio of nearly 10^2. Their device postannealing process was performed in the air for 1 hour at 300 ^oC. Chang *et al* [4] reported an enhancement-mode CdS TFTs with a field-effect mobility of ~1.5 cm^2/V s, a threshold voltage of $V_T \cong 14$ V and a drain current on-to-off ratio of approximately 10^6. The rapid thermal annealing (RTA) processes were employed in Ar ambient for 5 mins at 500 ^oC before and after evaporating the Al source and drain contacts in order to improve the CdS thin film crystallinity and form good ohmic contacts.

CHAPTER 3

CHEMICAL BATH DEPOSITION

3.1 Background

CdS thin films deposited by chemical bath deposition and series characterizations for better understanding of their structural, optical, chemical, and electrical properties were carried out. The studies of thin film morphology and growth and CdS particle formation were also included. Recent progress in fabricating an enhancement-mode CdS MISFET with a field-effect mobility of μ_{FE} $\cong$ 1.5 cm^2/V s and drain current on-to-off ratio of approximately 10^6 using CBD CdS channel layer is reported here. A novel reactor is needed to overcome those drawbacks associated with batch CBD process and to better understand and optimize the CBD thin film growth process.

3.2 Experimental Setup

The CBD reactor consists of a 1000 ml beaker, a plastic cover, a sample holder, a thermometer, a quartz crystal microbalance (QCM) probe (Maxtex PM 710), and a magnetic stir bar. The reactor is sitting on top of a VWR Dyla-Dual heater and magnetic stirrer. The stirring rate was set ~200 rpm and the temperature was maintained at 80 ^oC with a pH of ~11. The CBD bath condition has overall 0.004 M $CdCl_2$, 0.04 M $SC(NH_2)_2$, 0.04 M NH_4Cl and 0.4 M NH_4OH. The CdS thin film thickness and growth rate was monitored in-situ by a quartz crystal

microbalance probe. The signal from the quartz crystal probe is then sent to the quartz crystal monitor and computer for data acquisition. A schematic diagram of the experimental setup is shown in Figure 3.1.

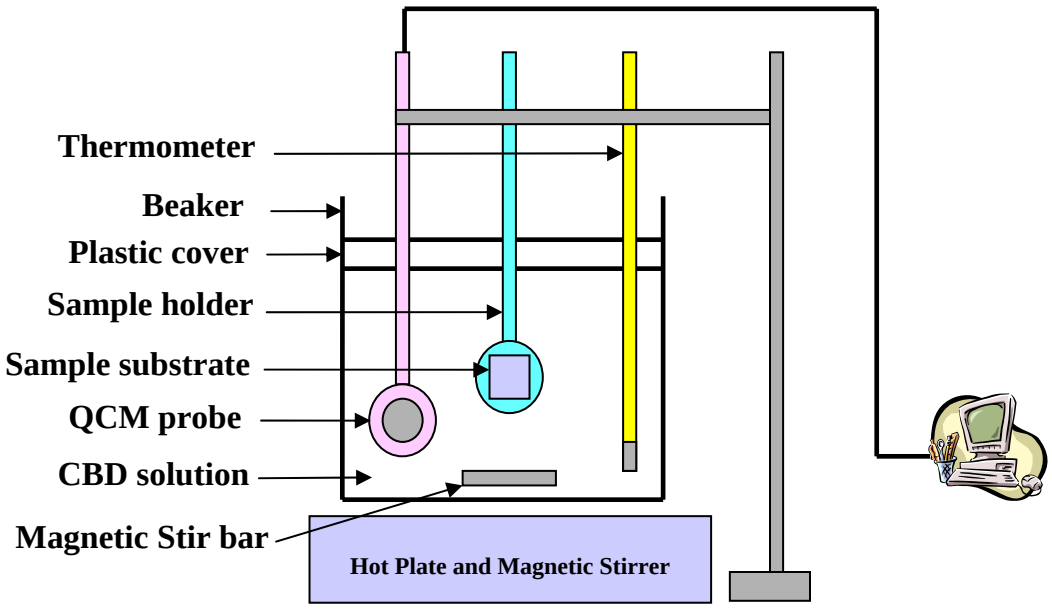

Figure 3.1 Schematic diagram of a typical CBD experimental setup.

3.3 Experimental Results

3.3.1 Thin Film Characterizations

The grown CBD CdS thin films were characterized by transmission electron microscopy (TEM), UV/VIS spectrophotometer, X-ray photoelectron spectroscopy (XPS), and four-point probe to determine its structural, optical, chemical, and electrical properties.

Selected area electron diffraction (SAED) was performed to determine the crystal structure of CBD CdS film. The obtained SAED pattern is shown in Figure 3.2. The observed d-spacing values are in good agreement with the JCPDS power diffraction data for hexagonal CdS phase. The SAED pattern also indicates the formation of a polycrystalline film.

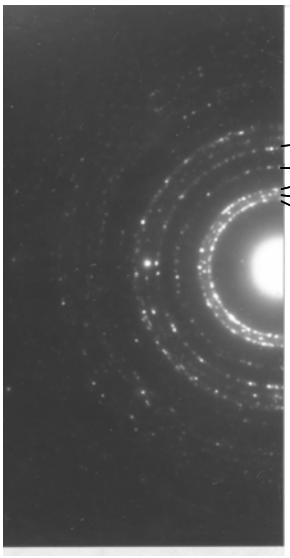

	JCPDS 6-314	JCPDS 10-454
Observed D-spacing values (A) for CdS	Hexagonal CdS	Cubic CdS
3.61	3.58 (100)	-
3.38	3.37 (002)	3.36 (111)
3.17	3.16 (101)	-
-	-	2.90 (200)
2.47	2.45 (102)	-
2.08	2.07 (110)	2.058 (220)

Figure 3.2 Selected-area electron diffraction pattern of CBD CdS thin film.

The absorption measurement of CdS thin film, measured at various wavelengths by a UV/VIS spectrophotometer was used to estimate the optical bandgap. A plot of $(\alpha E)^2$ versus E for a 500 Å thick CdS thin film was shown in Figure 3.3. Extrapolation of the linear portion of the curve to $(\alpha E)^2 = 0$ gives the

estimated optical bandgap, which is about 2.4 eV. This value is in good agreement with the reported bandgap value of 2.42 eV for CdS [61].

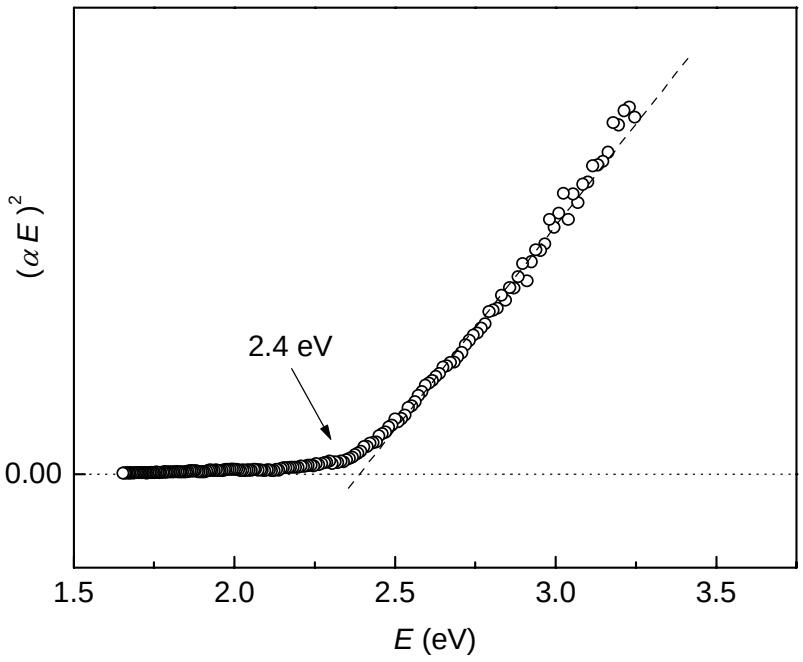

Figure 3.3 Estimated bandgap from optical absoption spectrum of chemical bath deposited CdS thin film on a glass slide.

The CdS layer was analyzed by XPS using a PHI Quantera Scanning ESCA. The spectrometer uses a monochromatic aluminum x-ray source of photon energy 1486.7 eV. Two areas on each section were surveyed as received, and then ion beam sputtered to an approximate depth of 100 Å (based on SiO_2 etch rates) and resurveyed. The analysis was performed using a 200 μm/40W photon beam

placed on the area of interest. The data were charge-corrected to carbon *1s* at 284.8 eV. The XPS binding energies of the Cd $3d_{5/2}$ at 405.3 eV and the S $2p_{3/2}$ at 161.6 eV for the as received samples are indicative of CdS chemistry. Low levels of Si are present and the XPS Si 2p binding energy at 103.2 suggests SiO_2. The presence of Si in the XPS data is likely due to regions of non-continuous CdS that expose the SiO_2 gate dielectric and is not necessarily incorporated into the CdS film. The high-resolution data are shown in Figure 3.4.

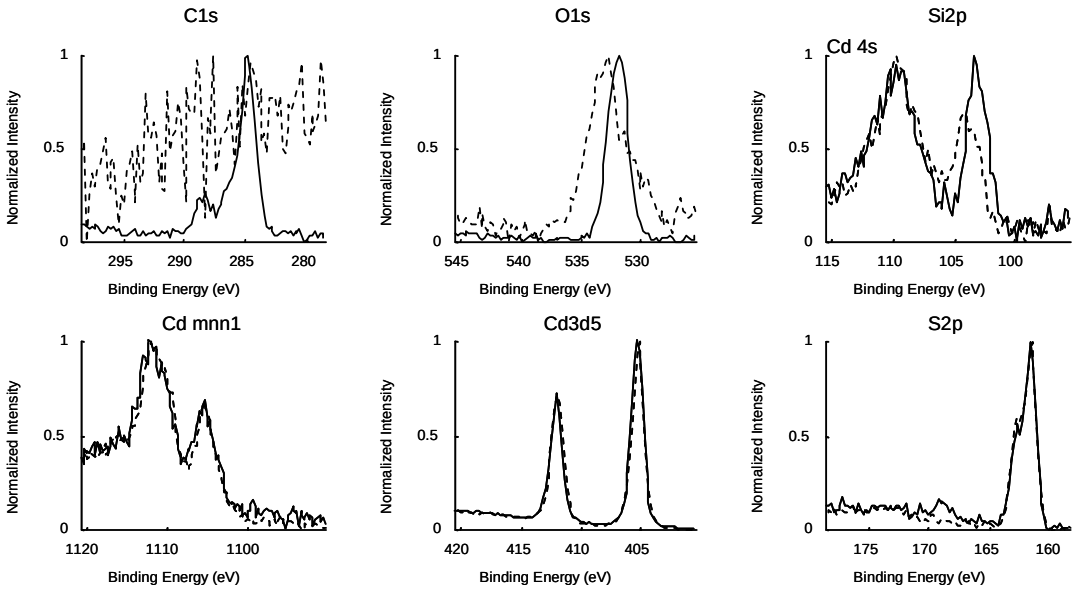

Figure 3.4 The XPS spectral data of a CBD CdS layer on top of a working CBD CdS MISFET (solid line - as received; dash line – after 100 Å sputtered clean).

To determine the resistivity of the as-deposited CBD CdS thin films, ten samples of 200 nm thick CdS were deposited on 25 mm x 25 mm glass substrates

for testing using a four-point probe at room temperature, which resulted in an average sheet resistance of 37.2 MΩ/SQ, that translated to an average resistivity of 744 Ω-cm.

3.3.2 Thin Film Morphology and Particle Growth

A scanning electron microscopy (SEM) image that indicates the analysis position for a typical CdS TFT after focused ion beam (FIB) sample preparation is shown in Figure 3.5, where (a) indicates the CdS channel layer and (b) indicates Al source and drain electrode contact layer. The top and cross-sectional SEM images of those layers are shown in Figure 3.5(a) and (b), respectively. The SEM images indicate the CBD CdS channel layer grown under current condition is dominated by a particle growth mechanism.

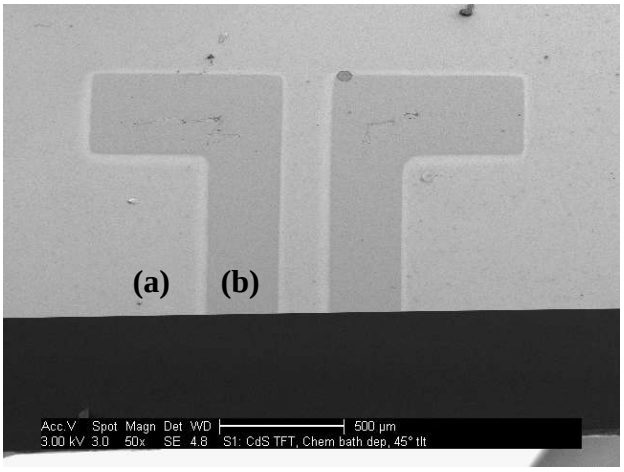
(a)
(b)
Acc.V Spot Magn Det WD 500 µm
3.00 kV 3.0 50x SE 4.8 S1: CdS TFT, Chem bath dep, 45° tlt

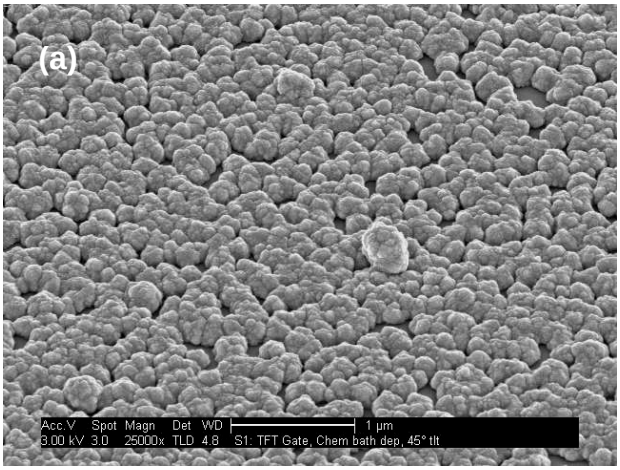
(a)
Acc.V Spot Magn Det WD 1 µm
3.00 kV 3.0 25000x TLD 4.8 S1: TFT Gate, Chem bath dep, 45° tlt

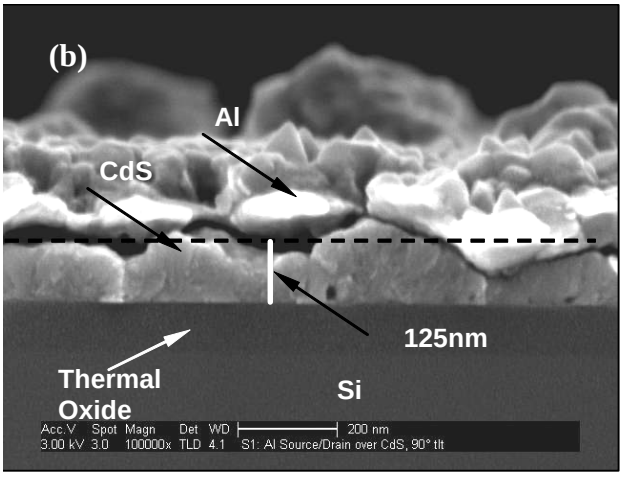
(b)
Al
CdS
125nm
Thermal Oxide
Si
Acc.V Spot Magn Det WD 200 nm
3.00 kV 3.0 100000x TLD 4.1 S1: Al Source/Drain over CdS, 90° tlt

Figure 3.5 Analysis position for SEM/FIB sample preparation: (a) CdS channel layer; (b) Al source and drain electrode contact layer. (a) Top-view SEM image of CdS channel layer and (b) cross-sectional SEM image of CdS channel layer with Al contact.

A typical real-time QCM growth curve for a CBD CdS process with a bath condition of 0.004M $CdCl_2$, 0.04M $SC(NH_2)_2$, 0.04M NH_4Cl, 0.4M NH_4OH, and pH=11 at 80 ^oC is shown in Figure 3.6. The QCM curve indicates that the CBD CdS film started at a linear growth regime (molecule-by-molecule) then changed to faster particle sticking growth after 100 seconds. The CBD CdS film shown in the SEM image (Figure 3.5) has been grown for 8.5 minutes (510 sec) (which is well within the particle sticking growth regime) before being out of the bath. Both SEM and QCM analysis suggest that the CBD CdS thin films grown under these conditions is dominated by a particle sticking mechanism.

To study the particle formation, solutions were taken from the CBD CdS reactor using a micropipette at different time after reaction occurred and then dropped onto Si/SiO_2 substrates. After 3 minutes, a micropipette was used to remove the solution. A tapping mode atomic force microscope (AFM) (Digital Instrument NanoScope) was used to characterize the homogeneous particle formation responsible for the colloidal sticking growth mechanism. AFM images of particles taken from the solution for initial 5 and 10 minute periods after the reaction started are given in Figure 3.6(a), (b) and (c), respectively. Figure 3.6(a) shows an AFM image of the sample prepared from the CBD solution right after

the reaction started. A number of large rod-shape thiourea crystals were clearly identified. Figure 3.6(b) shows an AFM image of the sample prepared from the CBD solution 5 minutes after the reaction started. A number of rod-shaped crystals could be identified clearly, in addition to smaller round-shaped particles. These rod-shaped crystals were formed most likely through a crystallization process of unreacted thiourea when the solvent evaporated. Figure 3.6(c) shows an AFM image of the sample prepared from the CBD solution 10 minutes after the reaction started. A large number of round-shaped (CdS) particles could be identified clearly and rod-shaped thiourea crystals could no longer be observed. This observation indicates that round-shaped CdS particles were growing at the expense of consuming sulfur from thiourea.

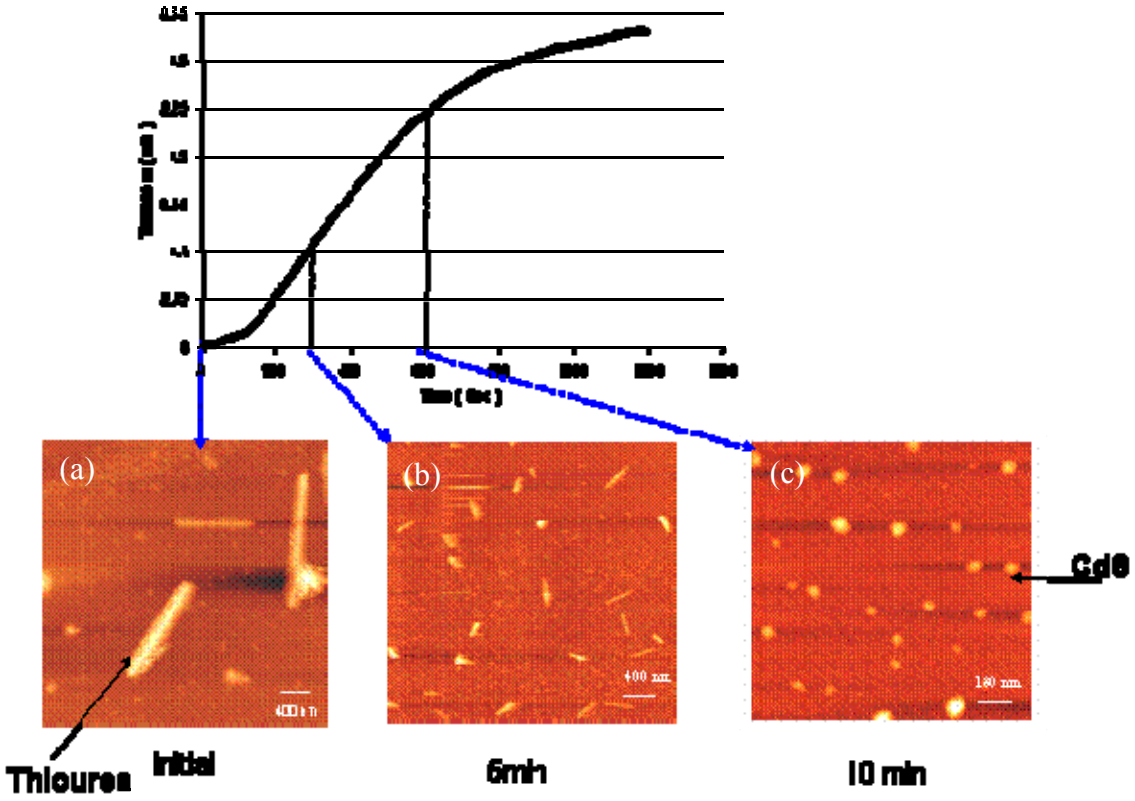

Figure 3.6 Typical QCM growth curve for a CBD CdS process and the corresponding AFM micrographs of the CdS particles taken from the CBD solution for (a) initial, (b) 5 minutes, and (c) 10 minutes after the reaction started.

A different CBD CdS growth was performed with a bath condition of 0.002M $CdCl_2$, 0.02M $SC(NH_2)_2$, 0.02M NH_4Cl, 0.2M NH_4OH at 80 ^oC for further elucidation of the molecule-by-molecule and particle-by-particle growth mechanism. A cross-sectional SEM image of the resulting CBD CdS thin film deposited on Si/SiO_2 substrate is shown in Figure 3.7(a). In this condition, the majority of CBD CdS thin film was formed within the compact layer growth

regime resulting in a denser film. The series of SEM images shown in Figure 3.7(b)-(d) suggest that film growth was terminated when particle sticking growth was initiated.

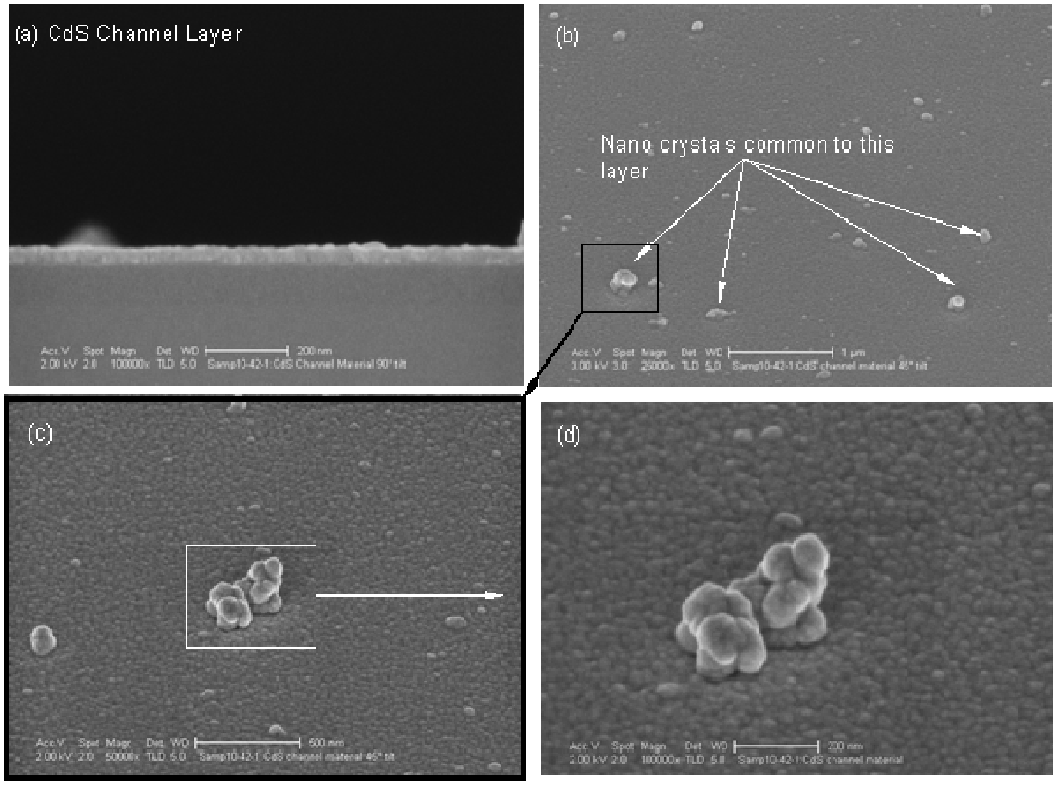

Figure 3.7 (a) Cross-sectional SEM image and a series of top-view SEM images ((b)-(d)) of CBD CdS thin film deposited on Si/SiO_2 substrate with a bath condition of 0.002M $CdCl_2$, 0.02M $SC(NH_2)_2$, 0.02M NH_4Cl, 0.2M NH_4OH at 80 ^oC.

3.3.3 Device Characterizations

For the device fabrication, a heavily boron-doped silicon substrate served as the gate in an inverted-gate structure. Silicon dioxide with a thickness of 100

nm was grown thermally on top of a silicon substrate and a 500 nm gold layer for gate contact was sputtered on the backside of a Si substrate. In order to reduce the gate leakage for the device fabrication, polyimide (Kapton) tape (McMaster-Carr) was used to tightly tape the four edges of the substrate to prevent shorting the device. A 200 nm CdS thin film was deposited on top of the SiO_2 by CBD with 0.004 M $CdCl_2$, 0.04 M $SC(NH_2)_2$, 0.04 M NH_4Cl and 0.4 M NH_4OH at 80 ^oC. A two-step rapid thermal annealing (RTA) process was performed in an argon atmosphere before and after evaporating 300 nm aluminum source and drain contacts for 5 minutes at 500 ^oC. The first anneal was to improve the CdS crystallinity of the semiconductor layer. The second anneal was to form a good source and drain ohmic contact between the aluminum and CdS layer. A schematic cross-sectional view of the CdS MISFET structure is shown in Figure 3.8. All the TFT testing was performed in the dark at room temperature with an HP 4156B semiconductor parameter analyzer.

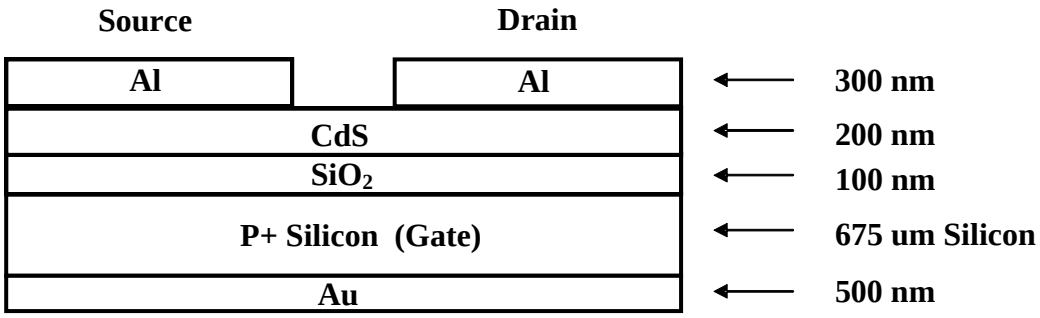

Figure 3.8 Schematic cross-sectional view of the CBD CdS MISFET structure.

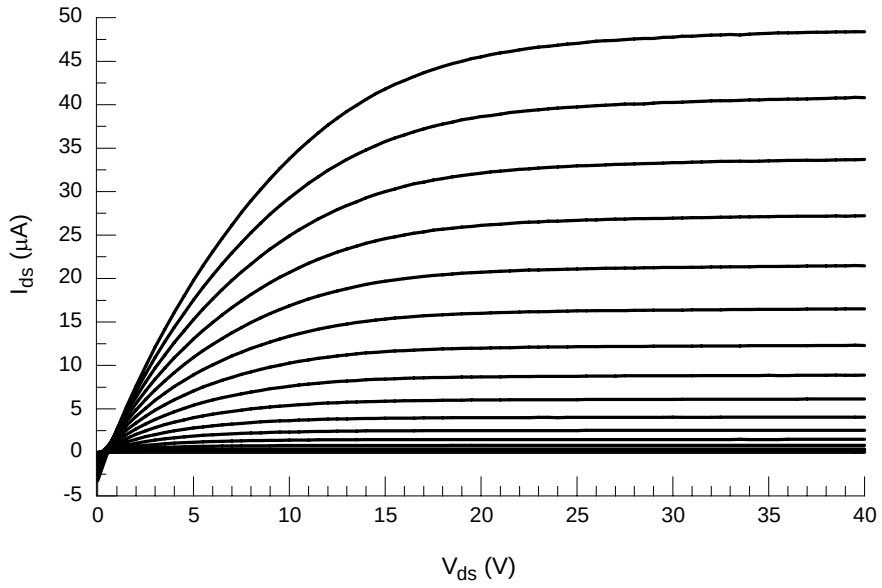

Figure 3.9 Drain current-drain voltage (I_{DS}-V_{DS}) characteristics for a CdS TFT with V_{GS} = 0 - 40 V in 2 V steps, V_{DS} = 0 - 40 V, and a channel width-to-length ratio of 7. The CdS channel layer is 200 nm thick and was deposited by CBD and rapid thermal annealed in Ar at 500 °C.

The drain current - drain voltage (I_{DS} - V_{DS}) characteristics are presented in Figure 3.9, which shows good transistor-like behavior and a hard saturation. It is evident from the negative current offset at zero drain voltage that there is a considerable amount of gate leakage for this device. Although this gate leakage does not degrade the pinch-off properties of this TFT, it will lead to an increase in power loss. To determine the source of the leakage, the dielectric was tested by depositing a series of Al top contacts with an area of 0.011 cm^2 to form a capacitor structure. The capacitors were tested for breakdown, with most yielding a breakdown of ~8 MV/cm and a current density of ~1 nA/cm^2. A few capacitors failed the breakdown test early indicating a defect in the dielectric. The defect was localized and did not compromise the rest of the dielectric on the substrate, but in the case of this transistor, where the semiconductor layer was a blanket coat across the substrate, the defect would affect the gate leakage even if it was not in the area of the channel. It appeared that this gate leakage was due to the presence of a defect in the SiO_2 layer at a distance remote from the transistor, which allowed the gate to make contact with the CdS layer and provided a path for the gate current. Because the semiconductor was a blanket layer, any defect in the SiO_2 would resistively couple with this gate leakage path. When a blanket coat of semiconductor material was placed across the majority of the substrate, linking all transistors together, any defect in the area would affect the gate leakage of all the transistors on that substrate. Those directly on top of the defect could not be used. Those that were close by experienced a greater amount of gate leakage than those

further away. The way to avoid this problem was to pattern the semiconductor or top gate material, isolating the working transistors from the defect.

The electrical parameters used to characterize this TFT are threshold voltage, mobility, and drain current on-to-off ratio. The threshold voltage is the minimum required gate voltage to produce a conductive channel, thereby enabling current to flow from source to drain. The threshold voltage for this device is approximated using a linear extrapolation method, with the drain current measured as a function of gate voltage at a low V_{DS} to ensure operation in the linear region. Figure 3.10 shows the drain current - gate voltage (I_{DS}-V_{GS}) at drain voltage, V_{DS} = 0.5 V using the linear extrapolation method for threshold estimation, resulting in a threshold voltage of $V_T \cong 14$ V. With a positive threshold voltage, this device behaves as an enhancement-mode device that is initially off and requires a positive gate voltage to allow current to flow.

The drain current on-to-off ratio determines the switching quality of the TFT. Figure 3.11 shows the log(I_{DS})-V_{GS} characteristics at drain voltage, V_{DS} = 40 V, showing an on-to-off ratio of approximately 10^6. This rather large drain current on-to-off ratio indicates that this device will function well as a switch.

The mobility of a TFT refers to the carrier mobility that is proportional to the carrier velocity in an electric field. The effective mobility (μ_{eff}) is the most common mobility reported and depends on lattice scattering, ionized impurity scattering, and surface scattering and is derived from the drain conductance. The

field-effect mobility (μ_{FE}) is determined by the transconductance of the device**.** The effective mobility for the device is $\mu_{eff} \cong 1$ cm^2/V s and the field-effect mobility is $\mu_{FE} \cong 1.5$ cm^2/V s.

Both depletion-mode and enhancement-mode devices were obtained. It was also noted that the depletion-mode devices exhibited a higher mobility (μ_{FE} ~6 cm^2/V s) than the enhancement-mode devices. Depletion-mode devices always exhibit a higher mobility than enhancement-mode devices because a larger fraction of the drain current arises from 'bulk' rather than the interface portion of the channel. Carriers that drift in the 'bulk' portion of the channel do not experience mobility degradation due to interface scattering and quantization.

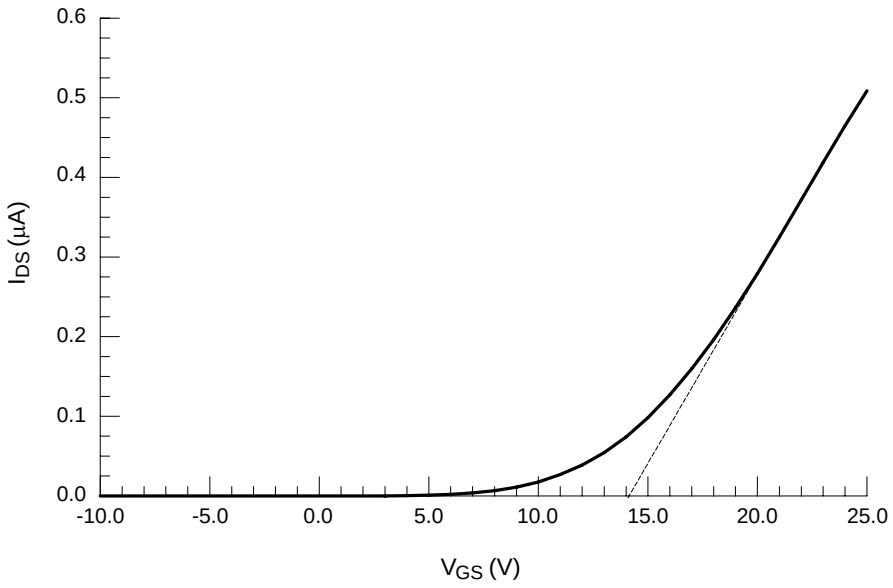

Figure 3.10 Drain current-gate voltage (I_{DS}-V_{GS}) at V_{DS} = 0.5 V for a CdS TFT showing a linear extrapolation method for threshold estimation, resulting in an estimated threshold voltage of $V_T \cong 14$ V.

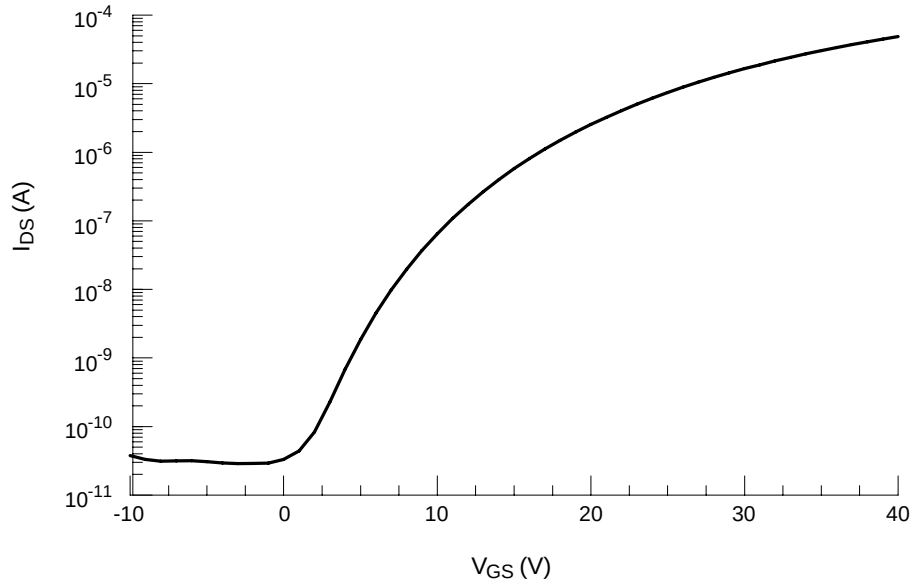

Figure 3.11 Log(I_{DS})-V_{GS} characteristics at V_{DS} = 40 V for a CdS TFT showing an on-to-off ratio of approximately 10^6.

In order to demonstrate the feasibility of fabricating flexible electronics, we tried to fabricate the bottom gate flexible CBD CdS MISFET on commercial available Poly(ethylene terephthalate) (PET)/ Indium Tin Oxide (ITO) polymeric substrate (Delta Technologies, Limited) using low temperature chemical bath deposited active channel materials.

The flexible device fabrication was started from evaporating a 100 nm thick SiO_2 insulator layer on top of the PET/ITO substrate following by a 200 nm CdS thin film deposited on top of the SiO_2 layer by CBD. Two-step post annealing

processes were performed before and after evaporating 300 nm aluminum source and drain contacts for 30 minutes at 200 ^{o}C in a vacuum furnace.

Figure 3.12(a) shows the schematic cross-sectional view of the flexible bottom gate CBD CdS MISFET structure using SiO_2 as gate insulation layer. A top view image of the flexible CdS MISFET structure and flexibility demonstration of this device are shown in Figure 3.12(b) and (c), respectively. The drain current-drain voltage (I_{DS}-V_{DS}) characteristics of the flexible device were shown in Figure 3.12(d). This CdS MISFET fabricated on a PET polymeric substrate exhibits the gate-modulated transistor behavior and a calculated channel field-effect mobility of ~8 cm^2/V s was obtained. This fabricated low-temperature flexible CdS MISFET was a depletion-mode device. It did not fully saturate due to a large channel conductance, thus precluding the channel from being fully turned-off. This preliminary experimental result, however, has demonstrated the feasibility of fabricating flexible MISFETs on PET/ITO substrate using chemical bath deposited channel materials.

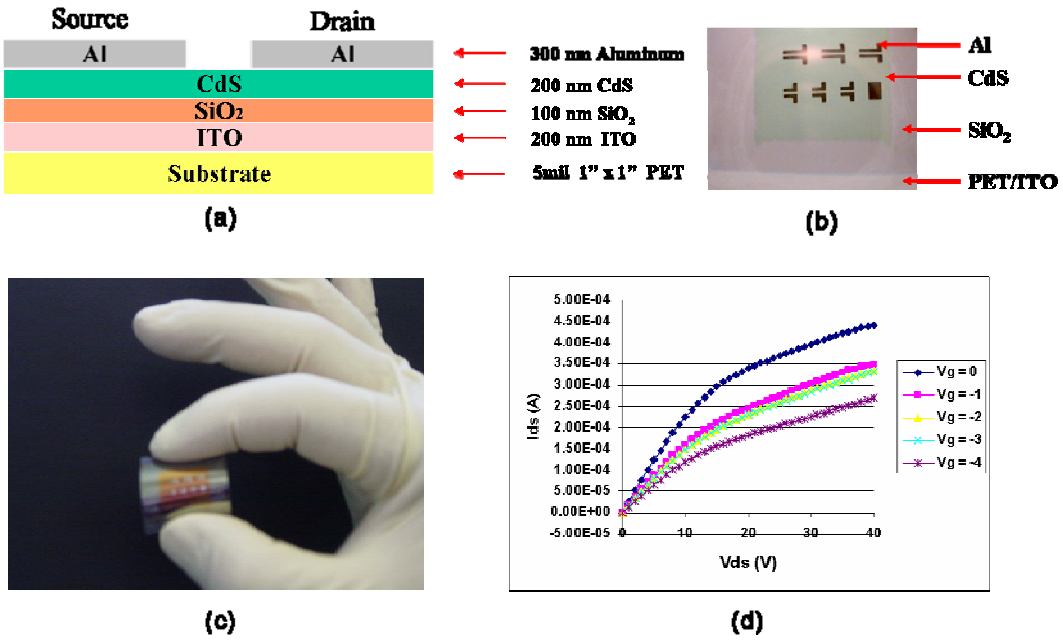

Figure 3.12 (a) Schematic cross-sectional view of the flexible bottom gate CBD CdS MISFET using SiO_2 as gate insulator layer, (b) a top view of the flexible CdS MISFET structure, (c) flexibility demonstration of this device, (d) drain current-drain voltage (I_{DS}-V_{DS}) characteristics for the flexible CdS MISFET with a channel width-to-length ratio of 12.

3.4 Issues with Chemical Bath Deposition

Although CBD has many advantages, it also suffers from three major drawbacks. First, in case of a batch CBD process, the heat supplied from the solution bath to the sample surface for chemical reaction results in not only heterogeneous CdS nucleation at the surface but also in homogeneous CdS particle formation in the bath. Particle formation will not only consume the chemical reactant concentration rapidly minimizing the heterogeneous thin film growth but also create a non-uniform morphology and pinholes making defects for the

devices. Second, the bath must be stirred continuously to ensure uniform thermal and chemical mixing and to minimize sticking of homogeneously nucleated CdS particles on the growing film surface. Third, the unequal volumes of the bath used to form the desired CdS film generates a lot of waste and the waste post treatment also increases the manufacturing cost. Although good progress has been made to reduce the bath volume-to-surface ratio [62], a comprehensible path for combining large area deposition with high growth rate and high conversion efficiencies has not been demonstrated yet. To solve those problems, it is necessary to design a novel reactor to decouple the homogeneous particle formation from heterogeneous surface reaction, to enhance the mixing quality in micro-scale instead of macro-scale, to utilize the bath solution efficiently and minimize the waste production, and to better understand and optimize the CBD thin film growth process.

CHAPTER 4

CONTINUOUS FLOW MICROREACTOR

4.1 Background

4.1.1 Continuous Flow Microreactor

In order to better understand the fundamental Chemical Bath Deposition (CBD) growth kinetics and mechanisms and optimize the CBD thin film growth process, we have developed a novel continuous flow microreactor that is capable of decoupling the homogeneous particle formation from heterogeneous thin film growth and able to overcome the drawbacks associated with the conventional batch process. This reactor with an integrated micromixer is able to achieve fast and uniform mixing on a micro-scale. It is capable of providing a temporal control over the homogeneous reaction by altering the impinging fluxes to tailor thin film micro- and nanostructures. This novel reactor also provides the benefit of introducing a constant flux of reactant solutions to the system (continuous process), that is capable of continuously depositing high quality thin films with the same growth rate which can not be achieved by conventional CBD process. Growth rate will be depleted at the saturated regime for batch CBD process; therefore, multiple deposition or higher reagent concentration are of necessity for depositing thicker films.

For our continuous flow microreactor, streams A and B are introduced into the mixing element and countercurrently enter the interdigital channels (30 μm),

where they are split into many interpenetrated substreams. The substreams exit the interdigital channel perpendicular to the direction of the feed flows, initially with a multilayered structure. Fast mixing through diffusion follows due to the small thickness of the individual layer. The homogeneous chemistry of the impinging fluxes can be controlled by the temperature of the bath and the residence time. A schematic diagram illustrates the capability of the continuous flow microreactor to separate the homogeneous and heterogeneous reaction for CBD as shown in Figure 4.1.

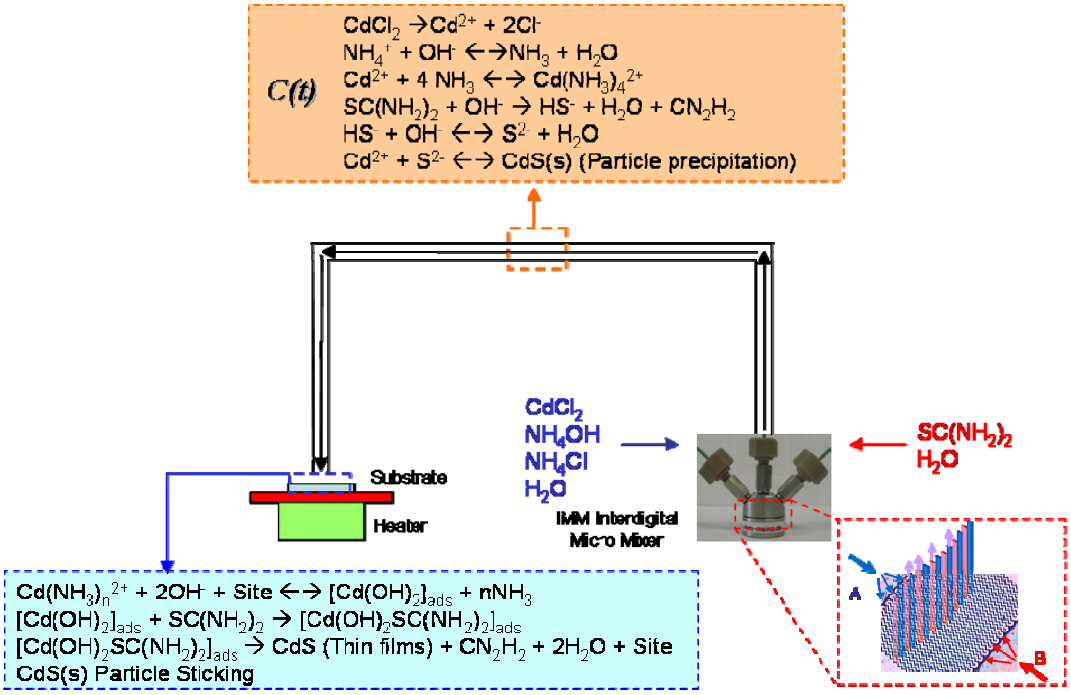

Figure 4.1 Schematic diagram illustrates the capability of the continuous flow microreactor to separate the homogeneous and heterogeneous reaction for CBD.

With this microreactor setup, we were able to obtain an impinging flux without the formation of nanoparticles at a short residence time (3 sec) [10,63] , as indicated from the transmission electron microscopy (TEM) analysis. Using this particle-free flux, the molecule-by-molecule heterogeneous growth can be promoted. Surface morphology analysis of the deposited thin films clearly showed that extremely smooth and highly oriented nanocrystalline CdS semiconductor thin films were successfully deposited on oxidized silicon substrates at low temperature (80 ^{o}C). Characterization results showed that the films deposited by the continuous flow microreactor were more uniform and of better quality than the conventional batch deposited ones [63]. Functional thin film transistors with an effective mobility of μ_{eff} =1.46 cm^2/V s were fabricated from the as-deposited films without any post annealing process [10].

In addition, the reactor could be operated in a homogeneous particle formation regime. Size increasing CdS nanoparticles and further aggregation and agglomeration grown by homogeneous reaction were clearly observed from TEM and corresponding SEM micrographs with mean residence time from 1 to 280 sec using pre-heated precursor solutions. The formation of CdS nanorod and arrayed nanorod bundle structures using the CBD recipe were observed in certain area and reported here for the first time.

This microreactor could be adopted for the deposition of other compound semiconductor thin films at low temperature using chemical solution deposition

and opens a low-cost avenue to fabricate thin film flexible electronics on polymeric substrates.

4.1.2 Nucleation Kinetics

The crystallization followed by the precipitation of powders or particles starts form the nucleation and continues growing in a supersaturated solution. Before the crystals can be developed, there must be embryos, seeds, or nuclei that first exist in the solution. Nucleation however can occur either spontaneously (homogeneous nucleation) or induced artificially (heterogeneous and secondary nucleation). Moreover, the rate of nucleation plays an important role in controlling the final particle size distribution. Generally, the nucleation process can be divided into three main categories: (1) Primary homogeneous nucleation that occurs spontaneously in the absence of a solid interface. (2) Primary heterogeneous nucleation that occurs in the presence of a solid interface of a foreign seed and can be induced by foreign particles. The primary nucleation refers to all cases of nucleation in the systems except the crystalline matter. (3) Secondary nucleation occurs in the presence of a solute-particle interface which is induced by crystals. The secondary nucleation refers to those nuclei that are often generated in the surrounding area of crystals presenting in the supersaturated solution. The mechanisms which administrate primary and secondary nucleation are not the same and result in different rate expressions [48,64].

For the homogeneous nucleation, the ideal steady-state condition is assumed and predicts immediate nucleation once superaturation is achieved. For a supersaturated solution, the overall excess free energy, ΔG, between a small particle of solute and the solute in the solution can be represented as the sum of two terms: the surface excess free energy, ΔG_s, and the volume excess free energy, ΔG_V. Where ΔG_s is a positive quantity and its magnitude is proportional to r^2. ΔG_V is a negative quantity proportional to r^3 in a supersaturated solution [64].

$$\Delta G = \Delta G_S + \Delta G_V$$

$$= 4\pi \cdot r^2 \gamma + \frac{4}{3}\pi \cdot r^3 \Delta G_v \qquad [4.1]$$

Where

r = Radius of spherical particle

γ = Interfacial tension or surface free energy per unit area

ΔG_v = Free energy change of the transformation per unit volume

Since the ΔG_s and ΔG_V are of opposite signs and depend differently on radius, the overall excess free energy, ΔG, will pass through a maximum value. This maximum value, ΔG_{crit}, corresponds to the critical nucleus, r_c, where it can be obtained by setting $d\Delta G / dr = 0$.

$$\frac{d\Delta G}{dt} = 8\pi \cdot r\gamma + 4\pi \cdot r^2 \Delta G_v = 0 \qquad [4.2]$$

Therefore,

$$r_c = \frac{-2\gamma}{\Delta G_v} \qquad [4.3]$$

By substituting $r=r_c$ into equation 4.1, we can get the maximum value of free energy, ΔG_{crit}.

$$\Delta G_{crit} = \frac{16\pi\gamma^3}{3(\Delta G_v)^2} = \frac{4\pi\gamma \cdot r_c^{\,2}}{3} \qquad [4.4]$$

The free energy diagram for homogeneous nucleation with the critical nucleus and the maximum value of free energy is shown in Figure 4.2 [64].

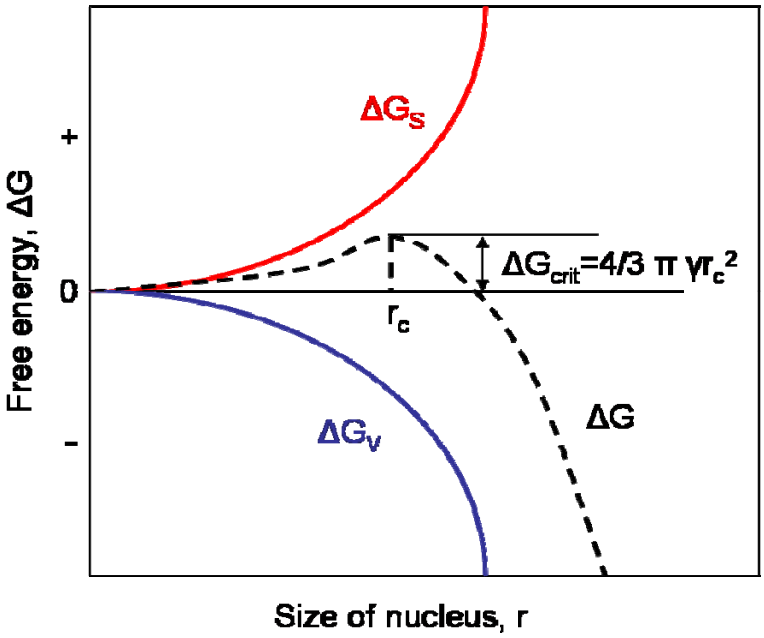

Figure 4.2 Free energy diagram for homogeneous nucleation.

The critical nucleus, r_c, represents the minimum size of a stable nucleus. When an embryo with an size $r < r_c$, it will dissolve and remain as an embryo, until $r \geq r_c$ where a nucleus will start to form and their Gibbs free energy will start to decrease owing to the growth. This process will form the stable nuclei following by particle formation.

The rate of nucleation, J , the number of nuclei formed per unit time per unit volume, can be expressed in the form of the Arrhenius reaction velocity equation used for the rate of a thermally activated process:

$$J = A\exp(-\Delta G / kT) \qquad [4.5]$$

where

A = Pre-exponential factor

k = Boltzmann constant

The basic Gibbs-Thomson relationship for a non-electrolyte can be expressed as [64]:

$$\ln S = \frac{2\gamma\nu}{kTr} \qquad [4.6]$$

where

S = Saturation ratio, and $S = \frac{C}{C_{eq}}$

C = Solution concentration

C_{eq} = Equilibrium solubility of the solute

ν = Molecular volume

From equation 4.3 and 4.6, we can obtain the following equation:

$$-\Delta G_v = \frac{2\gamma}{r} = \frac{kT \ln S}{\nu} \qquad [4.7]$$

Therefore, ΔG_{crit} (from equation 4.4) can be further expressed as:

$$\Delta G_{crit} = \frac{16\pi\gamma^3 v^2}{3(kT\ln S)^2} \qquad [4.8]$$

and

$$r_c = \frac{2\gamma v}{kT\ln S} \qquad [4.9]$$

By substituting equation 4.8 into 4.5, we can obtain the rate of homogeneous nucleation:

$$J_{Hom} = A\exp\left[-\frac{16\pi\gamma^3 v^2}{3k^3T^3(\ln S)^2}\right] \qquad [4.10]$$

This rate equation indicates three major variables that govern the rate of nucleation: interfacial tension, γ, temperature, T, and saturation ratio, S.

For the heterogeneous nucleation, it is induced by a foreign surface having a lower surface energy compared to the new solution particle and takes place at a lower critical supersaturation. The overall free energy change associated with the formation of a critical nucleus under heterogeneous conditions, $\Delta G'_{crit}$, must be

less than the corresponding free energy change, ΔG_{crit}, associated with homogeneous nucleation. Their relationship can be expressed as:

$$\Delta G_{crit}^{'} = \phi \cdot \Delta G_{crit} \qquad [4.11]$$

where the factor ϕ is less than unity.

Figure 4.3 shows the interfacial energy diagram for three different phases in contact. Here the three interfacial tensions are denoted by: γ_{cs}, the boundaries between the crystalline phase and the foreign solid surface; γ_{cl}, the boundaries between the crystalline phase and the liquid; γ_{sl}, the boundaries between another foreign solid surface and the liquid [64].

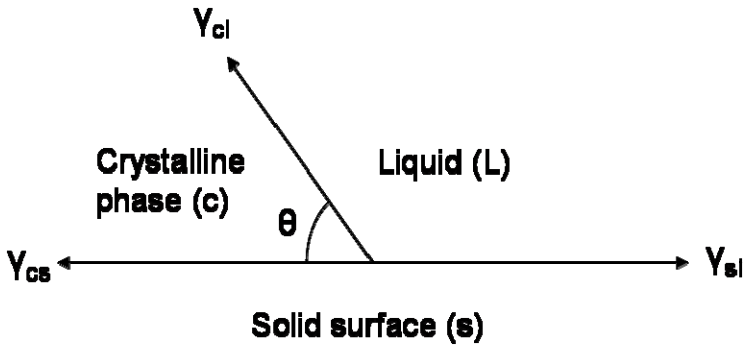

Figure 4.3 Interfacial energy diagram for three different phases in contact.

The interfacial tension is an important factor controlling the nucleation process. The relationship for these three interfacial tensions can be expressed as equation 4.12 or 4.13. The angle θ corresponds to the angle of wetting in liquid and solid systems.

$$\gamma_{sl} = \gamma_{cs} + \gamma_{cl} \cos\theta \qquad [4.12]$$

$$\cos\theta = \frac{\gamma_{sl} - \gamma_{cs}}{\gamma_{cl}} \qquad [4.13]$$

The factor ϕ in equation 4.11, can be expressed as:

$$\phi = \frac{(2 + \cos\theta)(1 - \cos\theta)^2}{4} \qquad [4.14]$$

When θ=0 (complete wetting), ϕ=0, $\Delta G'_{crit}$=0, the free energy of nucleation is zero and no nuclei have to be formed in the solution. When $0<\theta<180^o$ (partial wetting of a solid with a liquid), $\phi < 1$, $\Delta G'_{crit} < \Delta G_{crit}$, the nucleation is easier to achieve because the required overall excess free energy is less than that for the homogeneous nucleation. When θ=180^o (complete non-

wetting), $\cos\theta$=-1 and ϕ=1, $\Delta G^{'}_{crit} = \Delta G_{crit}$, the overall free energy of nucleation is the same as the homogeneous or spontaneous nucleation.

4.2 Heterogeneous Reaction

4.2.1 Experimental Setup

Oxidized silicon substrates (silicon wafer coupons) measuring 15 x 10 mm were used for deposition studies. The coupons were initially sonicated in an ultrasonic bath using 1M NaOH for about 10-15 minutes and then cleaned according to standard acetone, methanol, DI water (AMD) procedure. Finally, they were dried under a stream of nitrogen gas before being used for deposition.

The continuous flow microreactor used in our experiments basically consists of two 25 ml syringe pumps, a micromixer, and a heated substrate holder. They are connected using polycaryl-ether etherketone (PEEK) tubes (1/16 in. OD, 0.03 in. ID from Upchurch Scientific) as shown in Figure 4.4.

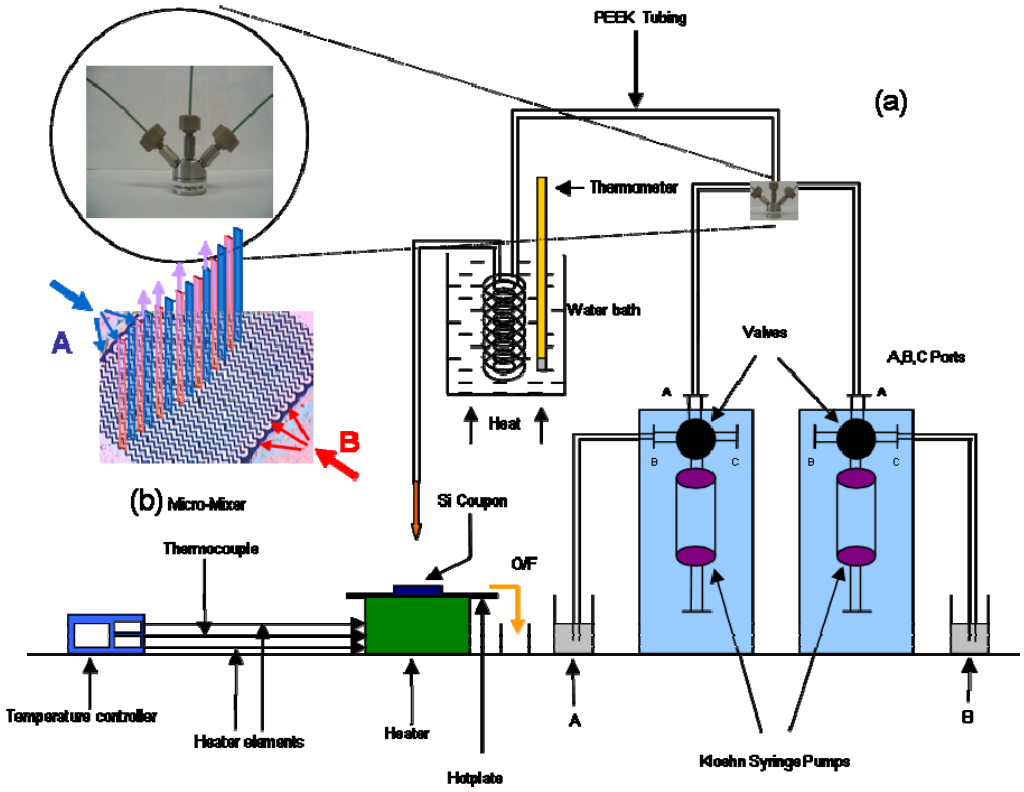

Figure 4.4 Schematic diagrams of (a) a continuous flow microreactor experimental setup and (b) an interdigital micromixer.

Two syringe pumps (V6 module from Kloehn Ltd.) were used for holding reactant streams A and B before mixing. Each pump has three ports (A, B, C). One port of each pump was used for aspirating the reactant streams and the other port was used for dispensing them. The standard slit interdigital micro mixer (SSIMM from Institut für Mikrotechnik Mainz, Germany) [65] was used for our experimental studies. Micromixers offer features which cannot be easily achieved by macroscopic devices, such as ultrafast mixing at the microscale [66]. It is essentially made of a stainless steel SS 316Ti housing with an inlay of thermally

oxidized silicon (30 x 100 µm channels). These mixer inlays are fabricated by an advanced silicon etching (ASE) technique. Figure 4.5 shows the optical images of (a) a disassembled interdigital micromixer and its top and bottom housing with inlay and (b) high resolution SEM micrograph of microchannels [67].

(a)

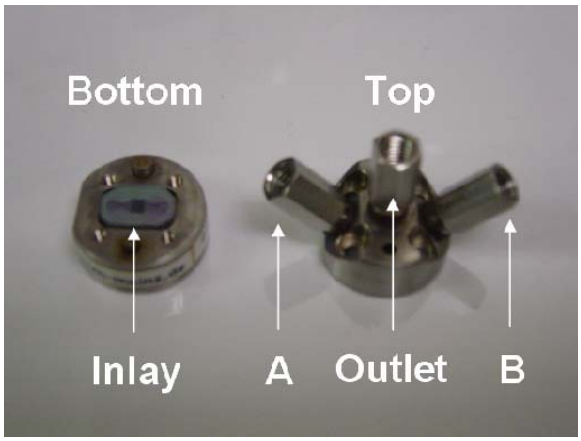

(b)

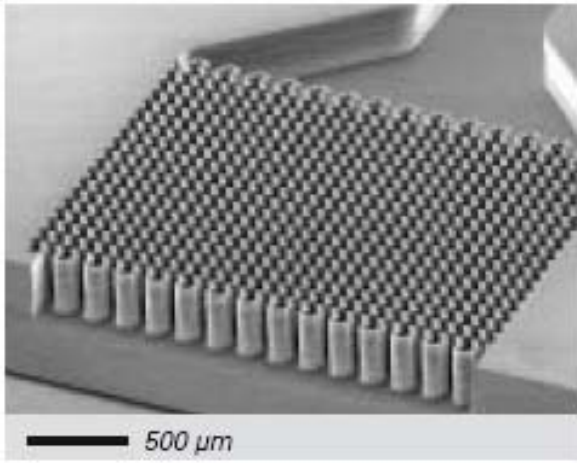

Figure 4.5 Optical images of (a) a disassembled interdigital micromixer and its top and bottom housing with inlay and (b) high resolution SEM micrograph of microchannels.

In all experiments, the reactant streams A and B were initially loaded into the syringe pumps and then dispensed through the PEEK tube and allowed to mix in the micromixer. Stream A consisted of 12 ml of 0.0163 M $CdCl_2$, 10 ml of 0.196 M NH_4Cl, and 2 ml of 9.8 M NH_4OH, where stream B consisted of 12 ml of 0.163 M $SC(NH_2)_2$ and 13 ml of deionized water. The final concentration of the reactants were 0.004 M $CdCl_2$, 0.04 M NH_4Cl, 0.04 M $SC(NH_2)_2$ and 0.4 M NH_4OH. The resulting mixture was passed through a 5 ft long coil (PEEK), which was immersed in a hot water bath maintained at 80-85 ^oC. The solution was impinged on the substrate, which was taped to a 3 in. diameter SS metallic plate and heated on a hotplate (2 in. diameter x 0.75 in. thick SS disk from Watlow) at 80-90 ^oC. The syringe pumps were operated at a speed of 250 steps/sec (Hz), ~0.13 ml/sec, and the mean residence time of the mixture after passing the micromixer was about 3 secs. Once the process was completed, the substrate was removed from the plate, washed with Millipore DI water, and dried under a stream of nitrogen gas.

4.2.2 Experimental Results

A thin film of 250 nm thickness of CdS was deposited on the silicon coupon with the continuous flow microreactor in the temperature range of 80-90 ^oC after 3.12 minutes. The phase and crystalline orientation of this thin film was determined by X-ray diffraction (XRD, Siemens D-5000) with Cu Kα radiation

(Figure 4.6(a)), which shows diffraction peaks at $2\theta = 26.5^{o}$ and $2\theta = 55^{o}$. These diffractogram peaks were compared with the standards in the JCPDS data files [68]. The as-deposited material appears to be composed of the cubic phase of CdS. In particular, both peaks correspond to the (111) and (222) Bragg reflection planes from the cubic (zincblende) phase. For testing the accuracy of our result and for comparison, XRD was also done on a bare silicon coupon and the peaks obtained are shown in the same graph. The presence of only these reflections indicates the highly oriented nature of our CdS films deposited by the continuous flow microreactor, which must grow as successive alternative planes composed of only either Cd or S atoms parallel to the substrate surface, as they corresponds to the (111) planes of the cubic crystalline structure. This type of growth is in good agreement with the molecular-level growth mechanism proposed by Ortega-Borges and Lincot [27], which is based on the adsorption of the cadmium hydroxide species and the successive formation of the metastable complex by the adsorption of a thiourea molecule. In contrast, the XRD spectrum from the as-deposited CdS thin films by a batch process shows a relatively broad peak which indicates its poor crystallinity as shown in Figure 4.6(b).

CdS can exist in three different crystal forms: hexagonal (wurtzite), cubic (zincblende or sphalerite) and cubic (rocksalt). The rocksalt form of CdS has been observed only at very high pressures; however, CBD films of this form have never been reported. Two other forms have been reported for CBD films under different conditions. The hexagonal form is thermodynamically more stable and occurs

more easily from the high temperature growth technique. Therefore, the low temperature CBD method allows the formation of the cubic (zincblende) phase.

(a)

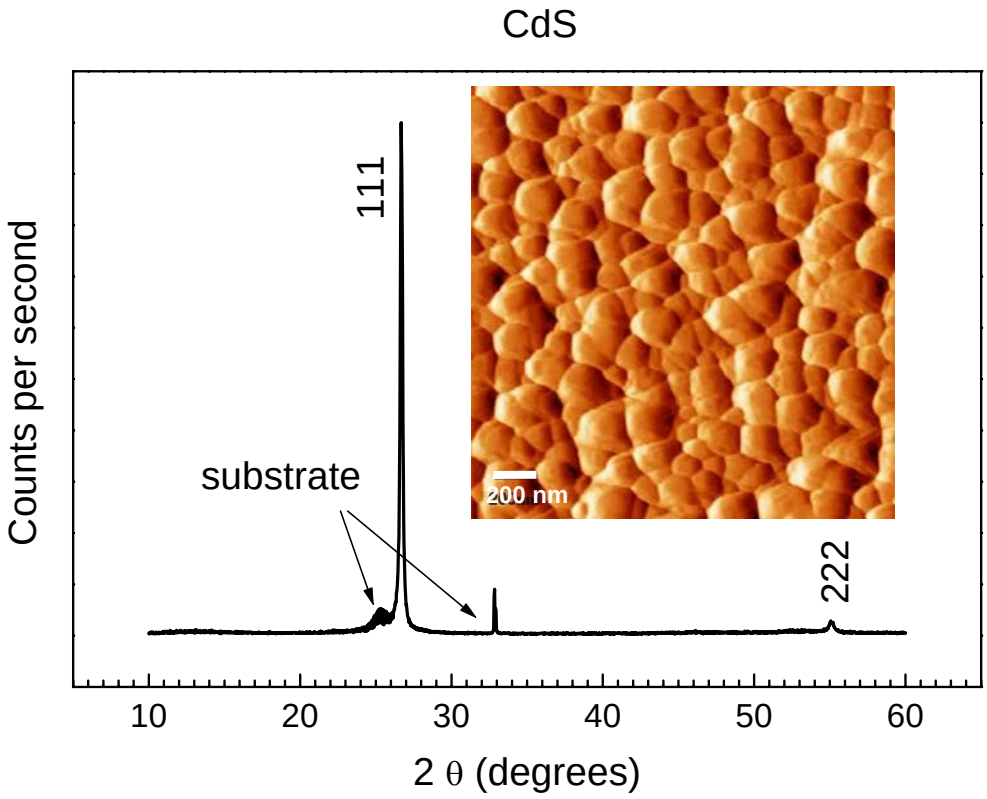

(b)

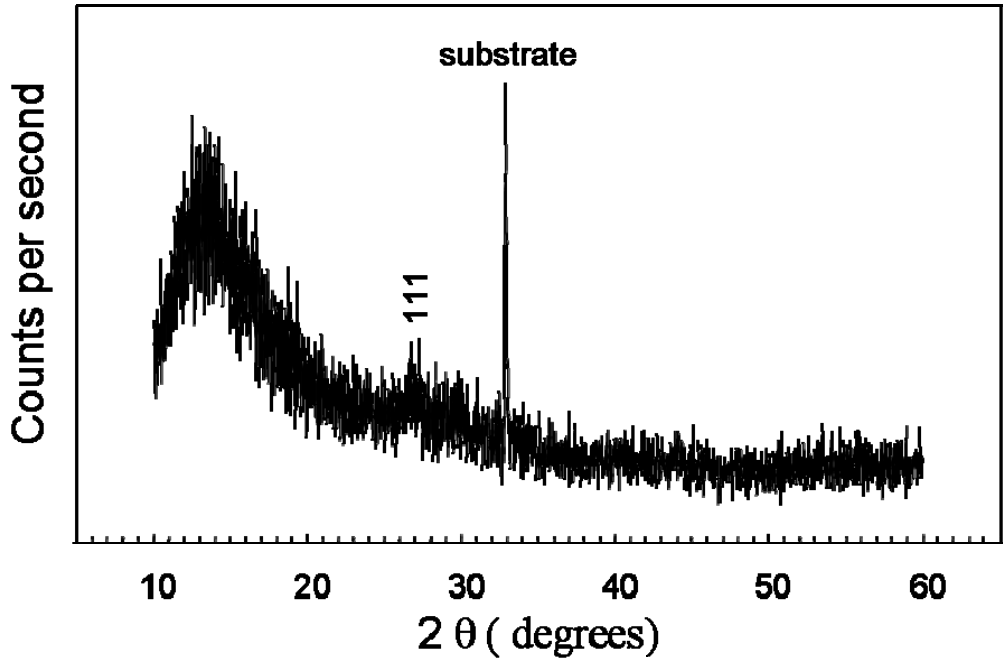

Figure 4.6 X-ray diffractogram of CdS films deposited by (a) a continuous flow microreactor with 1 x 1 μm scan size of AFM image (inset) and (b) a batch reactor.

The continuous flow microreactor supplied a reactant flux with constant concentration that provided a higher heterogeneous nucleation density than a batch reactor could provide. This high nucleation density played a significant role in improving film coverage. Figure 4.6(a) (inset) shows the surface morphology of the CdS film deposited on silicon-oxidized substrate with the scan size of 1 x 1 μm using the continuous flow microreactor. The CdS thin film morphology was characterized by atomic force microscopy (AFM, DI Nanoscope III) in the contact mode. The AFM image shows that a continuous nanocrystalline film was formed.

The root mean square (RMS) value of roughness was found to be 11.751 nm with a mean roughness of 9.606 nm.

The absorption measurement of the as-deposited CdS thin film, measured at various wavelengths by a UV-Vis spectrophotometer, was used to estimate the optical bandgap. Two plots of $(\alpha E)^2$ versus E for thin film deposited on a glass slide by a batch reactor and a continuous flow microreactor are shown in Figure 4.7(a) and (b), respectively. Extrapolation of the linear portion of the curve to $(\alpha E)^2=0$ gives the estimated optical bandgap of 2.41 eV from a batch reactor and 2.43 eV from a continuous flow microreactor. Both values are in good agreement with the reported bandgap value of 2.42 eV for CdS [61].

(a)

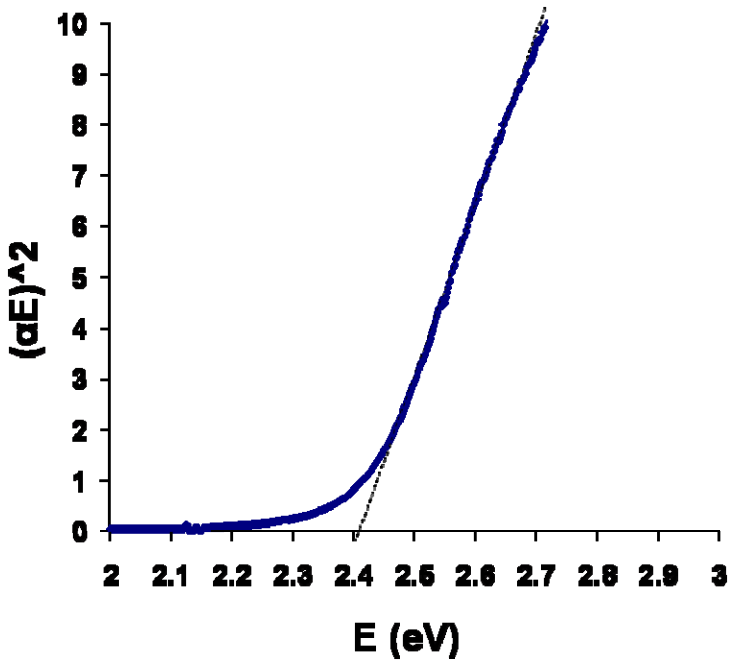

(b)

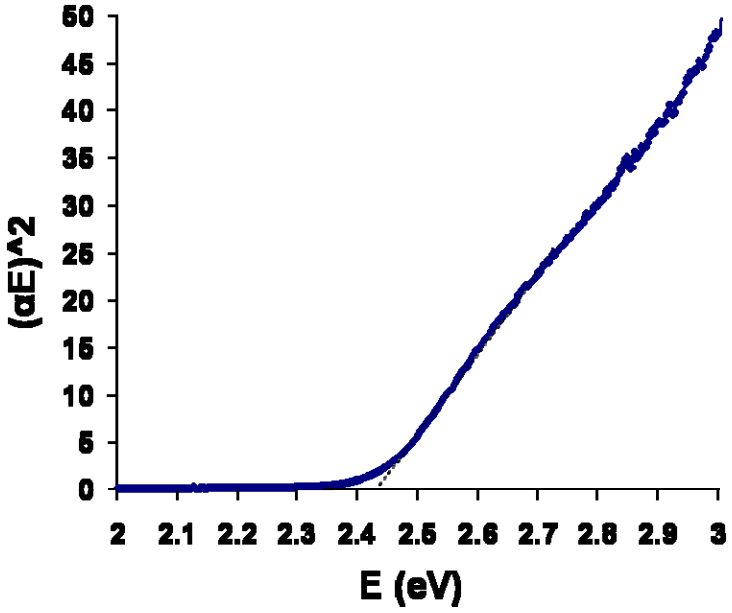

Figure 4.7 The estimated optical bandgaps of as-deposited CdS films deposited by (a) a batch reactor and (b) a continuous flow microreactor.

We were able to obtain an impinging flux without the formation of nanoparticles, at a short residence time (3 sec) [10], as indicated from the transmission electron microscopy analysis [63]. TEM samples were obtained by dipping copper grids (with thin lacey carbon film) in hot solution and were collected from the continuous flow microreactor, for about 10 sec. There was no evidence of any particles on the surface of the grid. This sample had no crystallinity and nothing of interest was found. Also, the energy dispersice X-ray (EDX) analysis did not show any CdS. This result indicated that the impinging reactant flux from the continuous flow microreactor was particle-free under this operating condition. Thus, the CdS films were grown through a molecule-by-

molelcule mechanism. Using this particle-free flux, the molecule-by-molecule heterogeneous growth can be promoted.

For CdS metal-insulator-semiconductor field-effect transistors (MISFETs) fabrication, a heavily boron (p+) doped silicon substrate served as the gate in an inverted-gate structure. Silicon dioxide with thickness of 100 nm was thermally grown on top of a silicon substrate and a 500 nm gold layer for gate contact was sputtered on the backside of the Si substrate. A schematic cross-sectional view of the CdS MISFET structure is shown in Figure 4.8. The semiconductor channel material was patterned in order to reduce the gate leakage current [4]. For this purpose, around 1 μm thick positive photoresist was first spun on the Si substrate followed by a photolithography process. A ~50 nm CdS thin film was deposited on top of the SiO_2 by the continuous flow microreactor. After the deposition, the sample was immersed into an acetone solution and gently agitated to remove the photoresist and lift-off the additional CdS layer. After the sample was removed from the solution, it was washed with DI water and dried under a stream of nitrogen gas. No further post annealing process was performed. The 300 nm aluminum source and drain contacts were then evaporated on top of CdS layer through a shadow mask with a channel width-to-length ratio of 12 (channel length is 200 μm) in order to complete the process of fabricating CdS MISFETs.

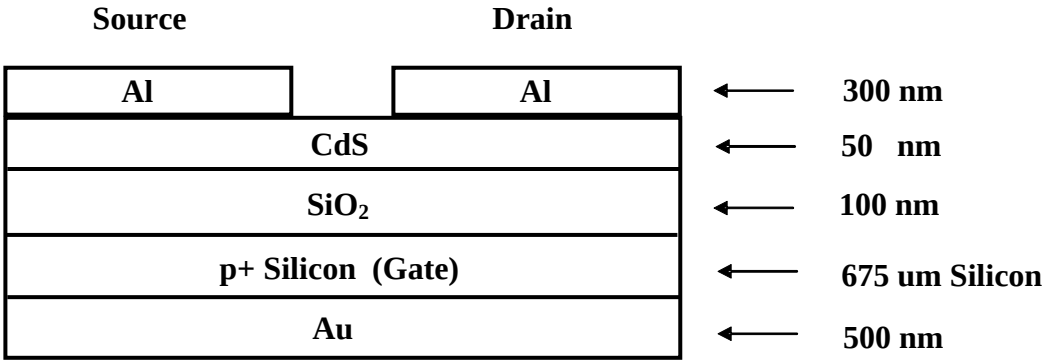

Figure 4.8 Schematic cross-sectional view of the CdS MISFET structure.

The drain current-drain voltage (I_{DS}-V_{DS}) output characteristics presented in Figure 4.9(a) shows that the CdS MISFET behaves as an n-channel transistor with good gate modulation and hard saturation. We have characterized the MISFET parameters including threshold voltage, mobility, drain current on-to-off ratio, and turn-on voltage. The threshold voltage is the minimum required gate voltage to produce a conductive channel, thereby enabling electrons to flow from the source to the drain. The threshold voltage for this device is approximated by a linear extrapolation method with the drain current measured as a function of gate voltage at a low V_{DS} to ensure operation in the linear region. Figure 4.9(b) shows the drain current - gate voltage (I_{DS}-V_{GS}) at V_{DS} = 1 V using the linear extrapolation method for threshold estimation, resulting in a threshold voltage of $V_T \cong 25$ V. With a positive threshold voltage, this device behaves as an

enhancement-mode device that is initially off and requires a positive gate voltage to allow current to flow.

The mobility of a MISFET refers to the carrier mobility that is proportional to the carrier velocity in an electric field. The effective mobility (μ_{eff}) (the most common reported mobility) is derived from drain conductance. The field-effect mobility (μ_{FE}) was determined from the transconductance of the device at V_{DS} = 1 V to ensure mobility extracted from the linear region**.** The effective mobility for the CdS device presented here is $\mu_{eff} \cong 1.46$ cm^2/V s, and the field-effect mobility is $\mu_{FE} \cong 1.4$ cm^2/V s.

The drain current on-to-off ratio determines the switching quality of the MISFET. Figure 4.9(c) shows the log(I_{DS})-V_{GS} transfer characteristics at V_{DS} = 40 V showing a drain current on-to-off ratio of approximately 10^5 and turn-on voltage at 0 V.

(a)

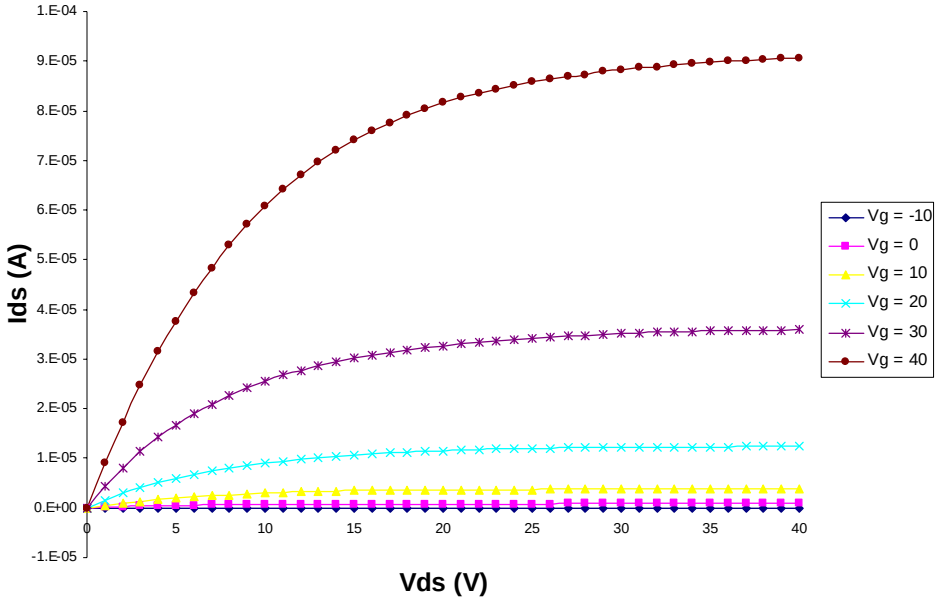
1.E-04
9.E-05
8.E-05
7.E-05
6.E-05
5.E-05
4.E-05
3.E-05
2.E-05
1.E-05
0.E+00
-1.E-05
0
5
10
15
20
25
30
35
40
Ids (A)
Vds (V)
Vg = -10
Vg = 0
Vg = 10
Vg = 20
Vg = 30
Vg = 40

(b)

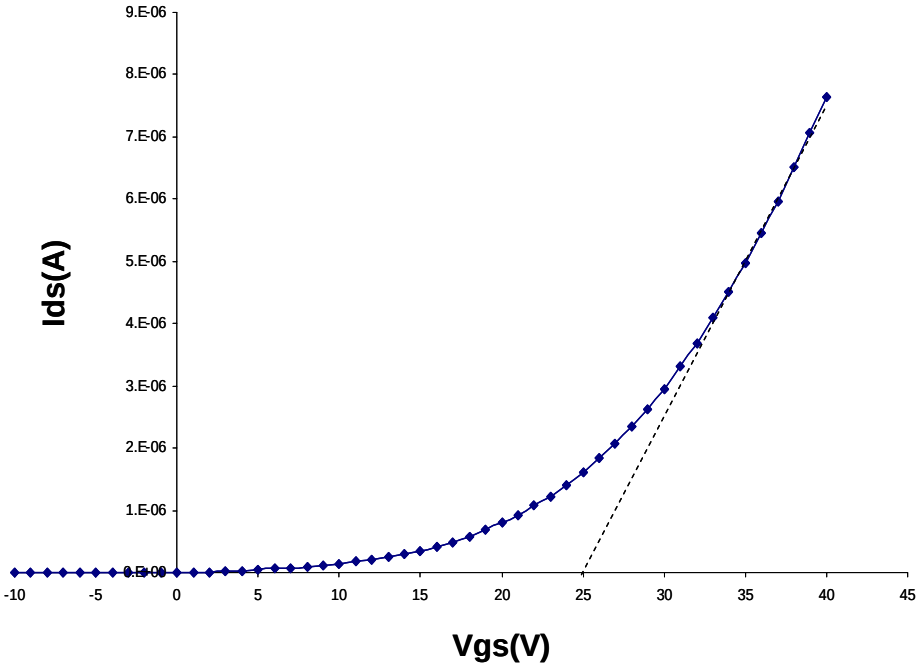
9.E-06
8.E-06
7.E-06
6.E-06
5.E-06
4.E-06
3.E-06
2.E-06
1.E-06
-10
-5
0
5
10
15
20
25
30
35
40
45
Ids(A)
Vgs(V)

(c)

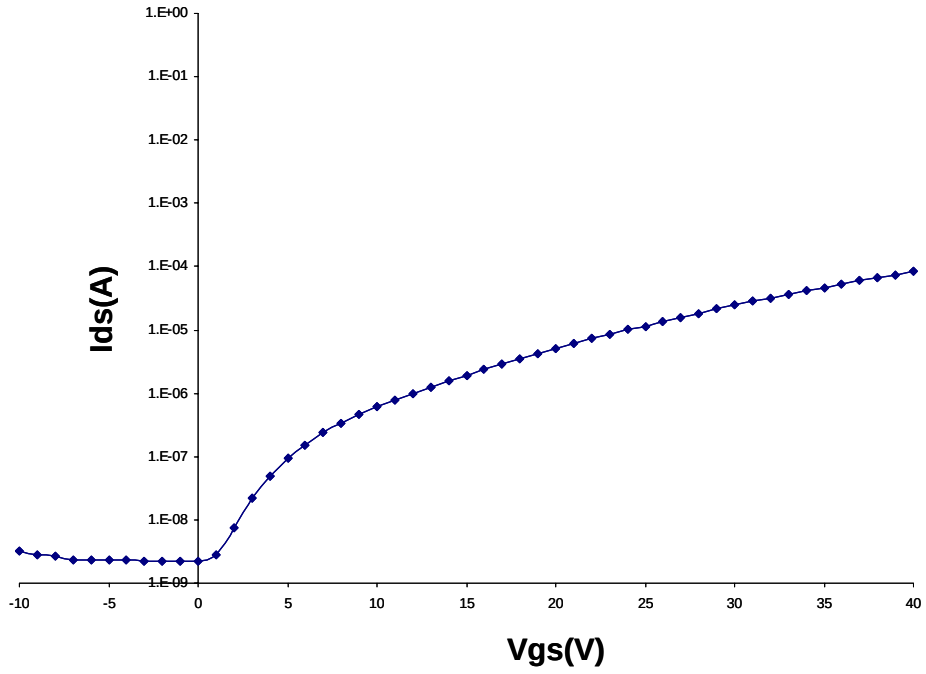

Figure 4.9 (a) Drain current-drain voltage (I_{DS}-V_{DS}) output characteristics for a channel width-to-length ratio of 12. (b) Threshold voltage estimation at V_{DS} = 1 V. (c) Drain current on-to-off ratio determination at V_{DS} = 40 V.

This enhancement-mode CdS MISFET with a CdS channel layer deposited by the continuous flow microreactor at low temperature (80-90 ^{o}C) shows an effective mobility and a field-effect mobility comparable to or higher than previously reported data, for example, $\mu_{FE} \cong 1$ cm^2/V s from Gan and Shih [57], $\mu_{FE} \cong 1.5$ cm^2/V s from Chang *et al* [4], $\mu_{eff} \cong 2$ cm^2/V s from Voss *et al* [59]. In comparison, $\mu_{FE} \cong 0.2$ and 2 cm^2/V s using Al_2O_3 and Ta_2O_5 gate dielectrics, respectively, as reported by Gan and Shih [58]. All previously reported CBD CdS

MISFETs employed a postannealing process such as vacuum annealing in N_2 ambient for 3-6 mins at 400 ^oC [57, 58], vacuum annealing for 30 mins at 200 ^oC [59], air annealing for 1 hour at 300 ^oC [60], and rapid thermal annealing in Ar ambient for 5 mins at 500 ^oC [4]. Our results show it is possible to fabricate TFTs on low-cost flexible polymeric substrates using a chemical solution deposition technique.

4.3 Homogeneous Reaction

4.3.1 Experimental Setup

Due to previously used syringe pump is limited to hold only 25 ml volume of solution, the microprocessor controlled peristaltic pump instead of two syringe pumps was used here. The continuous flow microreactor for homogeneous reaction consists of a microprocessor controlled peristaltic pump (Ismatec REGLO Digital), three 1.22 mm ID Tygon ST tubes (Upchurch Scientific), an interdigital micromixer (SSIMM from Institut für Mikrotechnik Mainz, Germany), hotplate (VWR), a porcelain filter funnel (VWR), and a flask.

The schematic diagram of the experimental setup for studying the homogeneous reaction by a continuous flow microreactor is shown in Figure 4.10.

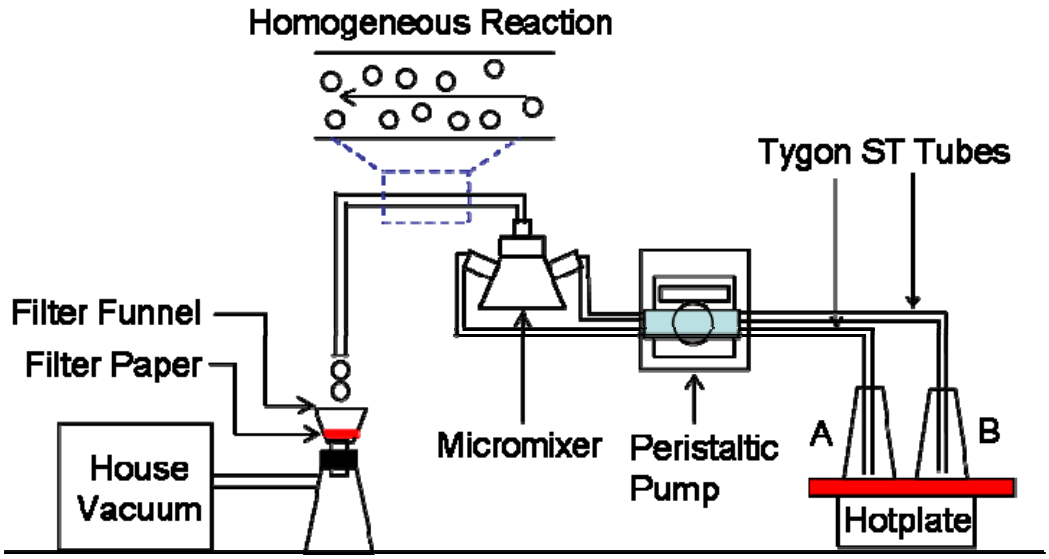

Figure 4.10 Schematic diagram of the experimental setup for studying the homogeneous reaction by a continuous flow microreactor.

Experiments were carried out to have a better understanding of the homogeneous reaction that takes place in the CBD reaction solution. TEM grids and oxidized silicon substrates were used to collect the solutions coming from different impinging fluxes of reactant streams after passing through the micromixer for growth study.

For our experimental operations, the reactant streams A and B were initially pre-heated to 80 ^{o}C (using VWR hotplate stirrer) then pumped through the Tygon ST tubes and allowed them to mix in the micromixer. While stream A consists of 24 ml of 0.0163 M $CdCl_2$, 20 ml of 0.196 M NH_4Cl, and 4 ml of 9.8 M NH_4OH, stream B consists of 24 ml of 0.163 M $SC(NH_2)_2$ and 26 ml of de-ionized water. The overall concentration of the reactants were 0.004 M $CdCl_2$, 0.04M

NH_4Cl, 0.04 M $SC(NH_2)_2$ and 0.4 M NH_4OH. The mixed solutions that had passed through the 10 cm Tygon ST tubing were collected on the TEM copper grids and were also deposited on oxidized silicon substrates for 1 min for comparison. Seven different mean residence times from 1, 3.5, 7, 35, 70, 140 to 280 sec after passing through the micromixer were used and obtained by changing the reactant flow rate.

For the preparation of transmission electron microscopy (TEM) samples were collected from the continuous flow microreactor at different residence times, a filter paper was first inserted inside a porcelain filter funnel (VWR) and then rinsed with de-ionized water followed by pinching a small hole in the center of the filter paper. This funnel was then pressed tightly on top of a flask using a rubber stopper and the flask was connected with the house vacuum through a plastic tube. The copper grid with thin lacey carbon film (Ted Pella, Inc) was placed on top of the filter paper with the small hole underneath the grid. The house vacuum was first turned on to hold the TEM copper grid. One drop of the hot solution came out from the reactor for a certain residence time and was collected on the TEM grid and dried immediately by vacuum sucking out the solution through the small hole to prevent the unwanted chemical reaction caused by the remaining solution.

4.3.2 Experimental Results

In order to further study and elucidate the formation of homogeneous particle growth, a series of TEM characterizations for samples collected at different residence times were performed. Samples prepared from one drop of the

hot solution came from the continuous flow microreactor at certain residence times and were collected on the copper grids and characterized by TEM (FEI Tecnai F20) at 200 KV. Solutions deposited on oxidized silicon substrates for 1 min were also performed and characterized by SEM (FEI Sirion XL30) at 5 KV for comparison.

Figure 4.11(a) shows the CdS clusters and small nanoparticles deposited along the copper grid with thin lacey carbon film for 1 sec residence time with particle size around 10 to 20 nm. The blown-up image from the dashed area of Figure 4.11(a) is shown in Figure 4.11(b). Due to using the pre-heated precursor solution, thiourea was seen to release more sulfide ions at a higher temperature through a hydrolysis reaction. Those free sulfide ions reacted with free cadmium ions to form CdS particles in the reaction solution and further deposited on the copper grid. The corresponding SEM micrograph for 1 min deposition time is shown in Figure 4.11(c). The formation of CdS clusters and small nanoparticles were observed from TEM characterization and cannot be seen clearly here; this might be due to the resolution of SEM micrograph or part of them may have been removed through the post rinsing and drying processes.

(a)

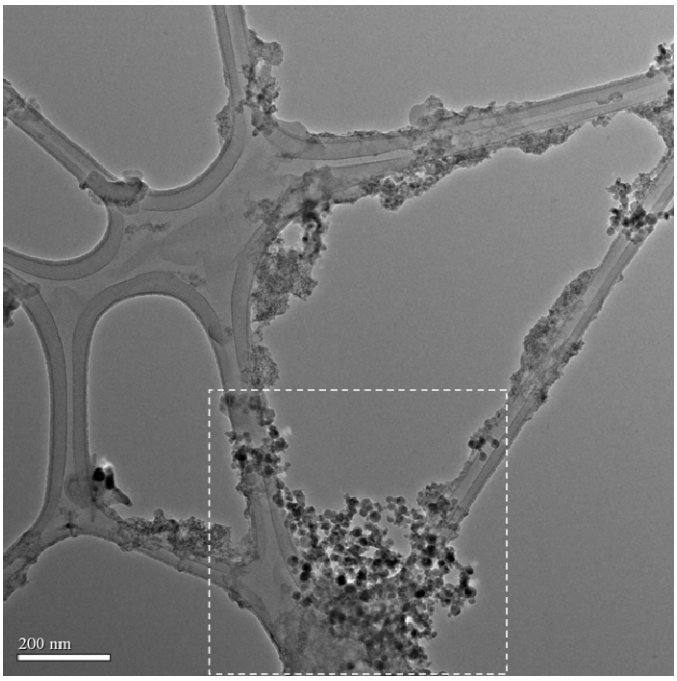

(b)

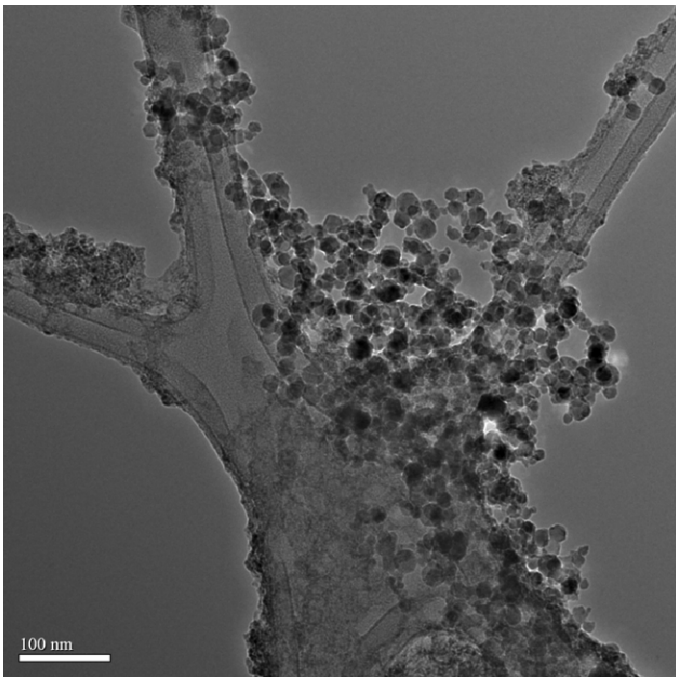

(c)

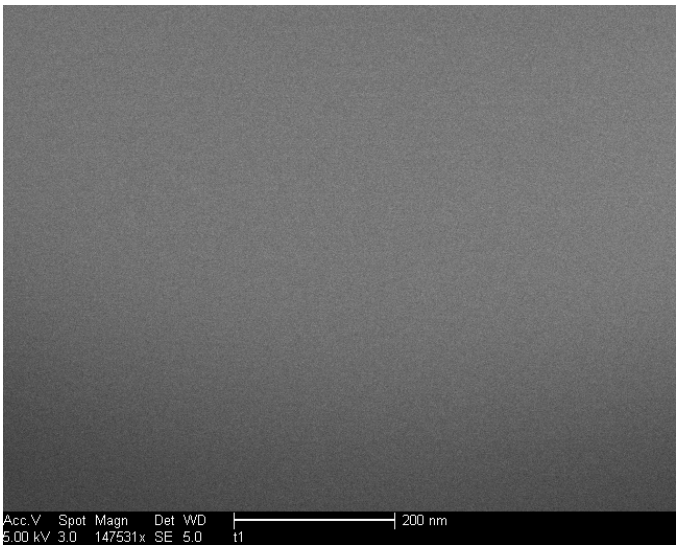

Figure 4.11 (a) TEM micrograph of CdS nanoparticles deposited by a continuous flow microreactor with a residence time of 1 sec, (b) a blown-up image from the dashed area of (a), and (c) the corresponding SEM micrograph.

When increasing the residence time to 3.5 sec, CdS nanoparticles will grow bigger while traveling inside the tube before impinging on the grid. Larger nanoparticles (~30 to 50 nm) were observed from a TEM micrograph, and they tended to connect and aggregate with each other as shown in Figure 4.12(a). The blown-up image from the dashed area of Figure 4.12(a) is shown in Figure 4.12(b). The corresponding SEM micrograph for 1 min deposition time is shown in Figure 4.12(c). The CdS nanoparticles observed from TEM characterization might have been removed through the post rinsing and drying processes. Therefore, they cannot be seen clearly here.

(a)

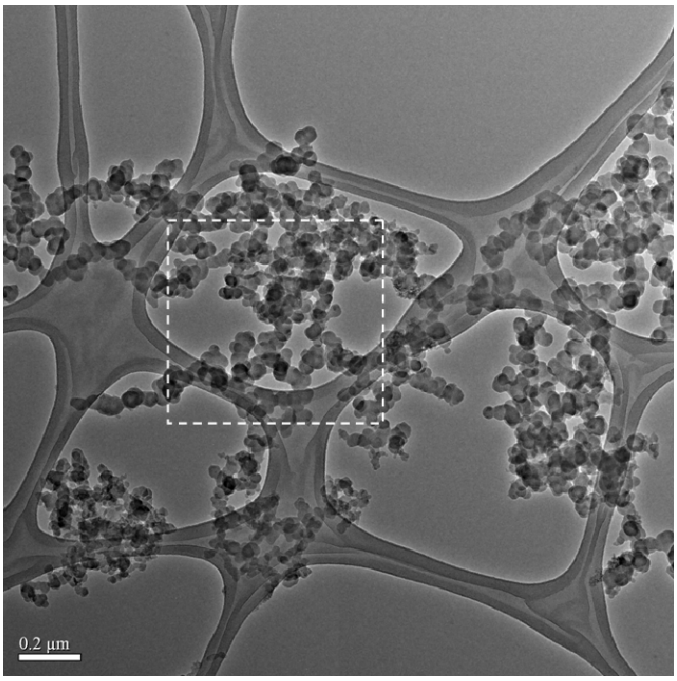

(b)

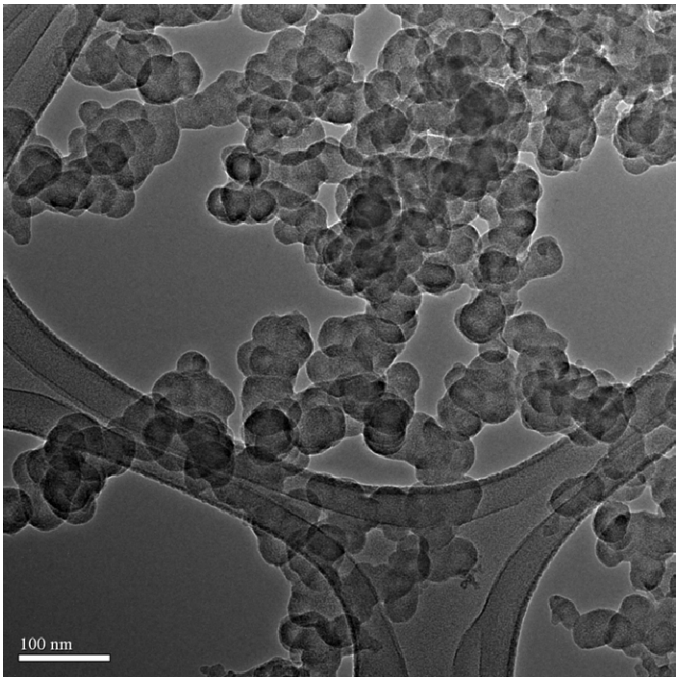

(c)

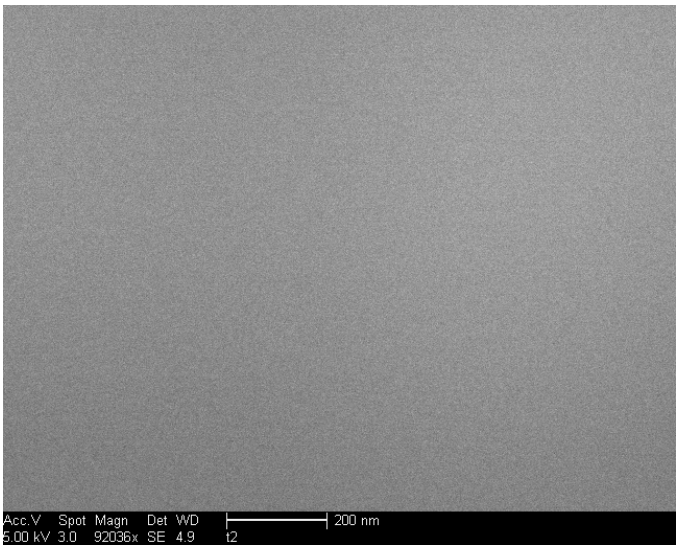

Figure 4.12 (a) TEM micrograph of CdS nanoparticles deposited by a continuous flow microreactor with a residence time of 3.5 sec, (b) a blown-up image from the dashed area of (a), and (c) the corresponding SEM micrograph.

CdS nanoparticles will continue to grow bigger inside the tube before impinging on the grid with residence time of 7 sec. A chain-like nanoparticle aggregation was observed in TEM micrograph (Figure 4.13(a)) which is well match to the corresponding SEM micrograph showing in Figure 4.13(b). At this reaction condition, spherical nanoparticles with diameter in the range from around 30 to 100 nm were clearly observed showing in dashed area of Figure 4.13(a).

(a)

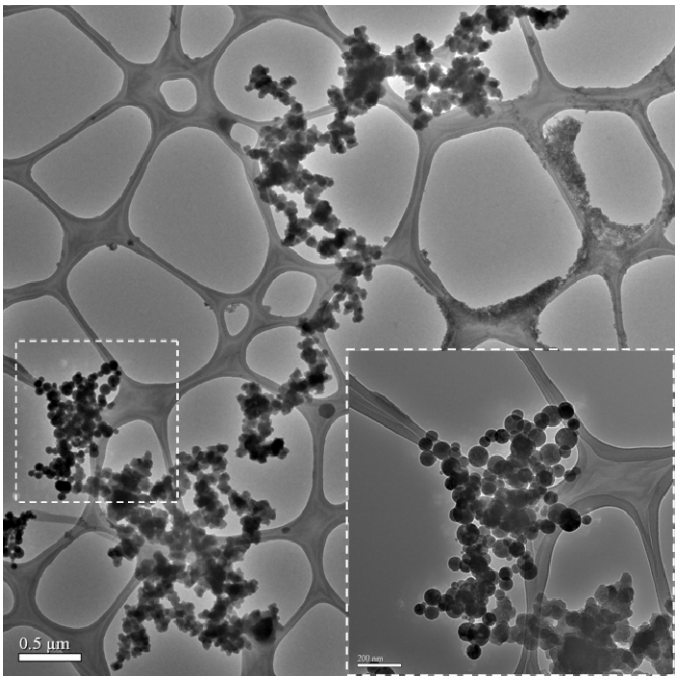

(b)

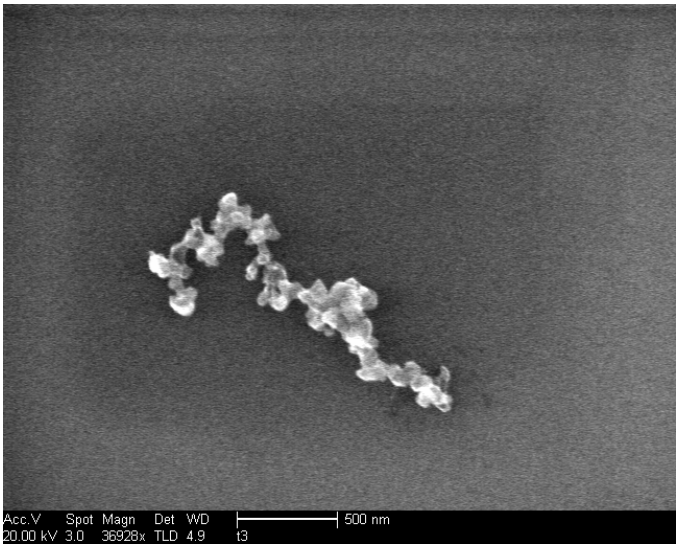

Figure 4.13 (a) TEM micrograph of CdS nanoparticles deposited by a continuous flow microreactor with a residence time of 7 sec including a blown-up image from the dashed area (inset) and (b) the corresponding SEM micrograph.

When residence time of 35 sec was applied, CdS nanoparticles were further aggregated and started to agglomerate together showing in Figure 4.14(a). The similar result was also observed from corresponding SEM micrograph shown in Figure 4.14(b).

(a)

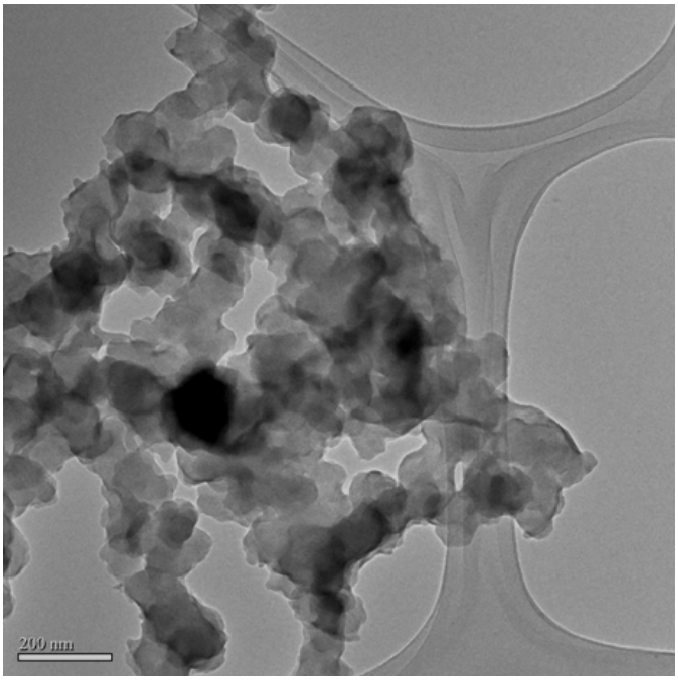

(b)

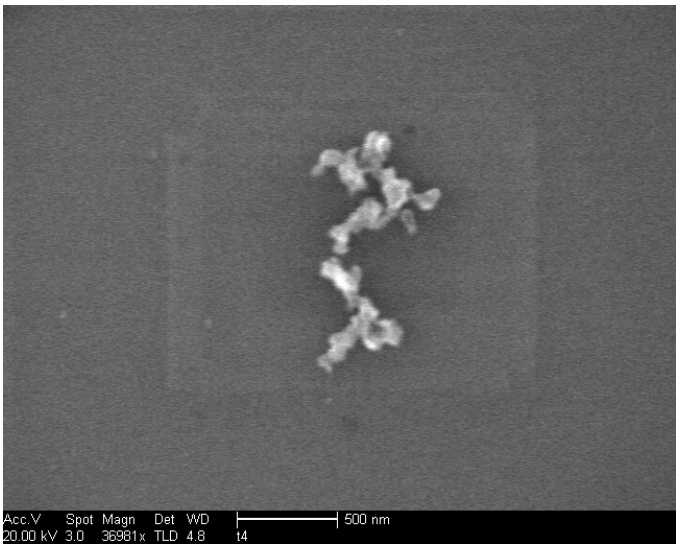

Figure 4.14 (a) TEM micrograph of aggregated CdS nanoparticles deposited by a continuous flow microreactor with a residence time of 35 sec and (b) the corresponding SEM micrograph.

Figure 4.15(a) shows the continuing agglomeration of CdS nanoparticles with a blown-up image from the dashed area (inset) when residence time of 70 sec was used. The agglomeration of CdS nanoparticles was also observed from the corresponding SEM micrograph shown in Figure 4.15(b). While in certain areas, some CdS nanorods with lateral size in a range of 30-70 nm combined with aggregated nanoparticles were observed showing in Figure 4.15(c)

(a)

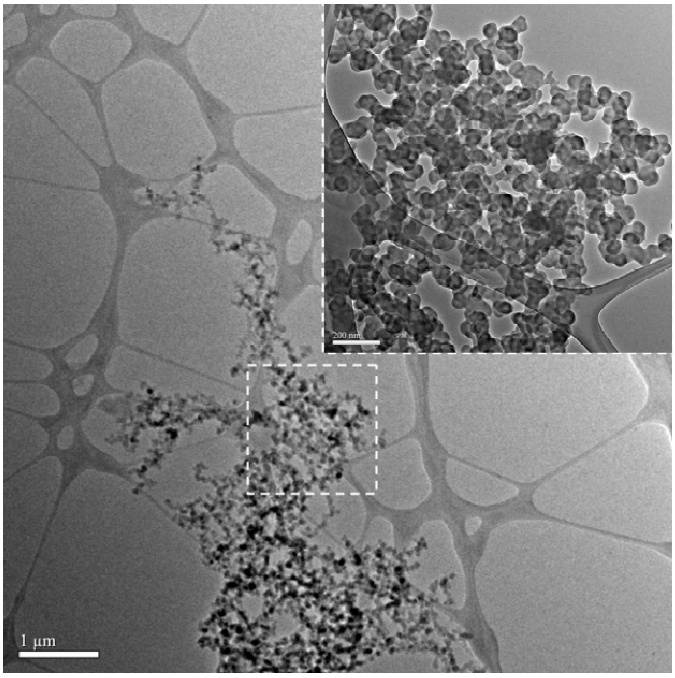

(b)

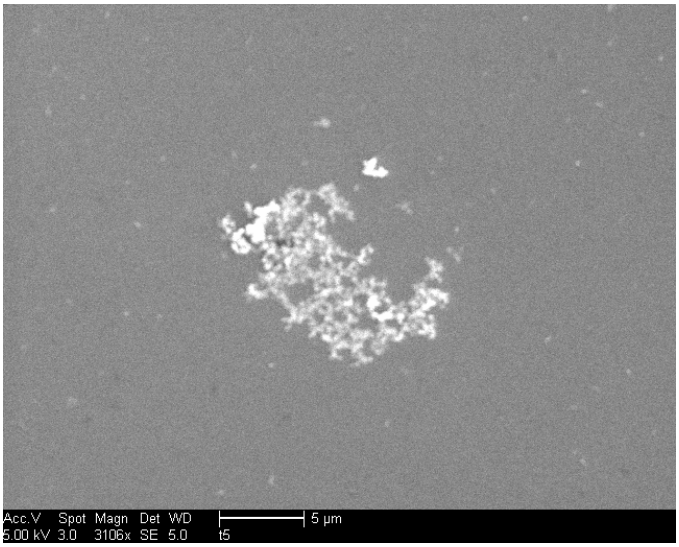

(c)

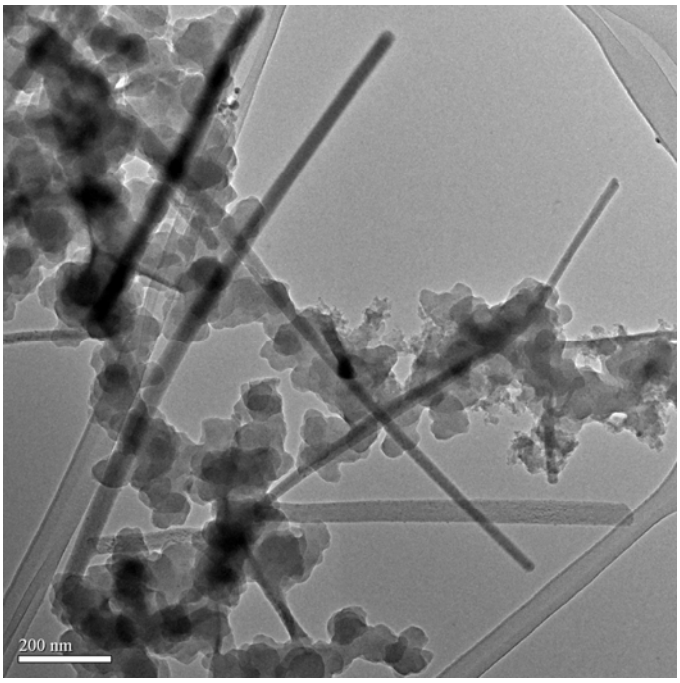

Figure 4.15 (a) TEM micrograph of agglomerated CdS nanoparticles with a blown-up image from the dashed area (inset) deposited by a continuous flow microreactor with a residence time of 70 sec, (b) the corresponding SEM micrograph, and (c) CdS nanorods formation.

When increasing the residence time to 140 sec, these nanoparticles were further aggregated and agglomerated together. The observed CdS thin films (Figure 4.16(a)) might be contributed to those agglomerated CdS nanoparticles first deposited inside the wall of the tube then washed away through the forthcoming reactant solution and further deposited on the TEM grid. The further agglomeration of CdS nanoparticles was also observed from the corresponding

SEM micrograph shown in Figure 4.16(b). The formation of arrayed CdS nanorod bundle structure was also observed in certain area shown in Figure 4.16(c).

(a)

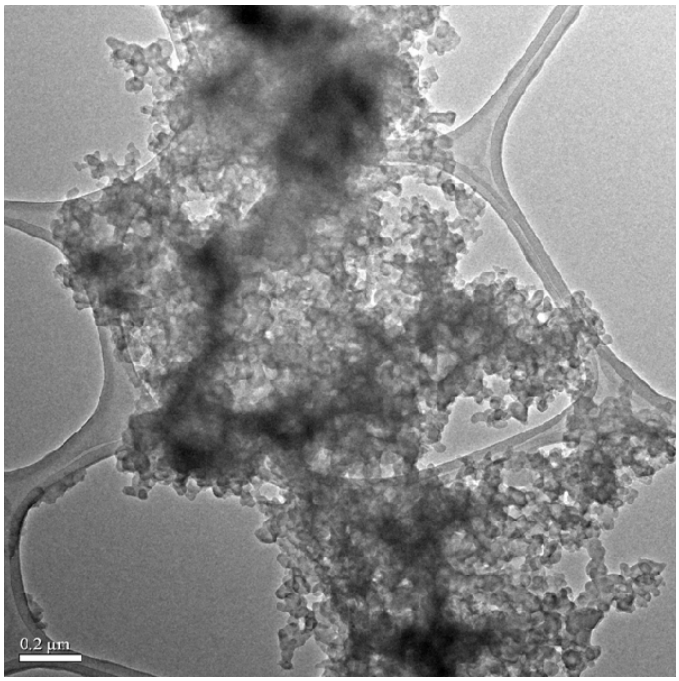

(b)

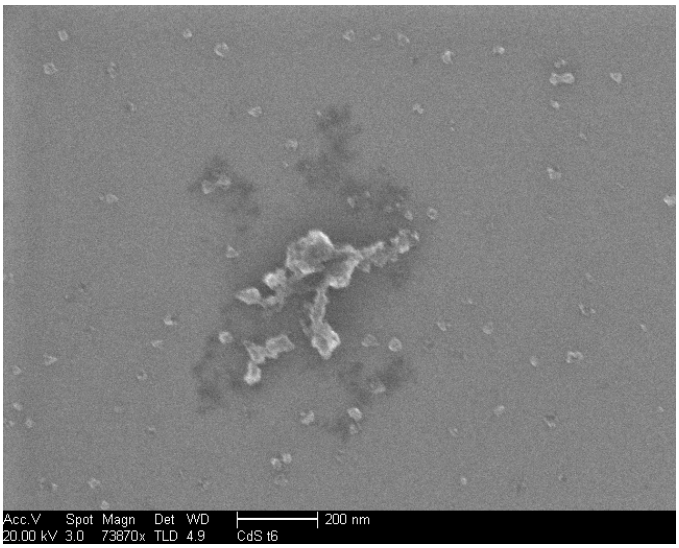

(c)

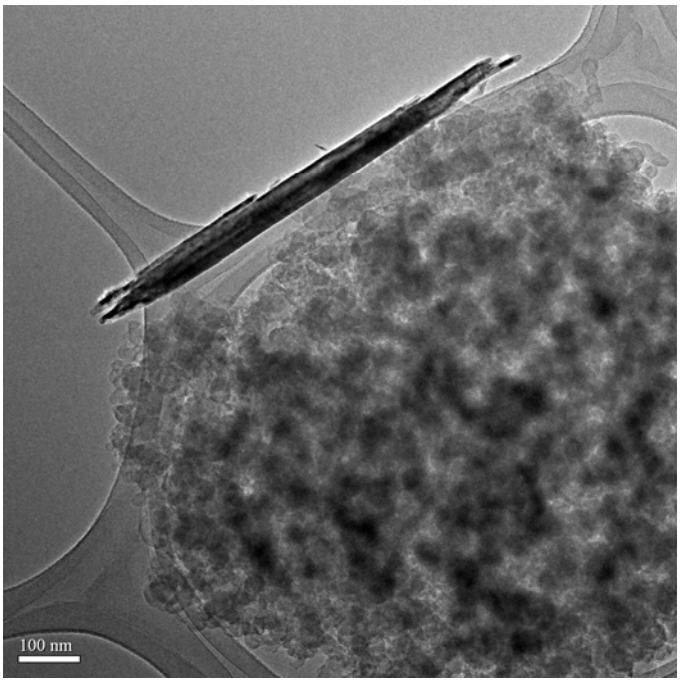

Figure 4.16 (a) TEM micrograph of agglomerated CdS nanoparticles deposited by a continuous flow microreactor with a residence time of 140 sec, (b) the corresponding SEM micrograph, and (c) CdS nanorod bundle structure formation.

The formation of CdS nanorods and arrayed nanorod bundle structures using the CBD recipe were observed in certain areas and reported here for the first time. The CdS nanoparticles have been assembled into CdS nanorods and arrayed nanorod bundles by a thioglycolic acid (TGA) assisted hydrothermal processes using sodium sulfide (Na_2S) and thiourea ($SC(NH_2)_2$) as the sulfur source, respectively [69]. They believed that the CdS nanorods were formed through the cluster-to-cluster oriented attachment mechanism, while the CdS nanorod bundles were formed through the particle-to-particle oriented attachment mechanism. The

effects of four major factors on the shape of CdS structure formed by hydrothermal processs have also been investigated from the same group [70]. Different studies of CdS nanocrystals were also reported in the literatures such as CdS nanoparticles [71], CdS nanorod [72-76], and CdS nanowire [77]. By controlling the growth of semiconductor materials to nanoparticles, nanorods, and nanolayer forms allows it to tailor the optical, structure, and electrical properties of materials [78].

While using a 280 sec residence time, the CdS thin films were formed from those amassed agglomeration of nanoparticles shown in Figure 4.17(a). The SEM image (Figure 4.17(b)) further supports the result observed from a TEM micrograph.

(a)

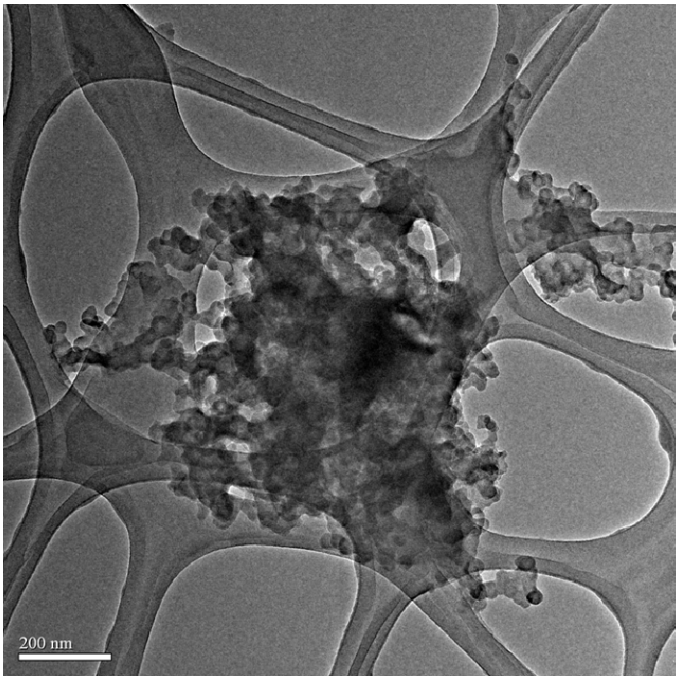

(b)

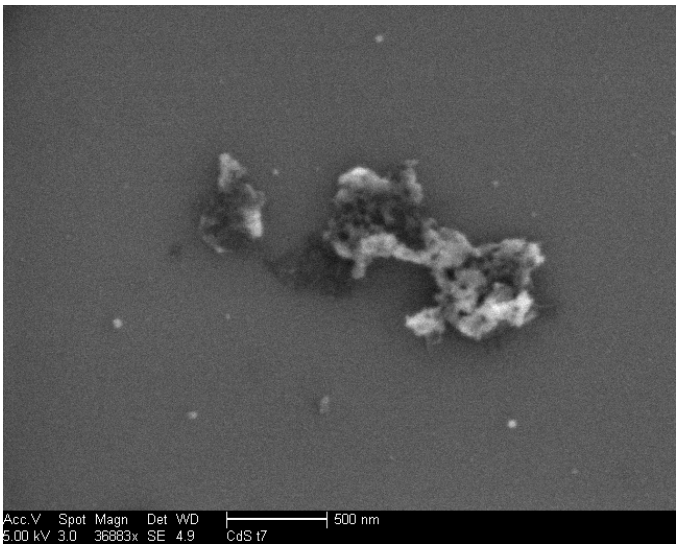

Figure 4.17 (a) TEM micrograph of amassed CdS nanoparticles deposited by a continuous flow microreactor with a residence time of 280 sec and (b) the corresponding SEM micrograph.

Based on the experimental results characterized by TEM and SEM, three transition periods can be observed for the CdS homogeneous reaction by providing a temporal control (from 1 to 280 sec) using a continuous flow microreactor. The first period is for the homogeneous particle formation when the residence times of 1, 3.5 and 7 sec were used. Size increasing CdS nanoparticles (from ~10 to 100 nm) and further connections with each other grown by homogeneous reactions were clearly observed from the TEM and corresponding SEM micrographs using pre-heated precursor solutions. The second period is for the aggregation and agglomeration of nanoparticles when the residence times of 35 and 70 sec were applied. During this period, the individual nanoparticles are hard to find but rather

aggregate and start to agglomerate together. The third period is for the thin film formation when the residence times of 140 and 280 sec were used. While in this period, CdS thin films were formed through amassed aggregation and agglomeration of nanoparticles that first deposited inside the wall of the tube then washed away through the forthcoming reactant solution and further deposited on the TEM grid. The formation of CdS nanorod bundles were observed for a 140 sec residence time, and these boundles could form through the nanorods oriented attachment.

CHAPTER 5

THIN FILM DEPOSITION AND GROWTH KINETICS

5.1 Background

A series of CdS thin film deposition experiments were carried out by altering the residence times, thiourea concentrations, temperatures of the impinging chemical solution and substrate.

5.2 Experimental Setup

The continuous flow microreactor used for this study consists of a microprocessor-controlled peristaltic pump (Ismatec REGLO Digital) for pumping each reactant stream through a 1.22 mm ID Tygon ST tube (Upchurch Scientific), while stream A consists of 60 ml of 0.0163 M $CdCl_2$, 50 ml of 0.196 M NH_4Cl, and 10 ml of 9.8 M NH_4OH and stream B consists of 60 ml of 0.163 M $SC(NH_2)_2$ and 65 ml of de-ionized water. The overall concentration of the reactants are 0.004 M $CdCl_2$, 0.04 M NH_4Cl, 0.04 M $SC(NH_2)_2$, and 0.4 M NH_4OH. An optical image of the continuous flow microreactor for CBD investigation is shown in Figure 5.1.

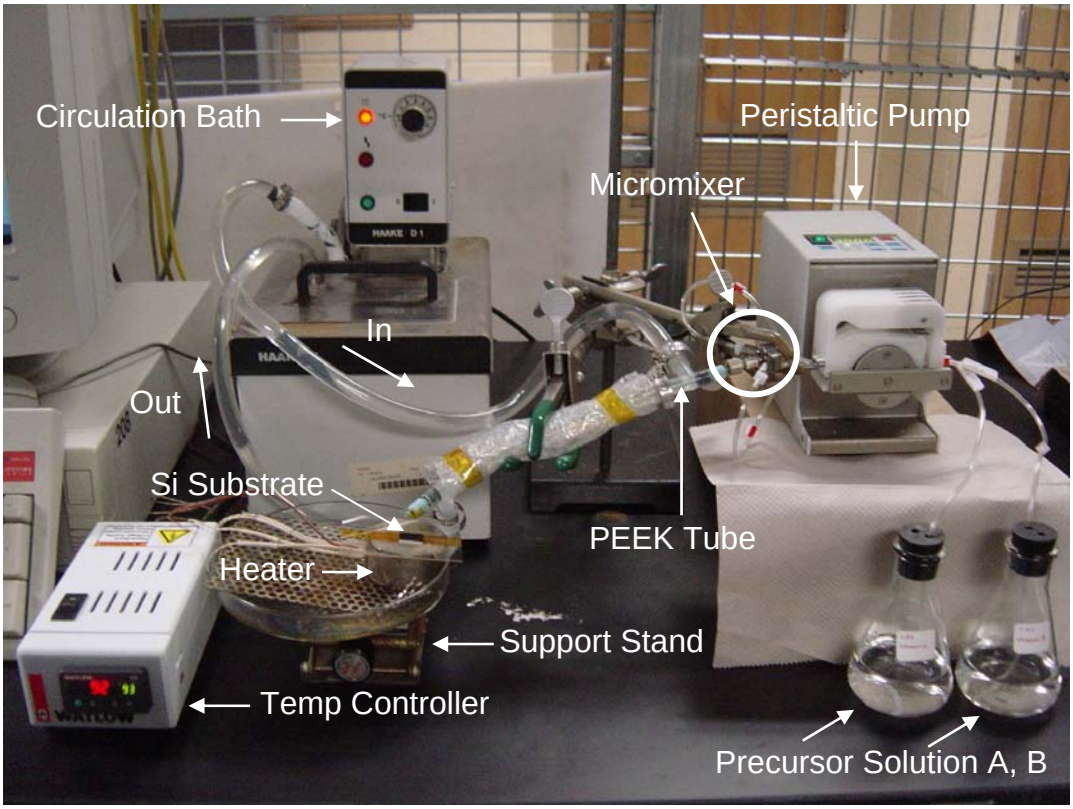

Figure 5.1 An optical image of the continuous flow microreactor for CBD investigation.

After the reactant solutions were mixed by an interdigital micromixer, the resulting mixtures were then passed through a ~26.5 cm polycaryl-ether etherketone (PEEK) tube (1/16 in. OD, 0.03 in. ID from Upchurch Scientific), which was immersed inside a PVC plastic tube filled with hot water maintained at a desired temperature controlled by a circulation water bath. A foam sheet was wrapped outside the plastic tube and used to prevent the heat loss.

The nanoparticles in the chemical solutions after mixing were characterized by TEM by collecting drops of solution on top of a copper TEM grid

(with thin lacey carbon film). TEM characterizations were performed using a FEI Tecnai F20 at 200 KV. The detail TEM sample preparation procedure was discussed in section 4.3.

Oxidized silicon substrates (silicon wafer coupons) measuring 15 x 10 mm were used for deposition studies. The coupons were initially sonicated in an ultrasonic bath using 1M NaOH for about 15 minutes and then cleaned according to a standard acetone, methanol, and DI water (AMD) procedure. Finally, they were dried under a stream of nitrogen gas before being used for deposition.

The film morphology was characterized by SEM (FEI Sirion XL30) at 5 KV and the film thickness was characterized by 3D Dektak 8 surface profiler (Veeco).

The solution was impinged on the substrate which was taped onto a 3 x 1 in. microscope glass slide and heated on a hotplate (2 in. diameter x 0.75 in. thick SS disk from Watlow) with a digital temperature controller at a desired temperature. The peristaltic pump was operated at a flow rate of 3, 1, 0.5, 0.1, and 0.05 ml/min in order to have the mean residence time of the mixtures after passing through the micromixer for 1, 3.5, 7, 35, and 70 seconds, respectively. Once completing the deposition process, the substrate was immediately rinsed with Millipore DI water and dried under a stream of nitrogen gas then removed from the slide. After deposition, no further post annealing process was performed.

5.3 Experimental Results

5.3.1 CdS Deposition Kinetics

Previous results indicated that for a CBD CdS deposition, the small particles were forming and growing even at the beginning of the deposition process and supported by real time dynamic light scattering and TEM characterization [5]. To have the deposition without the CdS particle formation, two approaches can be conducted:

1. Control the product of the concentration of dissolved ions, $[Cd^{2+}]$ x $[S^{2-}]$, to be less than the solubility product, K_{sp}, of CdS (10^{-25}).
2. Carry out the deposition by using a flux within the induction time scale.

An impinging flux without the homogeneous particle formation can be obtained from a short residence time of 1 sec with the solution temperature maintained at 80 ^{o}C using a continuous flow microreactor. A TEM sample was prepared by collecting the hot solution from the PEEK tube for 2 drops on top of the copper grid (with a thin lacey carbon film). The TEM characterization (Figure 5.2) indicated at this processing condition that there was no evidence of any particle formation on the surface of the grid and the reaction was carried out within the induction time scale. Using this particle-free flux, the study of the CdS deposition kinetics can be simplified by focusing on the heterogeneous surface reaction through a molecule-by-molecule growth mechanism.

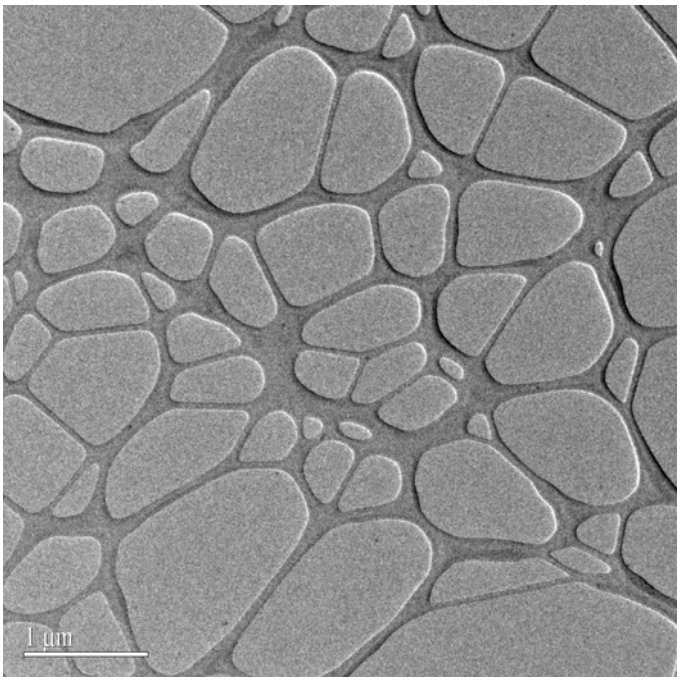

Figure 5.2 TEM micrograph showing absence of homogeneous CdS particle formation from a particle-free flux (residence time of 1 sec) using a continuous flow microreactor.

Figure 5.3 shows the average CdS thin film thickness of 90, 200, 350, and 800 Å obtained at deposition time of 1, 3, 5, and 10 mins, respectively for a mean residence time of 1 sec.

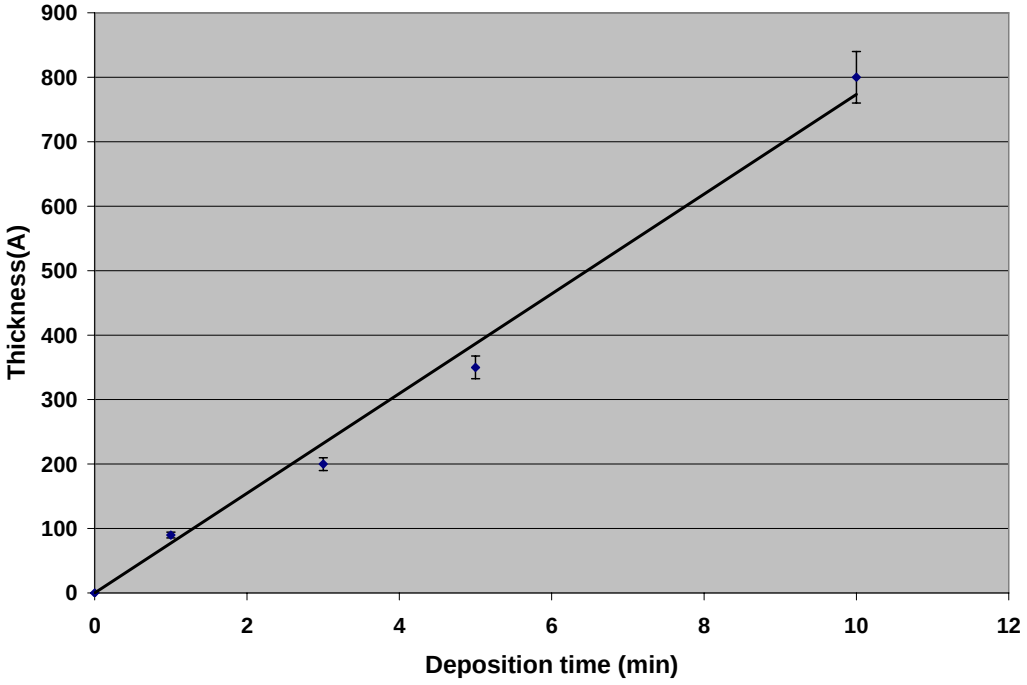

Figure 5.3 Average CdS thin film thickness versus deposition time for a mean residence time of 1 sec.

Figure 5.4 shows the SEM micrographs of CdS thin films deposited using a 1 sec mean residence time flux for (a) 1, (b) 3, (c) 5, and (d) 10 mins, respectively. Thin and rather smooth CdS thin films were found for deposition times of 1, 3, and 5 mins. After a 10-min deposition time, CdS nanocrystals of size around 40 to 50 nm in diameter formed through the heterogeneous reaction on the substrate surface and could be clearly observed.

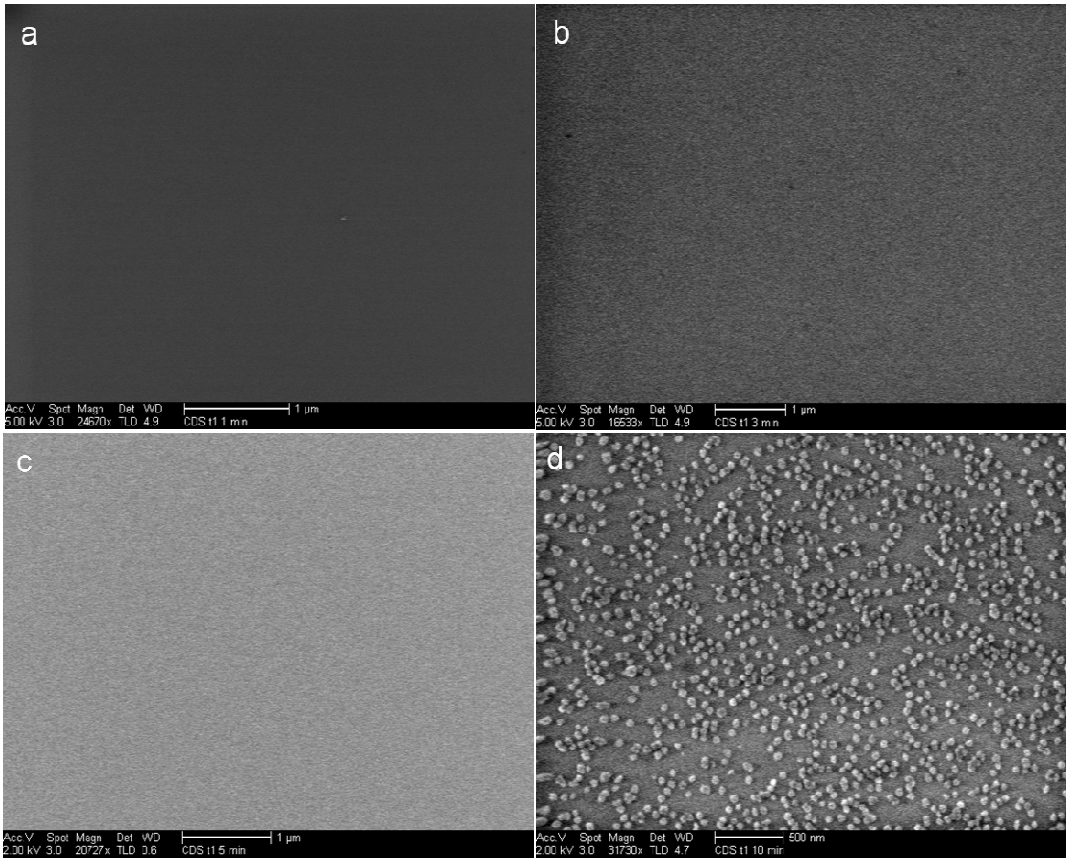

Figure 5.4 SEM micrographs of CdS thin films deposited at a mean residence time of 1 sec for (a) 1, (b) 3, (c) 5, and (d) 10 mins, respectively.

Our continuous flow microreactor provides the capability of decoupling the homogeneous particle formation and deposition from the molecular level heterogeneous surface reaction. This leads to an opportunity to study the fundamental growth kinetics operated in a particle-free regime. Based on previous characterization results (Figure 5.2), no homogenous particle formation was observed from the TEM micrograph with a mean residence time of 1 sec.

For a given condition, the thin film growth rate depends only on the variation of reagent concentration and can be expressed as:

$$r = k*[reag]^n \quad [5.1]$$

where k is the reaction rate constant, [reag] is the initial reagent concentration and n is the reaction order of this reagent. We can obtain the reaction order for each reagent from the slope of the linear fit of the log r versus log [reag].

In order to obtain an empirical rate equation of CdS thin film deposition using a particle-free deposition flux, the empirical rate equation (equation 2.8) proposed by Ortega-Borges *et al* [27] was used. For obtaining the reaction order of the thiourea concentration, CdS thin film depositions using thioura concentrations, [Tu], of 0.01, 0.015, 0.02, 0.03, and 0.04 M were performed and kept the rest of reaction conditions the same (0.004 M $CdCl_2$, 0.04 M NH_4Cl, and 0.4 M NH_4OH). Table 5.1 shows the average thin film thickness deposited by different thiourea concentrations and deposition times for a 1-sec residence time using the continuous flow microreactior.

Table 5.1 Average CdS thin film thicknesses deposited by different thiourea concentrations and deposition times for a 1-sec residence time.

	Average CdS thin film thicknesses (Å) for different thiourea concentrations				
Deposition time (min)	0.01 M	0.015 M	0.02 M	0.03 M	0.04 M
1	40	50	60	80	90
3	100	120	140	180	200
5	150	200	250	310	350
10	280	370	480	650	800

The deposition data from Table 5.1 were plotted in Figure 5.5 showing the deposited CdS thin film thickness versus the deposition time for different thiourea concentration values. The fitted linear regression lines were also plotted to obtain each individual growth rate values for different thiourea concentrations and are shown in Table 5.2.

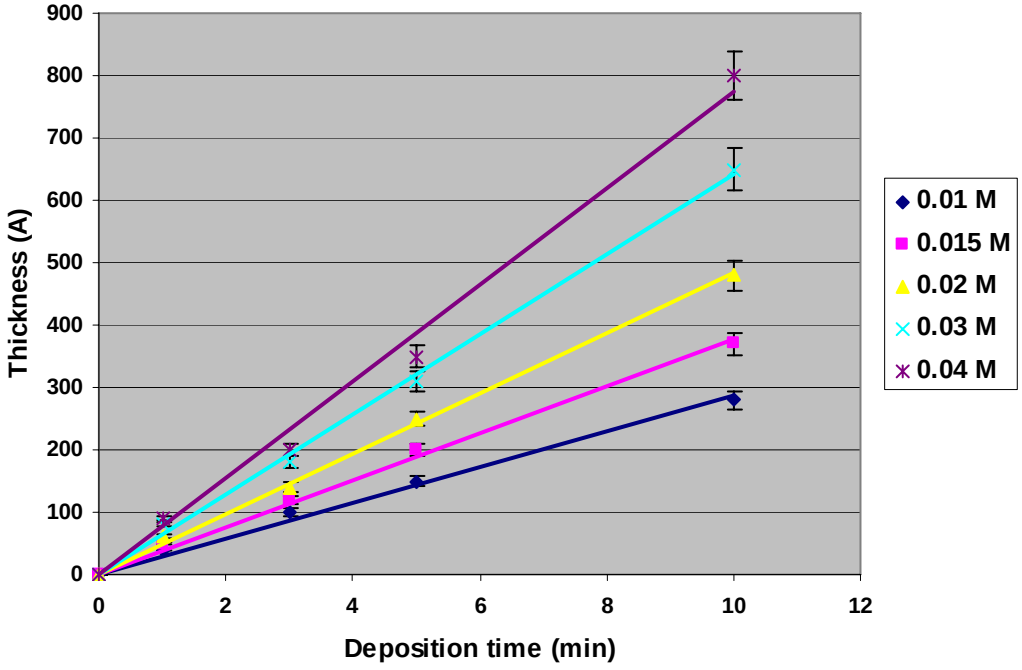

Figure 5.5 CdS thin film thickness versus deposition time for different thiourea concentrations.

Table 5.2 CdS thin film growth rates obtained from a 1-sec residence time for different thiourea concentrations.

Thiourea concentration (M)	0.01	0.015	0.02	0.03	0.04
Growth rate (Å/min)	28.815	37.852	48.37	64.222	77.333

From Table 5.2, we can observe that the thin film growth rate increases with the thiourea concentrations. The reaction order for thiourea concentration can be obtained from the slope of the linear fit of the log r versus log [Tu] showing in

Figure 5.6. In this case, the reaction order for the thiourea concentration is about 0.72.

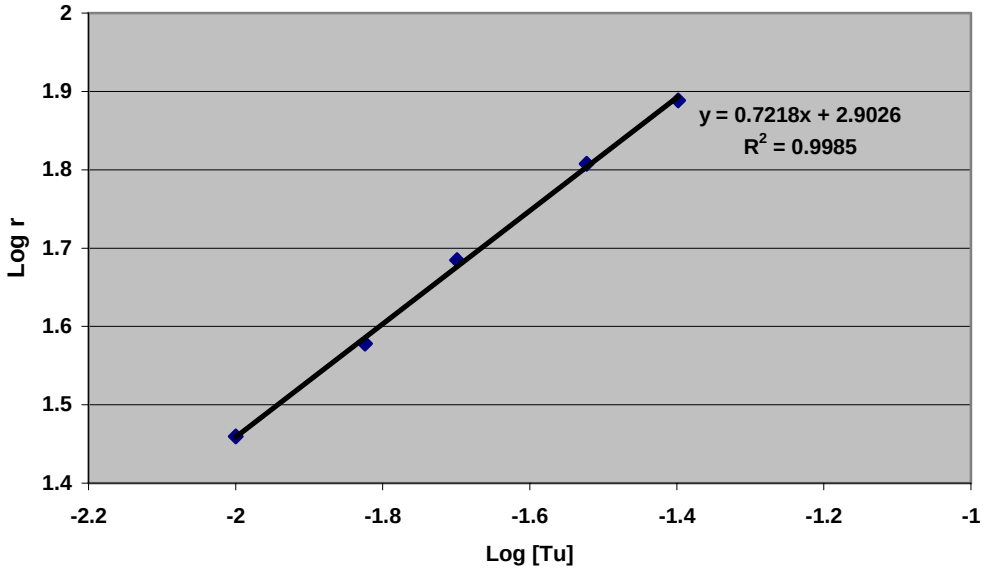

Figure 5.6 Logarithm of the growth rate as a function of log [Tu] for 1 sec residence time for different thiourea concentrations.

The obtained reaction order for thiourea concentration was compared with the previous results from Ortega-Borges *et al*. [27] based on initial rate studies using QCM. They arrived at the following empirical rate equation (equation 2.8):

$$\mathrm{r}(\mu\mathrm{m/h}) = K\frac{[\mathrm{Cd}]^{0.6}[\mathrm{SC(NH_2)_2}]^{0.8}}{[\mathrm{NH_3}]^{3.3}[\mathrm{H^+}]^{1.5}} \qquad [2.8]$$

with $K = 10^{-14.7}$

Our experimental value of 0.72 is close to their empirical reaction order of 0.8 obtained from the initial growth rate (linear part of the growth curve) for thiourea concentration.

If we only change the reaction order of thiourea concentration from 0.8 to 0.72 but still keep the same reaction orders for the rest of the reagent concentrations in the empirical rate equation (equation 2.8), the new empirical rate law based on our experimental data can be presented as equation 5.2.

$$r(\mu m/h) = K \frac{[Cd]^{0.6}[SC(NH_2)_2]^{0.72}}{[NH_3]^{3.3}[H^+]^{1.5}} \qquad [5.2]$$

where [Cd] is the total cadmium concentration, $[SC(NH_2)_2]$ is the total thiourea concentration and $[NH_3]$ is the total ammonia concentration. The total ammonia concentration is defined as:

$$[NH_3] = [NH_3]^o + [NH_4^+]^o \qquad [5.3]$$

The temperature dependence of the CdS thin film growth rate was studied in the range from 60 to 80 ^oC in steps of 5 ^oC. Table 5.3 shows the average thin film thickness deposited at different temperatures and deposition times for a 1-sec residence time.

Table 5.3 Average CdS thin film thicknesses deposited at different temperatures and deposition times for a 1-sec residence time.

	Average CdS thin film thicknesses (Å) at different temperatures				
Deposition time (min)	60 ^{o}C	65 ^{o}C	70 ^{o}C	75 ^{o}C	80 ^{o}C
1	30	40	60	80	90
3	100	130	150	180	200
5	170	200	250	300	350
10	330	370	480	600	800

The deposition data from Table 5.3 were plotted in Figure 5.7 showing the deposited CdS thin film thickness versus the deposition time at different operating temperatures. The fitted linear regression lines were also plotted to obtain each individual growth rate values at different operating temperatures and are shown in Table 5.4.

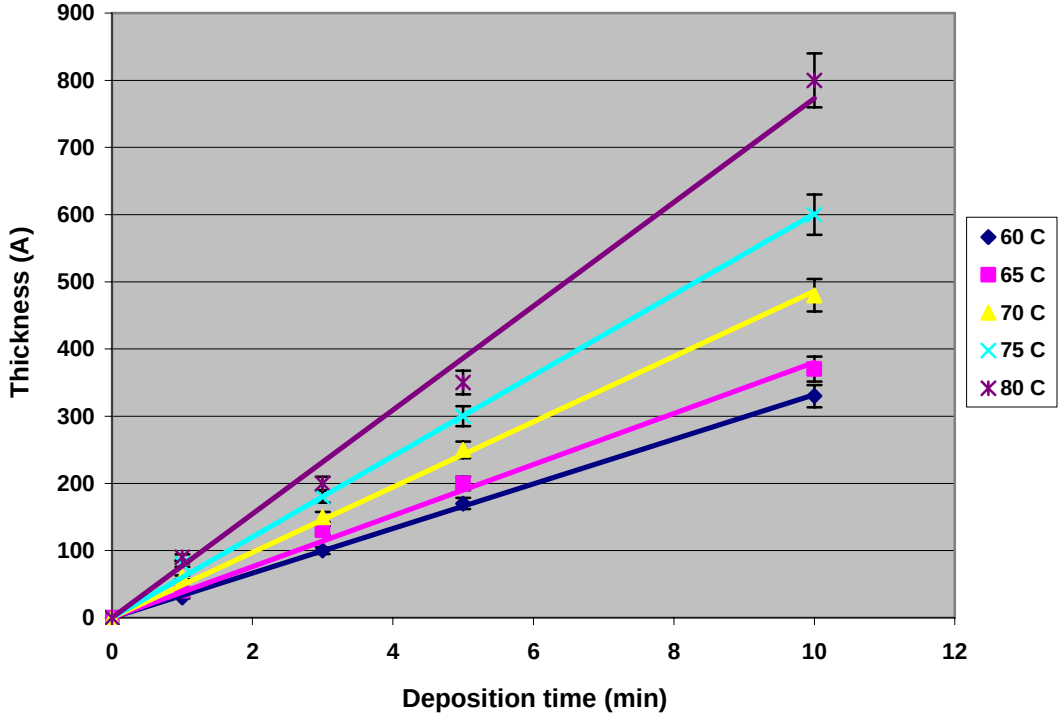

Figure 5.7 CdS thin film thickness versus deposition time at different operating temperatures for a 1-sec residence time.

Table 5.4 CdS thin film growth rates obtained from a 1-sec residence time at different operating temperatures.

Temperature (^{o}C)	60	65	70	75	80
Growth rate (Å/min)	33.185	38.0	48.593	66.074	77.333

The rate constant, K can be calculated from equation 5.4 using the growth rate of CdS thin film obtained from a 1-sec residence time for a reaction condition of 0.004 M $CdCl_2$, 0.04 M NH_4Cl, 0.04 M $SC(NH_2)_2$, and 0.4 M NH_4OH operated at different temperatures shown in Table 5.4 for the continuous flow microreactor.

$$r(\mu m/h) = K\frac{(0.004)^{0.6}(0.04)^{0.72}}{(0.4+0.04)^{3.3}(10^{-14}/10^{-3})^{1.5}} \quad [5.4]$$

Table 5.5 shows the calculated rate constants for CdS thin film deposition operated at different temperatures using the continuous flow microreactor for a 1-sec residence time.

Table 5.5 Calculated rate constants for CdS thin film deposition operated at different temperatures using the continuous flow microreactor for a 1-sec residence time.

Temperature (^oC)	60	65	70	75	80
Growth rate (Å/min)	33.185	38.0	48.593	66.074	77.333
Growth rate (μm/h)	1.991	2.280	2.916	3.964	4.640
Rate constant	1.169E-15	1.338E-15	1.712E-15	2.327E-15	2.724E-15

The rate constant value increased with the operating temperature. The rate constant value of 1.169E-15 at 60 ^oC is smaller than the previous reported value of $K = 10^{-14.7}$ (1.995E-15) that was obtained from the same operating temperature for batch CBD CdS deposition [27].

5.3.2 Effects of Residence Time

In order to observe the surface morphology changes of CdS thin films by altering the impinging fluxes, a series of CdS thin film deposition experiments using deposition flux at different residence times (1, 3.5, 7, 35, and 70 seconds) were performed at 80 ^{o}C for both solution and substrate temperature. The film morphology was characterized by SEM (FEI Sirion XL30) at 5 KV and the film thickness was characterized by 3D Dektak 8 surface profiler (Veeco).

Table 5.6 shows the average CdS thin film thickness deposited on silicon coupon substrates by different residence times and deposition times.

Table 5.6 Average CdS thin film thicknesses deposited by different residence times and deposition times.

	Average CdS thin film thicknesses (Å) for different residence times				
Deposition time (min)	1 sec	3.5 sec	7 sec	35 sec	70 sec
1	90	200	250	400	480
3	200	850	1000	1200	800
5	350	1300	1500	1800	1400
10	800	3000	3400	3800	3300

The thickness data from Table 5.6 was further plotted in Figure 5.8 showing the deposited CdS thin film thickness versus the deposition time at different residence times. The fitted linear regression lines were also plotted to

obtain each individual growth rate values for different residence times and are shown in Table 5.7.

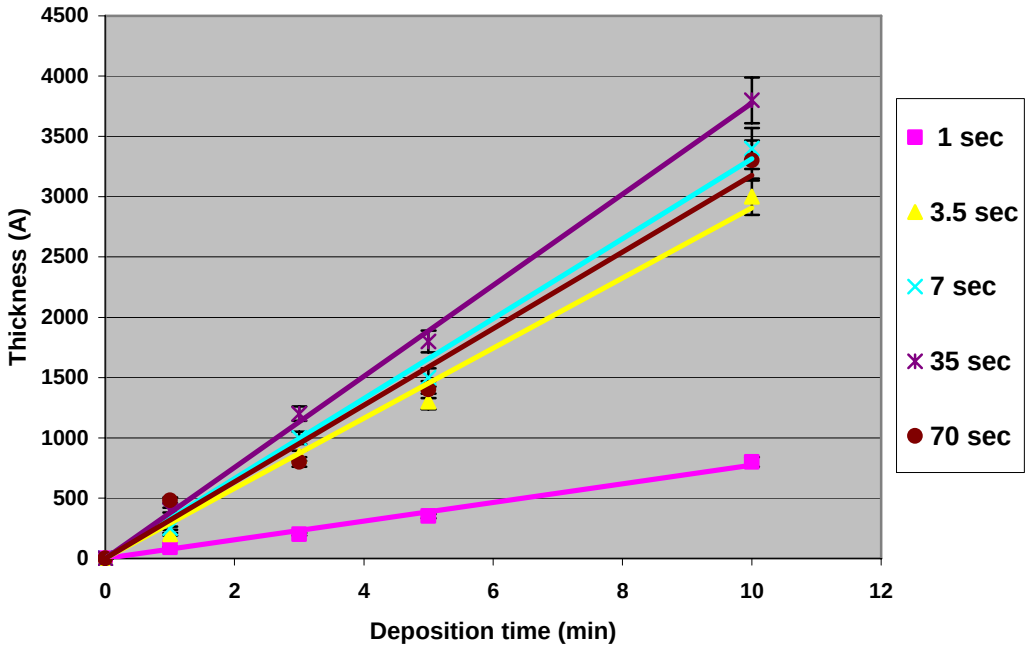

Figure 5.8 CdS thin film thickness versus deposition time for different residence times.

Table 5.7 CdS thin film growth rates obtained from different residence times.

Residence Time (sec)	1	3.5	7	35	70
Growth rate(Å/min)	77.33	290.74	331.48	377.78	317.63

The growth rate data from Table 5.7 was further plotted in Figure 5.9 showing the CdS thin film growth rate versus the residence time.

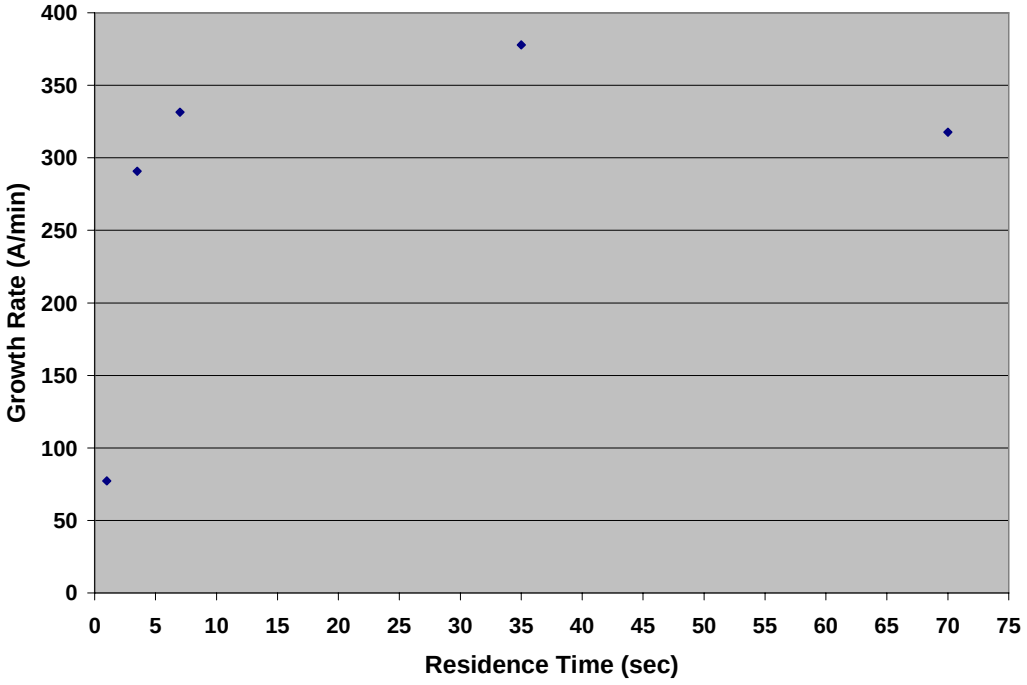

Figure 5.9 CdS thin film growth rate versus the residence time.

From Table 5.7 and Figure 5.9, the growth rate results clearly indicated that a very low CdS thin film growth rate was obtained (~77 Å/min) when a 1-sec residence time was used. The growth rate initially increased very fast (about 4 times higher) when a 3.5 residence time was used compared to a 1-sec one. After that, the thin film growth rate increased relatively slow from a 3.5 to a 35 sec residence time. However, when a 70 sec residence time was applied, the decrease of the growth rate was observed.

The deposited films using different flux at different deposition times were characterized by SEM and given from Figure 5.10 to Figure 5.13.

When a 3.5-sec residence time was used, we can clearly see lots of CdS nanocrystals grown on the substrate surface even for a 1-min deposition time from the SEM micrograph (Figure 5.10(a)). This result can not be seen from the very short residence time of 1 sec that was discussed previously. When longer deposition times were used (3, 5, and 10 mins), the larger nanocrystals in size and dense and compact films could be observed (Figure 5.10(b), (c), and (d), respectively). These results were getting more obvious as the deposition time was increased.

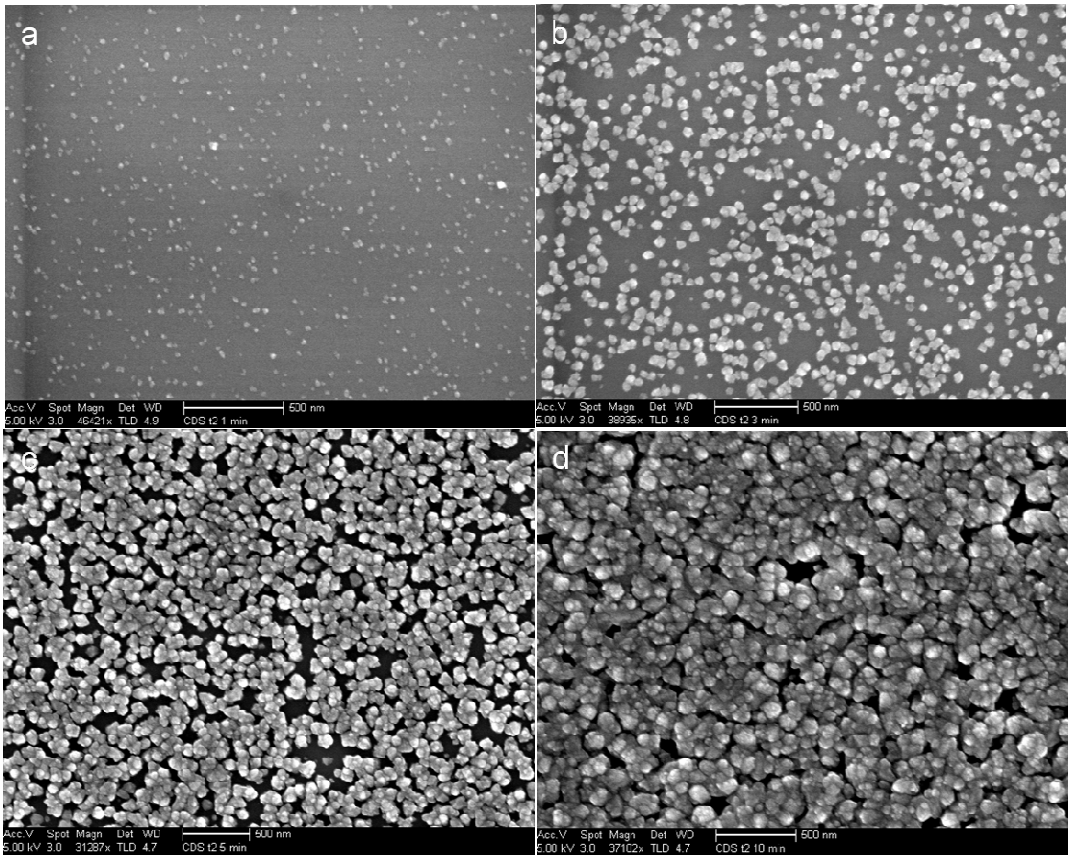

Figure 5.10 SEM micrographs of CdS thin films deposited at mean residence time of 3.5 sec using original recipe for (a) 1, (b) 3, (c) 5, and (d) 10 mins, respectively.

When using a 7-sec residence time, larger crystal sizes were observed compared to the results obtained from a 3.5-sec residence time as shown in Figure 5.11. In this deposition condition, we can see some CdS nanocrystals grown on the substrate surface at a 1-min deposition time as shown in Figure 5.11(a). When increasing the deposition times from 3, 5 to 10 mins as shown in Figure 5.11(b), (c), and (d), respectively, relatively compact and dense films could be obtained.

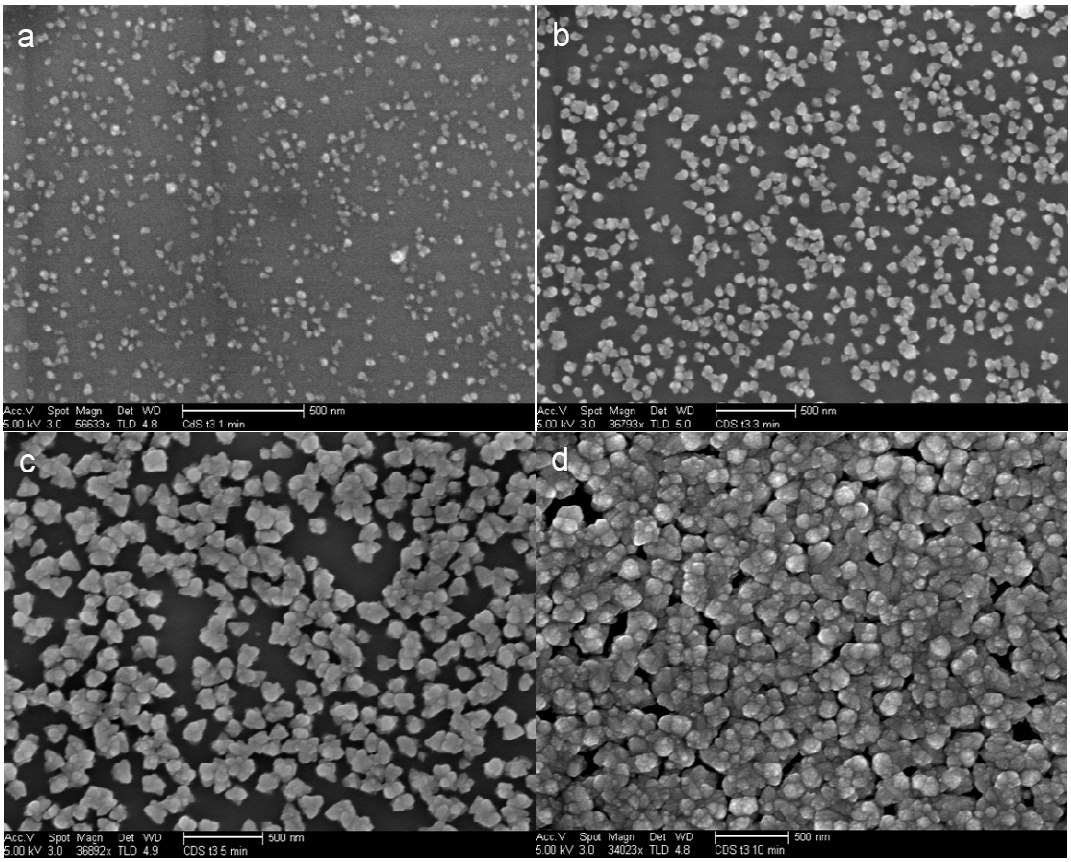

Figure 5.11 SEM micrographs of CdS thin films deposited at a mean residence time of 7 sec using the original recipe for (a) 1, (b) 3, (c) 5, and (d) 10 mins, respectively.

Samples deposited on oxidized silicon substrates at mean residence time of 35 sec for 1, 3, 5 and 10 minutes were also carried out. Figure 5.12(a), (b), (c), and (d) corresponded to 1, 3, 5, and 10 mins deposition times, respectively. Again, larger crystal sizes were observed compared to the results obtained from the 7-sec residence time.

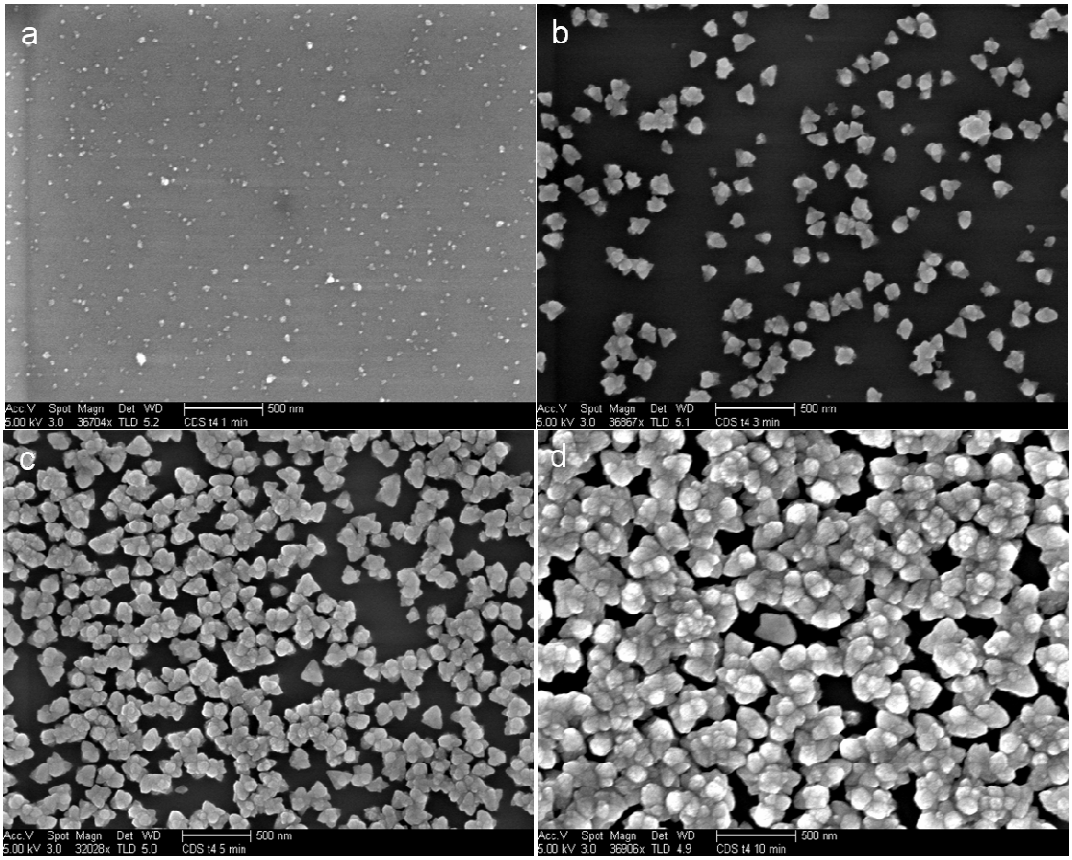

Figure 5.12 SEM micrographs of CdS thin films deposited at a mean residence time of 35 sec using the original recipe for (a) 1, (b) 3, (c) 5, and (d) 10 mins, respectively.

CdS samples prepared at a mean residence time of 70 sec for 1, 3, 5 and 10 mins deposition time were also performed. The corresponding SEM micrographs were shown in Figure 5.13(a), (b), (c), and (d) respectively. Smaller crystal sizes compared to the 35 sec one were observed. This result probably occurred when the residence time was increased to 70 sec, lower thin film growth rate was obtained. The lower growth rate was responsible for smaller crystal sizes resulting in the lower thickness of the thin films.

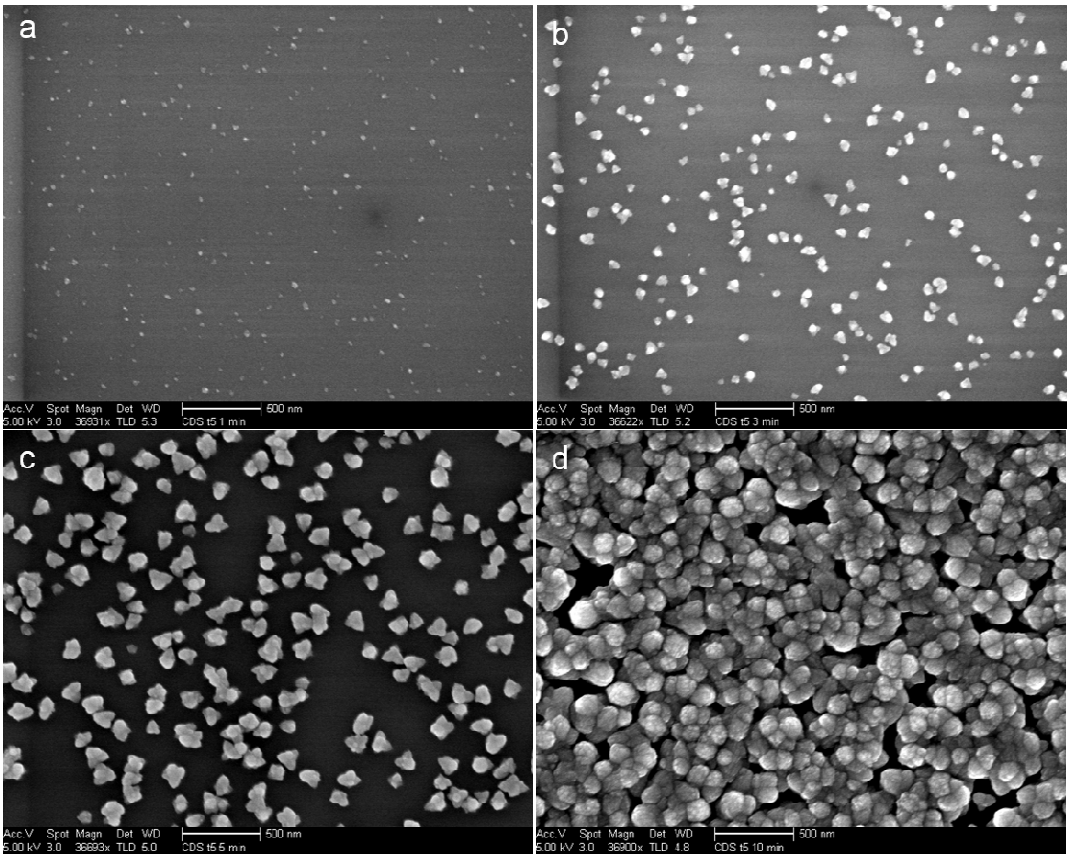

Figure 5.13 SEM micrographs of CdS thin films deposited at a mean residence time of 70 sec using the original recipe for (a) 1, (b) 3, (c) 5, and (d) 10 mins, respectively.

5.3.3 CdS Growth Mechanisms

Previous works from Ortega-Borges and Lincot [27] and Doña and Herrero [44] suggested that thiourea reacts with either cadmium hydroxide [27] or dihydroxo-diammino-cadmium complex [44] to form different adsorbed metastable complexes for batch CBD CdS deposition. Due to the limited control of the mixing of reactant solutions by conventional batch CBD setup, all the precursor solutions have to sequentially be pulled into the reaction beaker and mixed all at once. However, using our reactor, we were able to control the mixing elements and sequences based on the design of experiments and observe the effect that could not be found previously.

To obtain the concentration of HS^-, $SC(NH_2)_2$, OH^-, and S^{2-} just coming out from the PEEK tube after different residence times for an operating temperature at 80 ^oC, Polymath 5.1 was used for solving the ordinary differential equation of equation 5.5 based on the thiourea hydrolysis reaction (equation 2.4).

$$\frac{d(HS^-)}{dt} = k(0.04 - HS^-)(0.001 - HS^-) \qquad [5.5]$$

$$SC(NH_2)_2 + OH^- \rightarrow HS^- + CH_2N_2 + H_2O \qquad [2.4]$$

where k is the rate constant for the thiourea hydrolysis reaction at 80 ^oC, 2.63E-5 (l/mol.sec) [79], 0.04 (M) is the initial thiourea concentration, and 0.001 (M) is the

initial OH^- concentration for pH=11. S^{2-} concentration can be further calculated from equation 2.5, $[S^{2-}] = 10^{-3.3} [HS^-] [OH^-] = 10^{-6.3} [HS^-]$, when an alkaline solution with pH=11 was used [80].

$$HS^- + OH^- \leftrightarrow S^{2-} + H_2O \quad k_e = 10^{-3.3} \qquad [2.5]$$

Table 5.8 shows the concentration of HS^-, $SC(NH_2)_2$, OH^-, and S^{2-} coming out from the PEEK tube after different residence times at 80 ^oC solved by Polymath 5.1 software.

The concentration of HS^-, $SC(NH_2)_2$, OH^-, and S^{2-} versus different residence time are shown in Figure 5.14 (a), (b), (c), and (d), respectively.

Table 5.8 The concentration of HS^-, $SC(NH_2)_2$, OH^-, and S^{2-} coming out from the PEEK tube after different residence times at 80 °C.

Residence time (sec)	1	3.5
HS^- (M)	1.052E-9	3.682E-9
$SC(NH_2)_2$ (M)	3.9999998948E-2	3.9999996318E-2
OH^- (M)	9.99998948E-4	9.99996318E-4
S^{2-} (M)	5.273E-16	1.845E-15
Residence time (sec)	7	35
HS^- (M)	7.364E-9	3.682E-8
$SC(NH_2)_2$ (M)	3.9999992636E-2	3.999996318E-2
OH^- (M)	9.99992636E-4	9.9996318E-4
S^{2-} (M)	3.691E-15	1.845E-14
Residence time (sec)	70	
HS^- (M)	7.364E-8	
$SC(NH_2)_2$ (M)	3.999992636E-2	
OH^- (M)	9.9992636E-4	
S^{2-} (M)	3.691E-14	

(a)

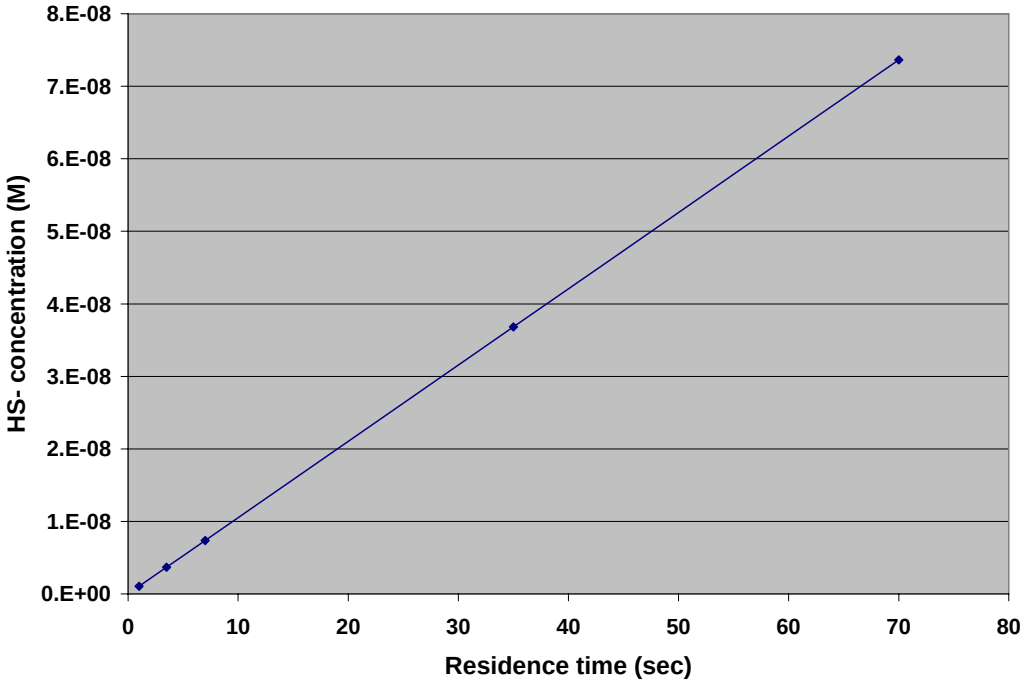
8.E-08
7.E-08
6.E-08
5.E-08
4.E-08
3.E-08
2.E-08
1.E-08
0.E+00
HS- concentration (M)
0
10
20
30
40
50
60
70
80
Residence time (sec)

(b)

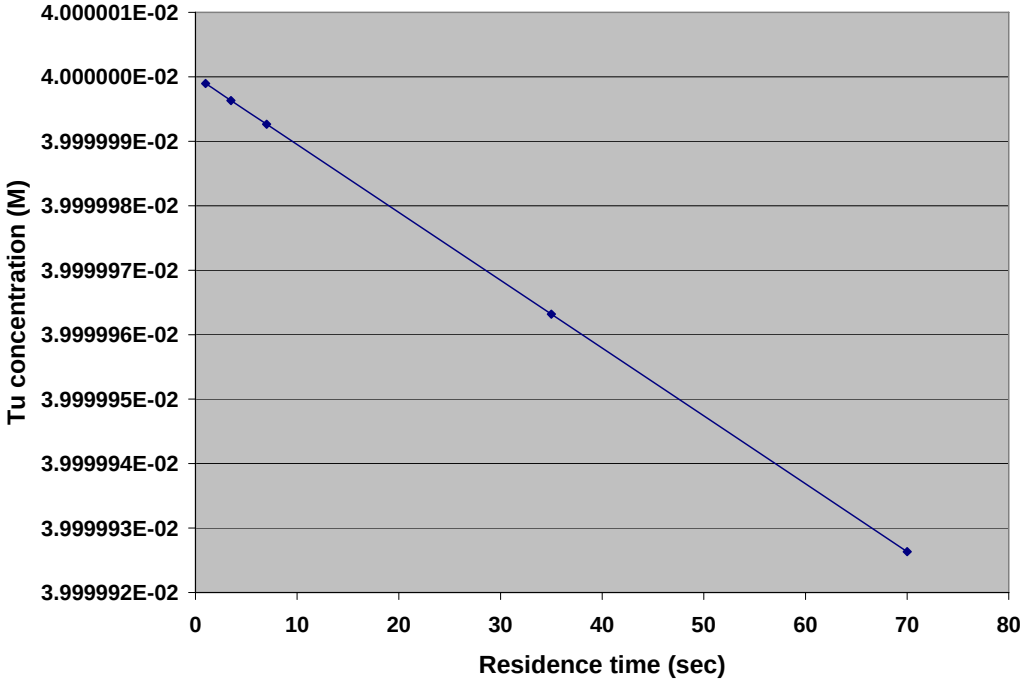
4.000001E-02
4.000000E-02
3.999999E-02
3.999998E-02
3.999997E-02
3.999996E-02
3.999995E-02
3.999994E-02
3.999993E-02
3.999992E-02
Tu concentration (M)
0
10
20
30
40
50
60
70
80
Residence time (sec)

(c)

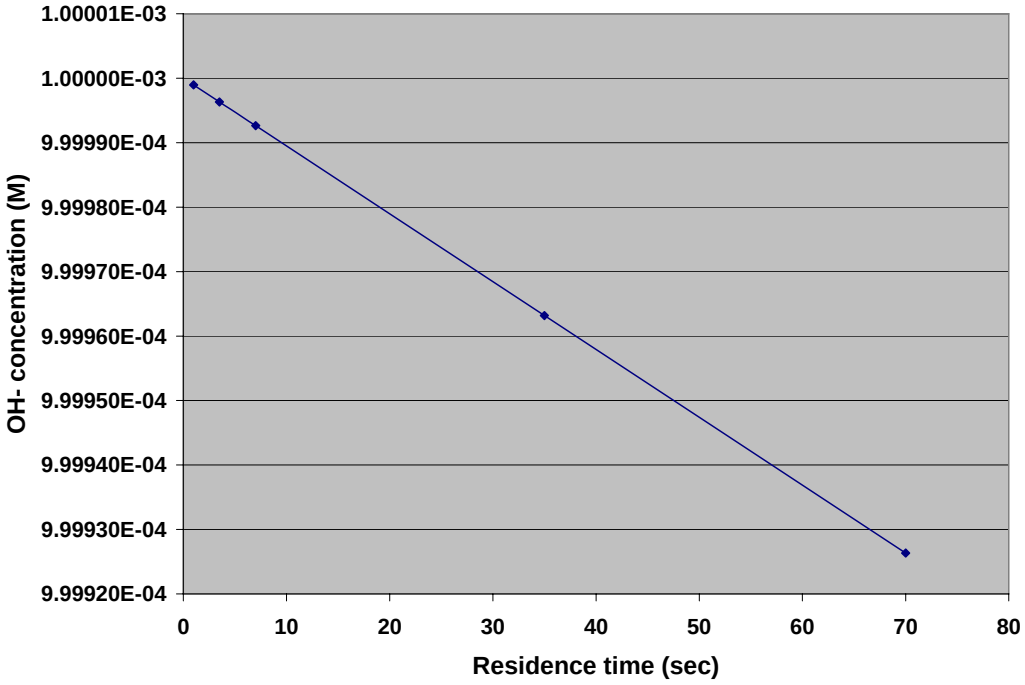
1.00001E-03
1.00000E-03
9.99990E-04
9.99980E-04
9.99970E-04
9.99960E-04
9.99950E-04
9.99940E-04
9.99930E-04
9.99920E-04
OH- concentration (M)
0
10
20
30
40
50
60
70
80
Residence time (sec)

(d)

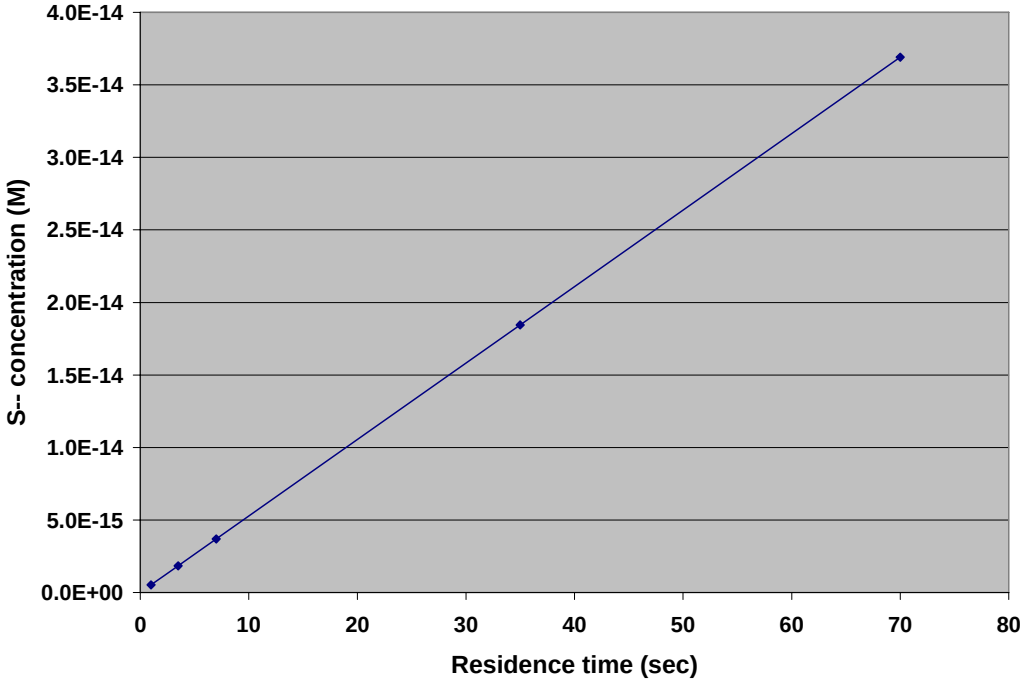
4.0E-14
3.5E-14
3.0E-14
2.5E-14
2.0E-14
1.5E-14
1.0E-14
5.0E-15
0.0E+00
S-- concentration (M)
0
10
20
30
40
50
60
70
80
Residence time (sec)

Figure 5.14 The concentration of (a) HS^-, (b) $SC(NH_2)_2$, (c) OH^-, and (d) S^{2-} versus different residence time at 80 ^oC.

The previous SEM results for a residence time of 1 sec (Figure 5.4) and the concentration data plotted in Figure 5.14 lead us to re-think why there is no clear CdS thin film deposition and only very low growth rate obtained at the very beginning of the reaction even when reactant thiourea concentration is still high compared to the other longer residence time reactions? Could it be possible that the dominant sulfide ion source that is responsible for CdS thin film deposition may not be thiourea itself but actually others? One possible explanation is that at the very short residence time of 1 sec, the concentration of HS^- formed through the thiourea hydrolysis reaction (equation 2.4) is very low resulting in a very low growth rate of CdS thin film deposition.

There are two possible sulfide ion sources, HS^- and S^{2-}, other than thiourea based on equation 2.4 and 2.5 that could be used for the CdS thin film deposition. To figure out which one is responsible for the CdS thin film deposition using our continuous flow microreactor setup and further support the hypothesis, two experiments were performed.

First, the new precursor solutions for stream A and B, different from the original ones, were prepared. We had intentionally pre-mixed $SC(NH_2)_2$ and NH_4OH together in stream B and had only $CdCl_2$ and NH_4Cl in the stream A. The HS^- ions formed through the thiourea hydrolysis reaction in stream B at room

temperature were expected. In the stream B, most of the sulfide ions were in the form of HS^- rather than S^{2-}, $[S^{2-}] = 10^{-3.3}\,[HS^-][OH^-] = 10^{-6.3}\,[HS^-]$ from equation 2.5, when an alkaline solution with pH=11 was used [80]. Therefore, the main sulfide ions in the solution will be HS^- that dominant the CdS deposition and it is possible to obtain only extremely small S^{2-} concentrations by having a very large excess of OH^- in the solution.

The SEM micrographs of CdS thin films deposited at a 1-sec residence time using $SC(NH_2)_2$ and NH_4OH system in stream B for deposition time of (a) 1, (b) 3, (c) 5, and (d) 10 mins, respectively are shown in Figure 5.15. We have clearly seen that relatively smooth thin films with few crystals were observed in Figure 5.15(a). Lots of nanocrystals were grown and distributed on the surface for longer deposition times with increased crystal size and surface coverage. These results, surface morphology, however, were not observed previously for short deposition times using the original recipe (Figure 5.4(a), (b), and (c)) but rather close to the 10-min one (Figure 5.4(d)).

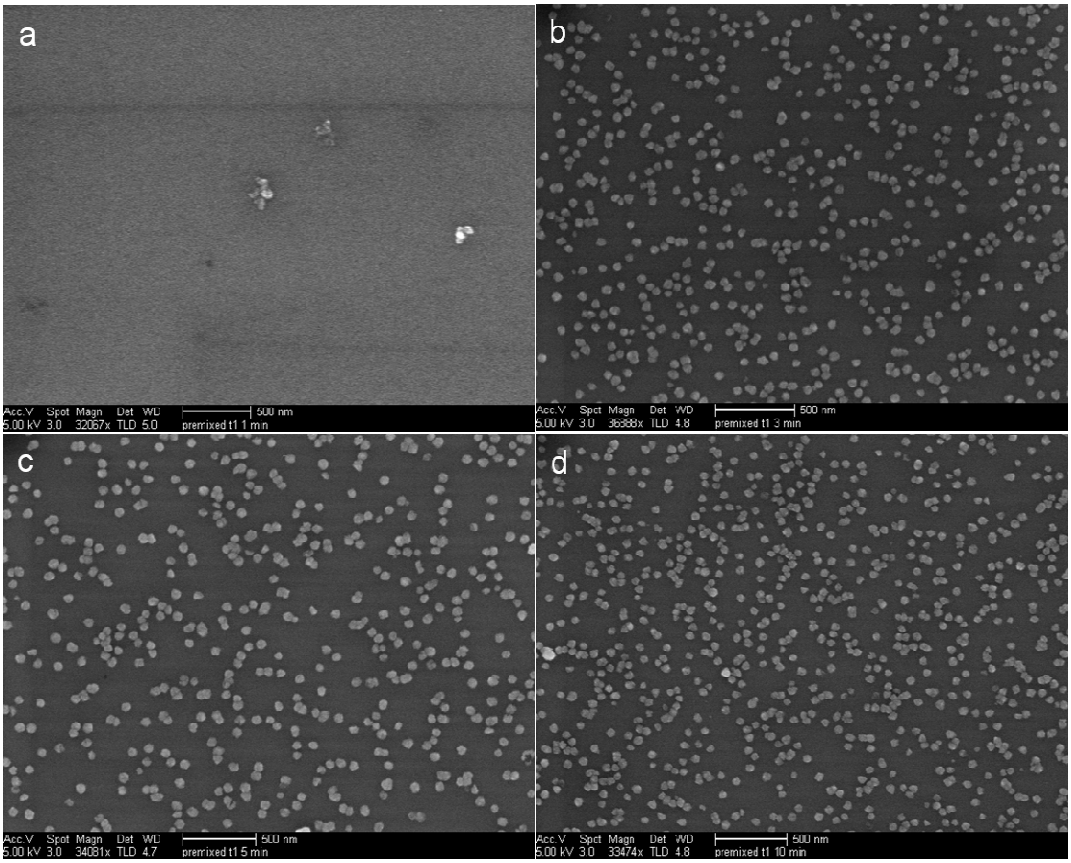

Figure 5.15 SEM micrographs of CdS thin films deposited at a mean residence time of 1 sec using $SC(NH_2)_2$ and NH_4OH system in the stream B for (a) 1, (b) 3, (c) 5, and (d) 10 mins, respectively.

Table 5.9 shows the average CdS thin film thickness deposited by different deposition times for a mean residence time of 1 sec using the pre-mixed and original recipes.

Table 5.9 Average CdS thin film thicknesses deposited by different deposition times for a mean residence time of 1 sec using the pre-mixed and original recipes.

	Average CdS thin film thicknesses (Å) for residence time of 1 sec	
Deposition time (min)	Pre-mixed	Original
1	150	90
3	600	200
5	900	350
10	1950	800

The thickness data from Table 5.9 was further plotted in Figure 5.16 showing the deposited CdS thin film thickness versus the deposition time at a 1-sec residence time. The fitted linear regression lines were also plotted to obtain the individual growth rate values for different recipes and are shown in Table 5.10.

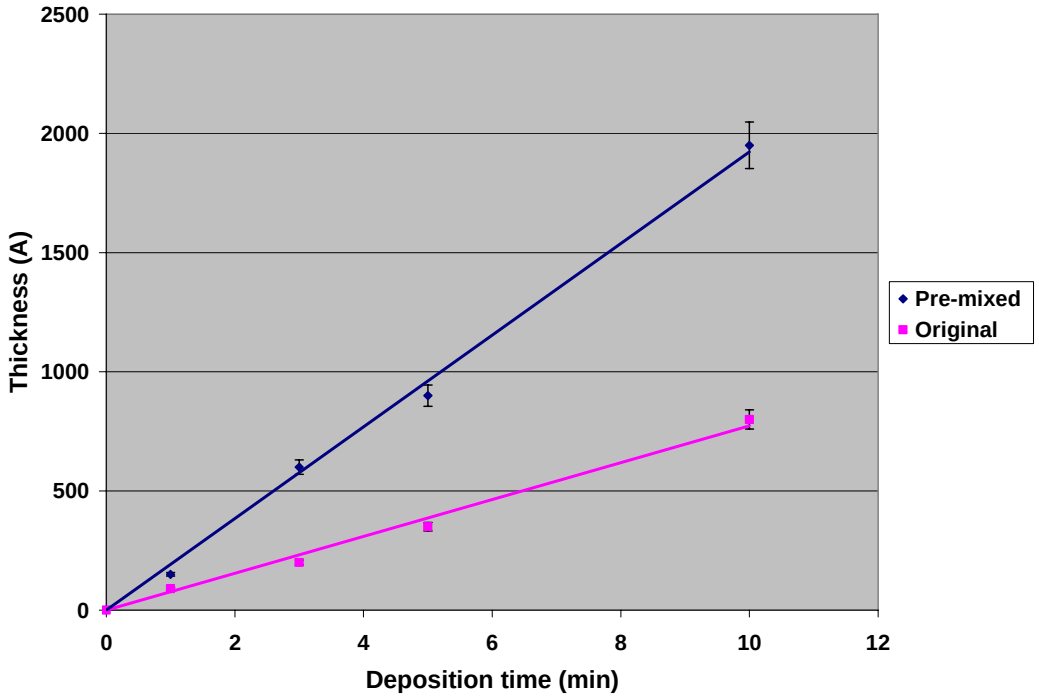

Figure 5.16 Comparison of CdS thin film thickness versus deposition time for a mean residence time of 1 sec using the pre-mixed and original recipes.

Table 5.10 CdS thin film growth rates obtained from a 1-sec residence time for the pre-mixed and original recipes.

Experimental conditions	Pre-mixed	Original
Growth rate (Å/min)	192.22	77.33

From Table 5.10 and Figure 5.16, the growth rate results clearly indicate that the deposited thin films using the pre-mixed $SC(NH_2)_2$ and NH_4OH system had a growth rate about 2.5 times higher than the one using the original recipe.

This result indicated that a higher HS^- concentration was formed by the pre-mixed treatment through the thiourea hydrolysis reaction resulting in a higher growth rate of CdS thin film deposition.

Second, the $CdCl_2$ and Na_2S system that often used to generate CdS nanoparticles through the reaction of free sulfide ions, S^{2-}, and free cadmium ions, Cd^{2+}, in solution using the short residence time of 1 sec was used for the CdS thin film deposition. In stream A and B, 50 ml of 0.004 M $CdCl_2$ and 50 ml of 0.004 M $Na_2S.9H_2O$ were used for Cd^{2+} and S^{2-} sources, respectively. After the deposition, the pieces of crack-shaped CdS crystallines and a bunch of CdS particles aggregated together and were observed from SEM micrographs for 1 and 10 mins deposition times as shown in Figure 5.17(a) and (b), respectively. This non-uniform thin film morphology is often found for the deposition through homogeneous particle formation and aggregation. On the other hand, when CdS thin film deposited through the heterogeneous surface reaction with HS^- ions formed through the thiourea hydrolysis reaction, smooth surface morphology can be obtained. Therefore, based on the SEM results, the S^{2-} will not be the one responsible for the CdS thin film deposition using our reactor setup and can be ruled out from the list of potential sulfide ion sources.

(a)

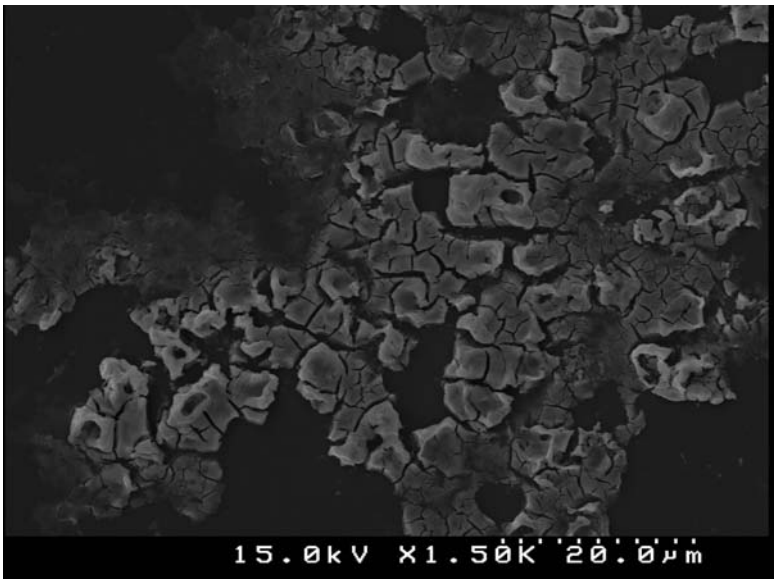

(b)

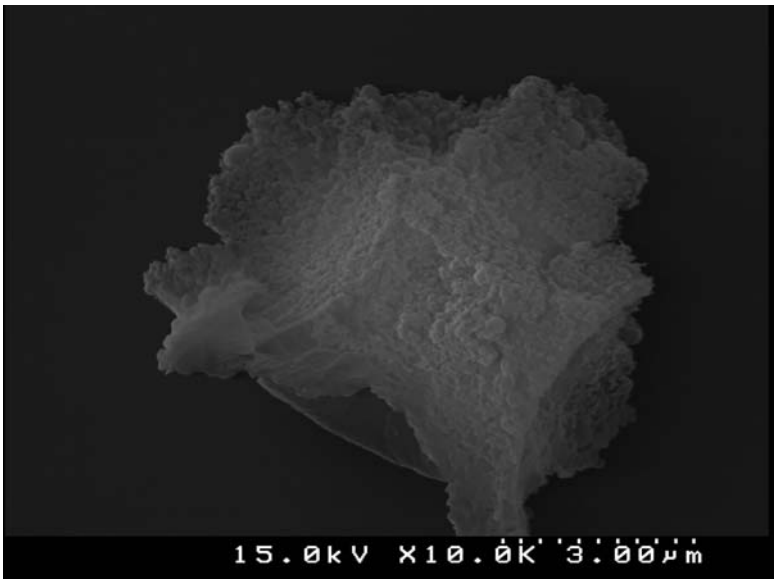

Figure 5.17 SEM micrographs of CdS thin films deposited at a mean residence time of 1 sec using $CdCl_2$ and Na_2S system for (a) 1 and (b) 10 mins, respectively.

Based on previous experimental results, the HS^- ions formed through the thiourea hydrolysis reaction are the dominant sulfide ion source responsible for the CdS deposition rather than the thioura itself that had widely been discussed in almost all the previous literature [4,5,27,44,80]. These results lead to the term of thiourea concentration in the rate equation of CdS thin film growth need to be replaced by HS^- concentration. This finding could not be found previously by a conventional CBD batch setup because all the reactant solutions were sequentially pulled into the reaction beaker and mixed all at once. However, using our reactor, we were able to control the mixing elements and sequence based on design of experiments which cannot be achieved by batch CBD process.

Based on thin film deposition results and our current understanding, the CdS thin film growth mechanism using the continuous flow microreactor was proposed. A schematic diagram that illustrates the growth mechanism is given in Figure 5.18.

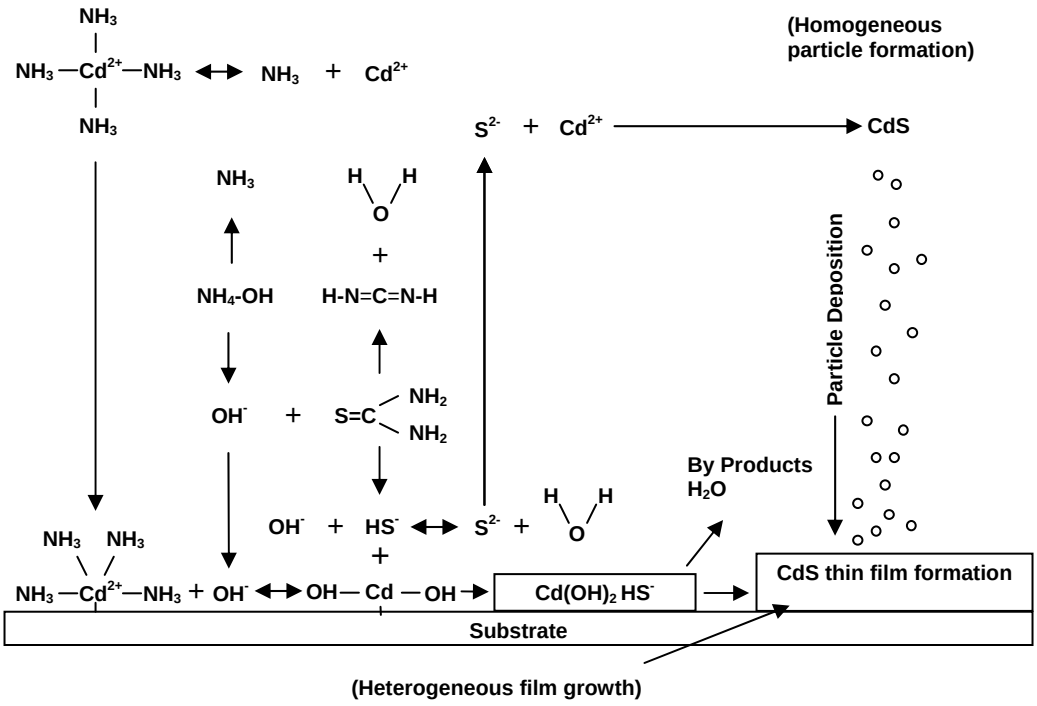

Figure 5.18 Schematic diagram of the CdS growth mechanism using the continuous flow microreactor.

There are two major reactions in the CdS growth process using the continuous flow microreactor: homogeneous particle formation and heterogeneous surface reaction. For the homogeneous reaction, the cadmium salt, such as $CdCl_2$, produces free cadmium ions, Cd^{2+}, through a dissociation reaction.

$$CdCl_2 \rightarrow Cd^{2+} + 2Cl^- \qquad [5.6]$$

An alkaline solution consisting of ammonium hydroxide provides ammonia in the solution.

$$NH_4^+ + OH^- \leftrightarrow NH_3 + H_2O \quad [5.7]$$

The cadmium ions then complex with ammonia to form the dominant tetra-amino-cadmium complex ions, $Cd(NH_3)_4^{2+}$, controlling the concentration of free cadmium ions.

$$Cd^{2+} + 4NH_3 \leftrightarrow Cd(NH_3)_4^{2+} \quad [5.8]$$

The HS^- ions formed through the thiourea hydrolysis reaction are the dominant sulfide ions responsible for CdS thin film deposition. Free sulfide ions, S^{2-}, then formed through an equilibrium hydrolysis reaction.

$$SC(NH_2)_2 + OH^- \rightarrow HS^- + CH_2N_2 + H_2O \quad [5.9]$$

$$HS^- + OH^- \leftrightarrow S^{2-} + H_2O \quad [5.10]$$

Free cadmium ions then reacted with free sulfide ions to form CdS particles in the bulk solution.

$$Cd^{2+} + S^{2-} \rightarrow CdS_{(s)} \quad [5.11]$$

For the heterogeneous reaction on the surface, first the adsorbed tetra-amino-cadmium complex ions reacted with hydroxide ions to form the adsorbed cadmium hydroxide, $\left[Cd(OH)_2\right]_{ads}$, on the surface.

$$Cd(NH_3)_4^{2+} + 2OH^- + site \xleftrightarrow{k_1, k_{-1}} \left[Cd(OH)_2\right]_{ads} + 4NH_3 \qquad [5.12]$$

Finally, CdS was formed through a Rideal-Eley growth mechanism of the adsorbed cadmium hydroxide reacts with HS^- and the site regeneration.

$$\left[Cd(OH)_2\right]_{ads} + HS^- \xrightarrow{k_2} CdS + H_2O + OH^- + site \qquad [5.13]$$

Based on equation 5.12 and 5.13, the global reaction for CdS deposition using continuous flow microreactor can be presented as:

$$Cd(NH_3)_4^{2+} + HS^- + OH^- \rightarrow CdS + 4NH_3 + H_2O \qquad [5.14]$$

This newly proposed growth mechanism is compared with the global reaction (equation 2.7) for CBD CdS deposition proposed by Ortega-Borges *et al*. [27]. The major difference is that $SC(NH_2)_2$ was replaced by HS^- for the dominant sulfide ion source that was responsible for the CdS deposition.

5.3.4 The Rate Equation

Our deposition results suggest that the term of thiourea concentration in the rate equation of CdS thin film growth needs to be replaced by HS^- concentration. From previous proposed CdS growth mechanisms using a continuous flow microreactor, the equation 5.13 is considered as the rate-limiting step in the mechanism. Based on this equation, the theoretical growth rate equation for the mechanism can be derived.

The CdS growth rate is given by

$$r = k_2 C_s \theta_1 [HS^-] \qquad [5.15]$$

where

C_s = Surface site concentration

θ_1 = Substrate surface fraction covered by $[Cd(OH)_2]_{ads}$

If we applied the stationary-state theory to the intermediate specie in the mechanism proposed, we can have

$$\frac{d[Cd(OH)_2]}{dt} = k_1 [Cd(NH_3)_4{}^{2+}] \; [OH]^2 C_s (1-\theta_1) - k_1 [NH_3]^4 C_s \theta_1 - k_2 [HS^-] \; C_s \theta_1 = 0 \qquad [5.16]$$

Thus

$$\theta_1 = \frac{k_1\left[Cd(NH_3)_4{}^{2+}\right]\left[OH^-\right]^2}{k_1\left[NH_3\right]^4 + k_1\left[Cd(NH_3)_4{}^{2+}\right]\left[OH^-\right]^2 + k_2\left[HS^-\right]} \qquad [5.17]$$

By substituting the equation 5.17 into 5.15, the theoretical growth rate equation for the proposed CdS growth mechanisms using a continuous flow microreactor could be written as follows.

$$r = \frac{k_1 k_2 C_s\left[Cd(NH_3)_4{}^{2+}\right]\left[OH^-\right]^2\left[HS^-\right]}{k_1\left[NH_3\right]^4 + k_1\left[Cd(NH_3)_4{}^{2+}\right]\left[OH^-\right]^2 + k_2\left[HS^-\right]} \qquad [5.18]$$

5.3.5 Activation Energy

In order to better understand the growth mechanism of the deposited CdS thin films, the values of activation energy for different impinging fluxes were obtained. The activation energy, E_a, of a reaction is the amount of energy needed to start the reaction. It represents the minimum energy needed to form an activated complex during a collision between reactants in order for a chemical reaction to occur. For a given reaction, the rate constant, k, is strongly related to the temperature of the system that is known as the Arrhenius equation:

$$k(T) = k_o * \exp\text{^-}(E_a/RT) \quad [5.19]$$

where k_o is a constant called the frequency factor, R is the ideal gas constant and T is the absolute temperature.

The thin film growth rate at a given condition can be considered independent of the reacting species concentration evolution during the deposition process. The growth rate variation with temperature can only be due to the rate constant dependence on the temperature. Therefore, this dependence can be expressed by the following equation:

$$r(T) = A' * \exp\text{^-} (E_a/RT) \quad [5.20]$$

where r(T) is the growth rate as a function of temperature and A' is the pre-exponential factor which includes the frequency factor, k_o, and a constant related with the initial reagent concentration.

The temperature dependence of the CdS thin film growth rate was studied in the range from 60 to 80 ^oC in steps of 5 ^oC for residence time of 1, 3.5, 7, 35, and 70 sec.

From Table 5.3, Figure 5.7 and Table 5.4 using a 1-sec residence time, we can observe that the thin film growth rate increases slowly when the operating

temperature is increased. Figure 5.19 presents the Neperian logarithm of the growth rate as a function of 1000/T (k) from Table 5.4. The activation energy for this deposition condition can be calculated from the negative slope of the linear fit of the Neperian logarithm of the growth rate as a function of 1000/T. In this case, the activation energy of 43.85 KJ/mol was obtained.

The detail experimental data for obtaining the activation energy for other impinging fluxes (except for 1 sec residence time) are shown in Appendix A1 to A4 for residence times of 3.5, 7, 35, and 70 sec, respectively.

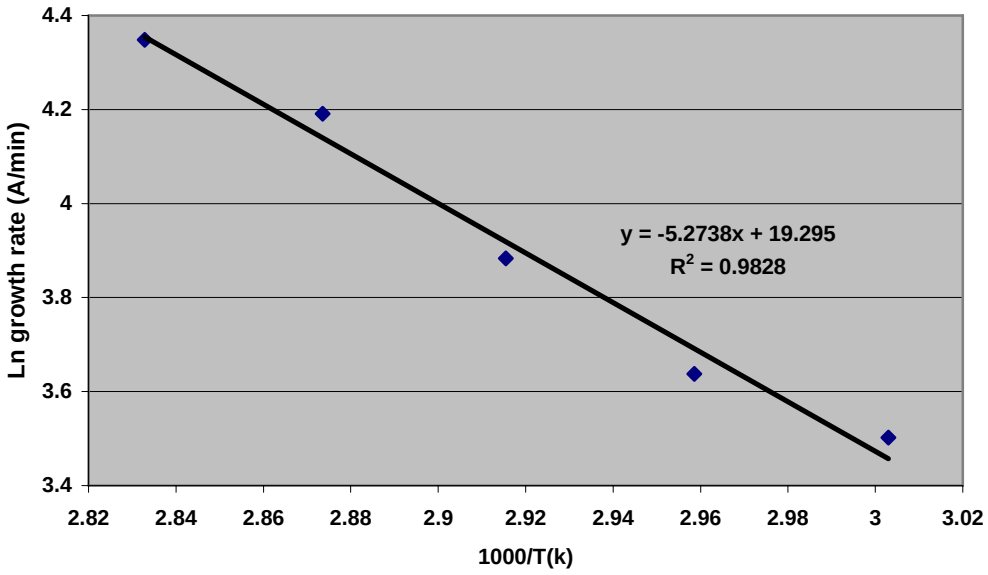

Figure 5.19 Neperian logarithm of the growth rate as a function of 1000/T (k) obtained from a 1-sec residence time at different operating temperatures.

The activation energies obtained from different impinging fluxes using the continuous flow microreactor are listed in Table 5.11 for comparison.

Table 5.11 Comparison of activation energies obtained from different residence times.

Residence time (sec)	1	3.5	7	35	70
Activation engergy (KJ/mol)	43.85	60.27	62.12	62.75	64.22

From Table 5.11, when a 1-sec residence time was used, the relatively low activation energy was obtained (~44 KJ/mol). When increasing the residence time from 3.5 to 70 sec, the activation energy first increased to 60.27 KJ/mol and then slowly increased to 64.22 KJ/mol. The relatively low value of activation energy obtained from the 1-sec residence time could be contributed to the heterogeneous surface reaction of the rate limiting step for CdS thin film formation (equation 5.13) based on our newly proposed growth mechanism when very low HS^- concentration was formed at this processing condition. When increasing the residence time from 3.5 to 70 sec, the values of the activation energy increased from ~60 to 64 KJ/mol. At these reaction conditions, the higher HS^- concentration was formed; therefore, the higher activation energy could be responsible for the combination of thiourea hydrolysis reaction (equation 5.9) and the reaction of the rate limiting step for CdS thin film formation (equation 5.13). The activation energy value of ~75 KJ/mol for thiourea hydrolysis reaction was reported previously [79]. The higher activation energy value of 85 KJ/mol for batch CBD CdS deposition was reported earlier [27,44]. This result could be

contributed to both the thiourea hydrolysis reaction and the heterogeneous surface reaction based on their proposed mechanisms that performed during the CBD CdS deposition process.

CHAPTER 6

ALTERNATIVE MATERIAL AND PROCESS

6.1 Background

Many compound semiconductors (II-VI, IV-VI, V-VI, I-III-VI) have been deposited by CBD techniques, such as Ag_2S, CdS, CdSe, CoS, Cu_2S, Cu_2Se, PbS, SnS, SnO, MoS_2, SbS, TiO_2, ZnO, ZnS, ZnSe, CdZnS, $CuInS_2$, $CuInSe_2$, PbHgS, etc. Among these, CBD CdS deposition is the most studied CBD process due to its important role in fabricating CdTe and $CuInSe_2$ thin film solar cells. For this reason and our laboratory's previous experience with this process, the CBD CdS process was used in fabricating thin film transistors and in investigating the fundamental reaction kinetics and growth mechanism of CBD. Furthermore, the fundamental knowledge learned from the CBD CdS process would provide a model for other CBD processes. Due to environmental safety issues regarding manufacturing and waste treatment, other cadmium free material, indium oxide**,** deposited by solution-based deposition process was carried out for exploring the feasibility of fabricating flexible electronics.

6.2 Indium Oxide Thin Film Formation

Transparent conducting oxides (TCOs) such as zinc oxide, tin oxide, and indium oxide are significant for their optical and electrical applications used in the

microelectronic industry such as flat-panel displays, organic light-emitting diodes, electrochromatic windows, electromagnetic shielding and active channel materials for thin film transistors [81,82]. Recently fabricated ZnO thin film transistors (TFTs) with a channel layer prepared by rf magnetron sputtering deposition [54,83], pulsed laser deposition (PLD) [84] and solution-based deposition processes such as chemical nanoparticle deposition [11] and spin-coating [85,86] and the SnO_2 transparent thin film transistors (TTFTs) with a channel layer deposited by rf magnetron sputtering [87] have been widely investigated and were used in the field of transparent electronics [88]. More important, the use of transparent conducting multicomponent oxide materials provides the possibility to tailor the electrical, optical, physical and chemical properties of TCO films by altering the chemical compositions [89-91]. Using transparent indium oxide as active channel materials for fabricating thin film transistors had just reported very recently [92], and most of the works were mainly focused on zinc and indium oxide-based electronic devices [93] such as zinc tin oxide (ZTO) [94] and zinc indium oxide (ZIO) systems [95,96].

A newly developed precursor solution was used to deposit highly transparent amorphous indium oxide (In_2O_3) thin films through a solution-based deposition process at a low-temperature of ~70 ^oC. Depletion-mode In_2O_3 metal–insulator-semiconductor field-effect transistors (MISFETs) with the field-effect mobility (μ_{FE}) as high as 18.71 and 2.23 cm^2/V s were obtained for devices with

and without postannealing processes performed in the air for 1 hour at 300 ^{o}C, respectively. These results demonstrated a promising pathway that is suitable for fabricating transparent flexible electronics on polyethylene terephthalate (PET) or polyimide (Kapton) polymeric substrates using solution-processed indium oxide (In_2O_3) thin films as the active channel layers.

6.2.1 Experimental Setup

Due to the indium oxide precursor solution which was prepared and well mixed before pumping into the reactor, a simpler version of the microreactor (Figure 6.1) can be operated compared to previously using the continuous flow microreactor for depositing nanocrystalline CdS semiconductor thin films. The simplified micropump deposition system setup consists of a microprocessor controlled peristaltic pump (Ismatec REGLO Digital), a 1.22 mm ID Tygon ST tubing (Upchurch Sscientific), a 3 in. diameter stainless steel metallic plate, and a 2 in. diameter x 0.75 in. thick heating hotplate with a digital temperature controller (Watlow).

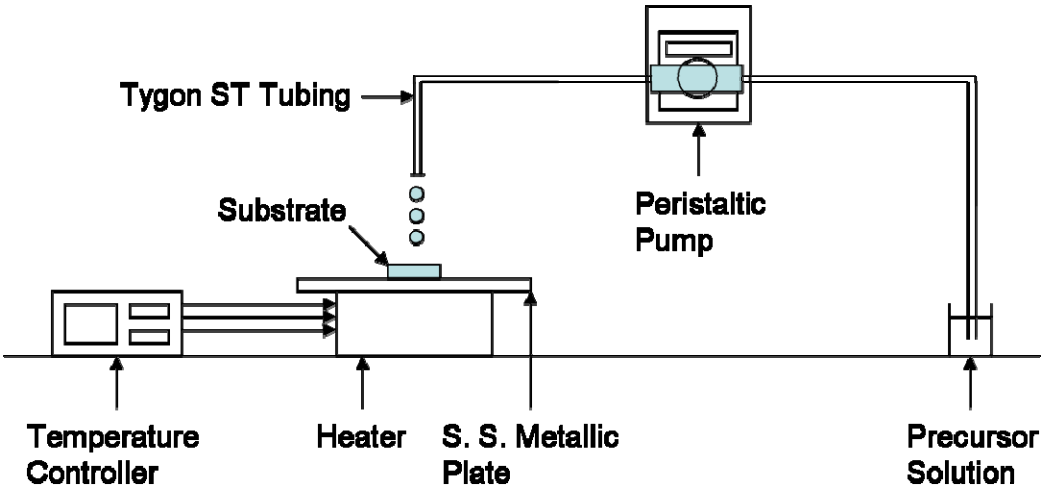

Figure 6.1 Schematic diagram of micropump deposition setup for indium oxide (In_2O_3) thin film deposition.

A newly developed metal halide precursor solution for fabricating In_2O_3 thin films was prepared by dissolving 0.03 M of $InCl_3$ in 25 ml acetonitrile solvent and well mixed by ultrasonicating the solution in a 30 ml pre-cleaned vial for 10 mins at an ambient temperature. Oxidized silicon substrates (silicon wafer coupons) measuring 15 X 10 mm were used for depositing In_2O_3 thin films. Those substrates were initially sonicated in an untrasonic bath using a 1 M NaOH solution for about 5 min providing a hydrophilic surface suitable for the deposition process. Finally, they were rinsed with DI water and dried under a stream of nitrogen gas before being used for deposition. The substrate was taped to a 3 in. diameter stainless steel metallic plate and heated on a metal hotplate at a temperature range of 70-80 ^oC for 3 min before deposition. The precursor solution

was then pumped into the Tygon tube at a flow rate of ~2.4 ml/min and impinged on top of the pre-heated substrate for 2.5 mins. Once the process was completed, the substrate was removed from the metallic plate without further rinsing it with DI water.

6.2.2 Experimental Results

In order to elucidate the formation mechanism of In_2O_3 thin film, thermo gravimetric analysis (TGA) was performed. The thermal behaviors of the In_2O_3 precursor chemicals were investigated by thermo gravimetric analyzer (TA Instrument Inc., Modulated TGA 2950 Thermogavimetric Analyzer). A drop of In_2O_3 precursor solution was first laid on a pre-tarred aluminum pan and dried in the air. TGA analysis was performed at a temperature ramp rate of 5 °C/min from room temperature to 600 °C. The resulted TGA curve is shown in Figure 6.2. Metal halides are known to be moisture sensitive. The as-deposited indium chloride precursor thin films first absorb moisture and form indium hydroxide at room temperature. There are two major features shown in the TGA curve. The first weight loss appeared between room temperature and 80 °C represents the residual solvent (i.e. acetonitrile) evaporation. The second weight loss between 100 °C and 135 °C could be mainly attributed to the loss of water through the dehydration reaction of indium hydroxide and then formed indium oxide or $(1-x)In_2O_3.xInCl_3$, where $0<x<1$. The film continued to lose weight slowly up to 500 °C which was

attributed to the further conversion to indium oxide. The reaction proceeded to completion for temperatures above 500 °C.

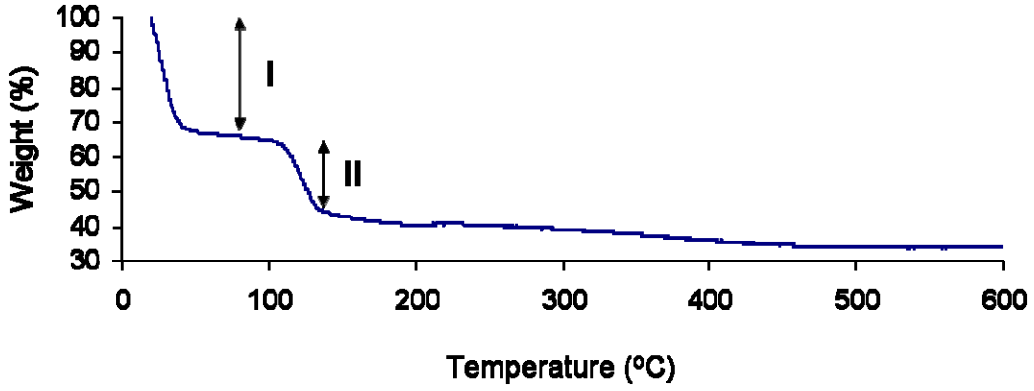

Figure 6.2 Thermo gravimetric analysis (TGA) of an In_2O_3 precursor solution.

The thin films deposited on the transmission electron microscopy (TEM) grids (Electron Microscopy Sciences, Dura SiN TEM grid) were characterized by TEM, electron diffraction (ED) and energy dispersive X-ray (EDX) (FEI Tecnai F20) at 200 KV for high resolution images, structure and chemical composition analysis, respectively. Figure 6.3 shows the TEM/ED/EDX analysis of In_2O_3 thin films deposited on SiN TEM grid substrates for (a) as-deposited and (b) after postannealing for 1 hour at 300 ^oC. More uniform thin films were observed from the as-deposited In_2O_3 thin films comparing to the annealed one. The electron diffraction (ED) analysis showed that both as-deposited and annealed thin films are amorphous structures; also, no crystalline fringes were observed from the higher magnification TEM images. The energy dispersive X-ray (EDX) showed

that both bulk surface films contain In and O with certain amounts of Cl. The results confirmed the formation of In_2O_3 chemistry and showed that our deposited thin films might be in the form of $(1-x)In_2O_3.x\ InCl_3$ where $0<x<1$ and a more detail investigation needs to be carried out. The Si and N were obtained from the SiN TEM grid used as the substrates.

(a)

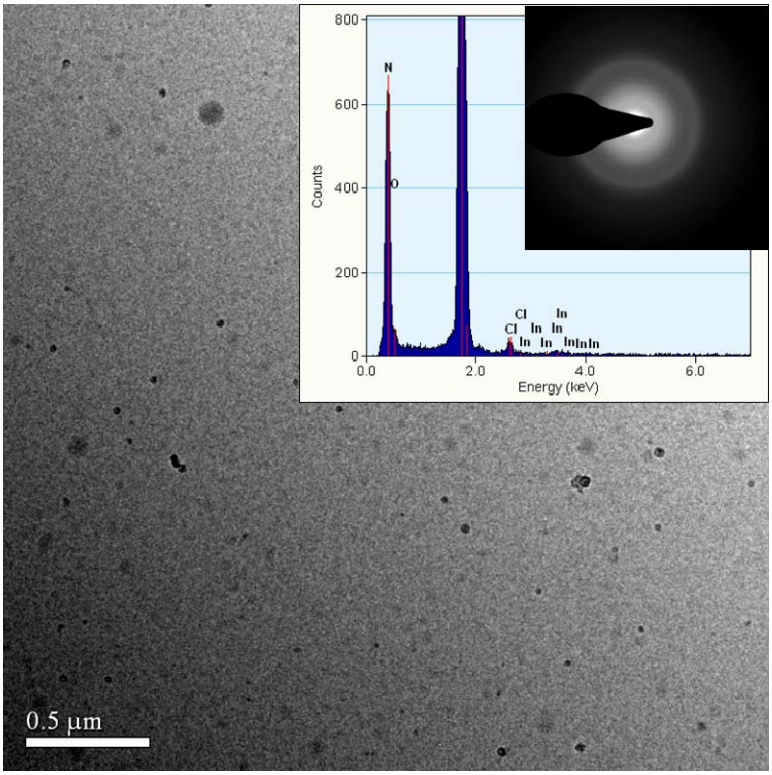

(b)

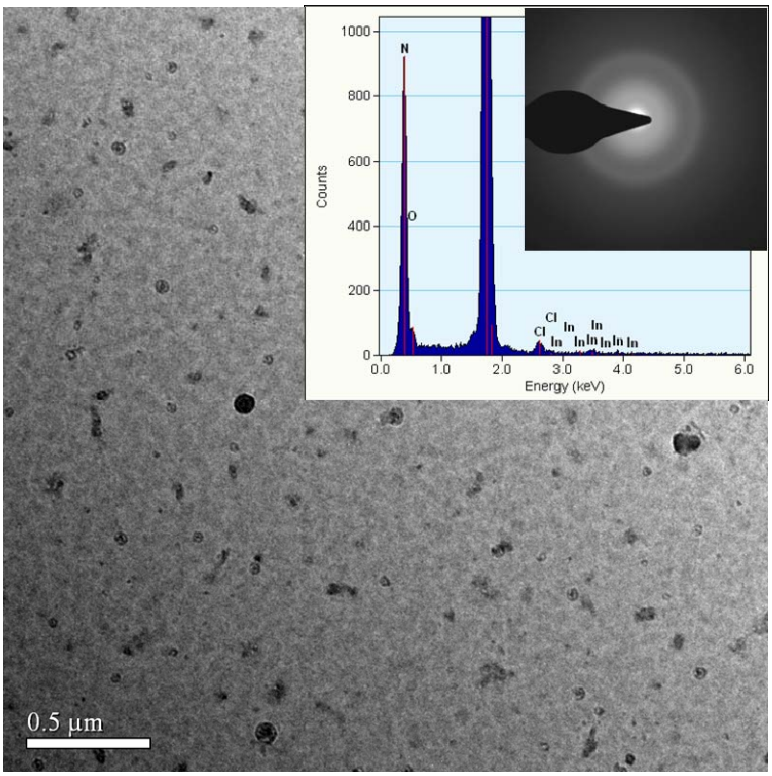

Figure 6.3 TEM/ED/EDX analysis of In_2O_3 thin films deposited on SiN TEM grid substrates for (a) as-deposited and (b) after postannealing for 1 hour at 300 ^oC.

The transmission analysis of the In_2O_3 thin films was measured at various wavelengths by a UV-Vis spectrophotometer (Ocean Optics Inc, USB 2000 optic spectrometer) for transmittance measurement. Optical transmittance of In_2O_3 thin films deposited on quartz substrates (G. M. Associate, Inc.) were measured in the wavelength range from 250 to 700 nm. The results showed that the In_2O_3 thin films were highly transparent with ~90 and 95 % in the visible portion (400 to 700 nm)

of the electromagnetic spectrum for as-deposited and annealed thin films shown in Figure 6.4(a) and (b), respectively. Optical image (inset) of thin film is also shown.

(a)

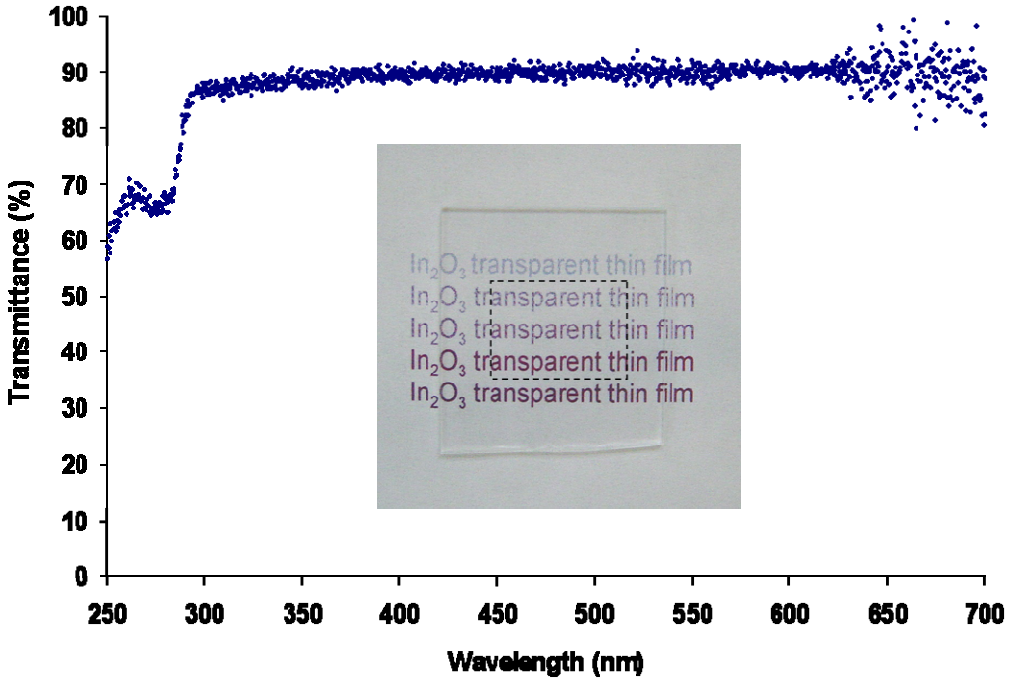

(b)

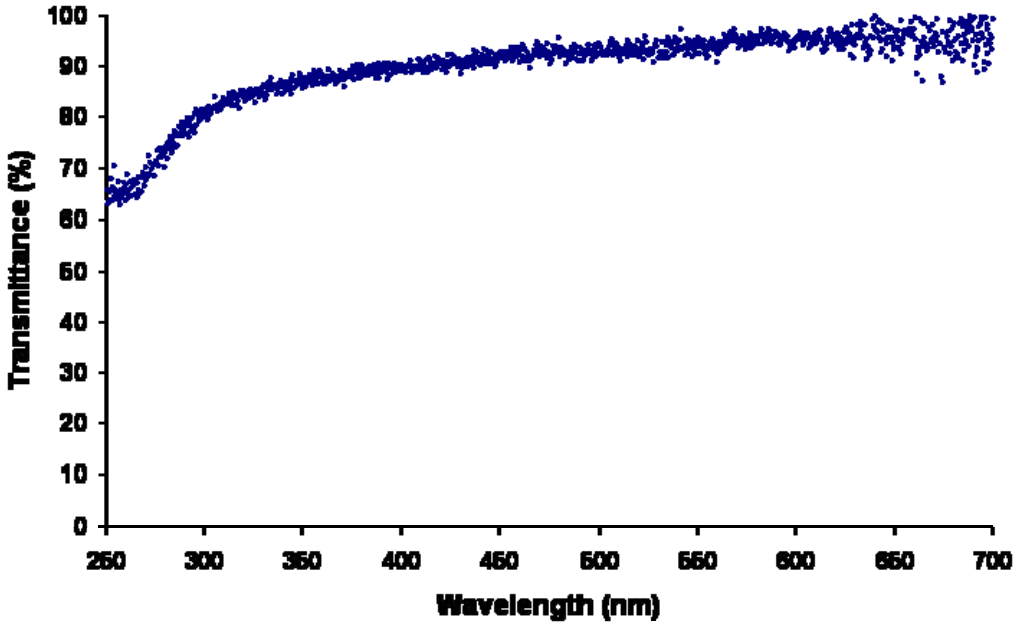

Figure 6.4 Optical transmittance of In_2O_3 thin films deposited on quartz substrates for (a) as-deposited and optical image (inset) of thin film and (b) after postannealing for 1 hour at 300 ^oC.

The surface morphology of the deposited thin films were characterized by a scanning electron microscopy (SEM) (FEI Sirion XL30) at 5 KV. SEM images of as-deposited and annealed In_2O_3 thin films taken from the device gate areas were shown in Figure 6.5(a) and (b), respectively. The relatively uniform surface morphologies were observed from both deposited thin films. In_2O_3 thin film thickness was measured by a Veeco Dektak 8 Stylus Profiler and showed the average film thickness to be around 100 nm for both thin films.

(a)

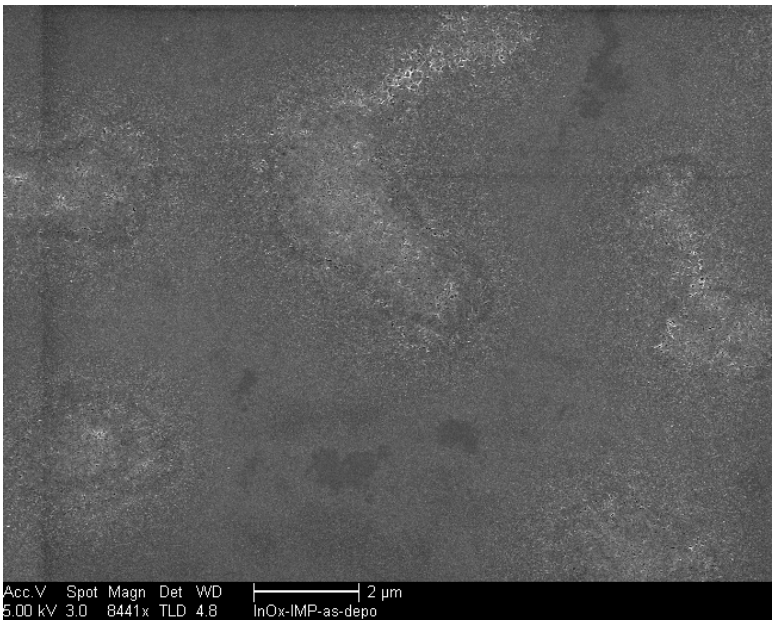

(b)

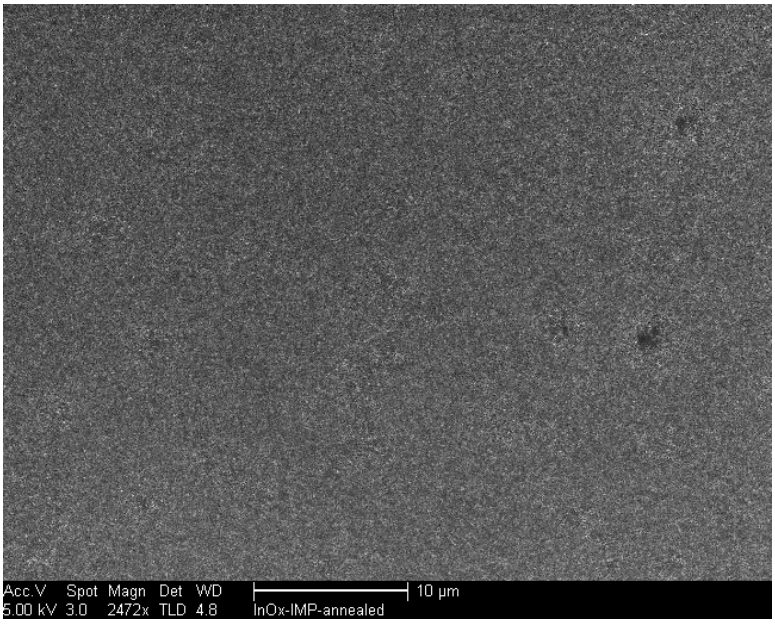

Figure 6.5 Scanning electron microscopy (SEM) images of (a) as-deposited and (b) annealed In_2O_3 thin films taken from the device gate areas.

For the In_2O_3 metal-insulator-semiconductor field-effect transistors (MISFETs) fabrication, a heavily boron (p+) doped silicon substrate served as the gate in an inverted-gate structure. Silicon dioxide with a thickness of 100 nm was thermally grown on top of a silicon substrate and a 500 nm gold layer for gate contact was sputtered on the back side of the Si substrate. A schematic cross-sectional view of the In_2O_3 MISFET structure is shown in Figure 6.6(a).

In order to reduce the gate leakage for the device fabrication, polyimide (Kapton) tape (McMaster-Carr) was used to tightly tape the four edges of the substrate on to a 3 in. diameter stainless steel metallic plate to prevent shorting the device and was heated on a metal hotplate to the temperature range of 70-80 ^oC for 3 min before deposition. The In_2O_3 precursor solution was then pumped into the Tygon tube at a flow rate of ~2.4 ml/min and impinged on top of the pre-heated oxidized silicon substrate for 2.5 mins. Once the process was completed, the substrate was removed from the plate without further rinsing with DI water. After the deposition, both with and without postannealing processes were performed in the air for 1 hour at 300 ^oC. ~100 nm In_2O_3 thin films were deposited on top of the SiO_2 layers. The 300 nm aluminum source and drain contacts were then evaporated on top of the metal oxide layer through a shadow mask with a channel width-to-length ratio of 12 for the annealed thin films and 7 for as-deposited ones (channel length equals 200 μm) in order to complete the process of fabricating In_2O_3 MISFETs.

The device characterization was performed in the dark at a room temperature with a HP 4157B Semiconductor Parameter Analyzer. The drain current-drain voltage (I_{DS}-V_{DS}) output characteristics presented in Figure 6.6(b) show that the as-deposited In_2O_3 MISFET behaves as an n-channel transistor with good gate modulation and hard saturation. We have characterized the MISFET parameters including threshold voltage, drain current on-to-off ratio, turn-on voltage and channel mobility. The threshold voltage for this device is approximated using a linear extrapolation method with the drain current measured as a function of gate voltage at a low V_{DS} to ensure operation in the linear region. The drain current-gate voltage (I_{DS}-V_{GS}) at V_{DS} = 1 V using the linear extrapolation method for threshold estimation, resulted in a threshold voltage of $V_T \cong 11$ V for our fabricated as-deposited In_2O_3 MISFET. However, the precise identification of the threshold voltage to determine the device operation-mode (either enhancement or depletion-mode) is still somewhat ambiguous [54,55]. A more accurate and less ambiguous parameter for device characterization used here is turn-on voltage, the gate voltage at the onset of the initial sharp increase in drain current in a log(I_{DS})-V_{GS} transfer characteristic [54].

The drain current on-to-off ratio determines the switching quality of the MISFET. Figure 6.6(c) shows the log(I_{DS})-V_{GS} transfer characteristic at V_{DS} = 40 V indicating a drain current on-to-off ratio of approximately 10^5 with a turn-on voltage at -4 V. With a positive threshold voltage and a negative turn-on voltage,

this device still behaves as a depletion-mode device that is initially on and requires a negative gate voltage to fully turn off the device [54].

The mobility of a MISFET refers to the carrier mobility that is proportional to the carrier velocity in an electric field. The field-effect mobility (μ_{FE}) was determined from the transconductance of the device at V_{DS} = 1 V to ensure that the mobility was extracted from the linear region. The field-effect mobility for the as-deposited In_2O_3 device presented here is $\mu_{FE} \cong 2.23$ cm^2/V s.

The drain current-drain voltage (I_{DS}-V_{DS}) output characteristics of the 300 ^oC annealed In_2O_3 MISFET presented in Figure 6.6(d) shown that the device also behaves as an n-channel transistor with good gate modulation and hard saturation. We had tried to apply negative gate voltage to -40 V (the highest negative gate voltage that could be applied using our Semiconductor Parameter Analyzer) but still we could not fully turn off this device. The log(I_{DS})-V_{GS} transfer characteristic at V_{DS} = 40 V indicates a drain current on-to-off ratio of approximately 10^2 for applying gate voltage between -40 to 40 V with a turn-on voltage lower than -40 V. The field-effect mobility for the annealed depletion-mode In_2O_3 MISFET presented here was as high as $\mu_{FE} \cong 18.71$ cm^2/V s.

(a)

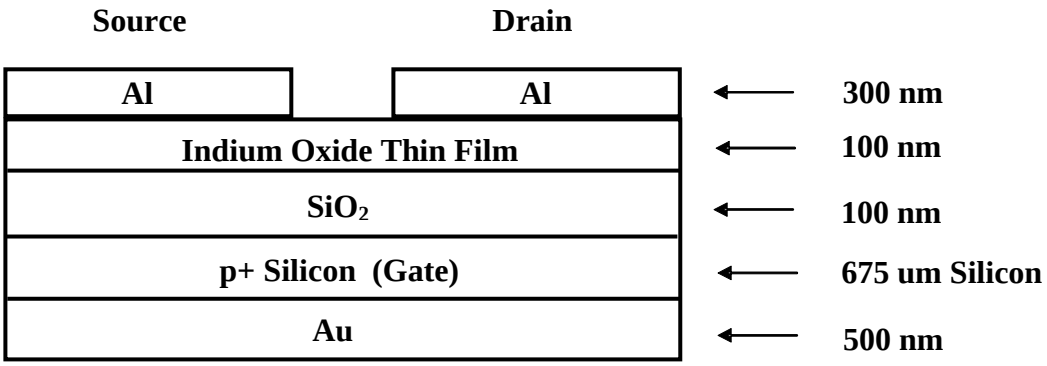
Source
Drain
Al
Al
Indium Oxide Thin Film
SiO2
p+ Silicon (Gate)
Au
300 nm
100 nm
100 nm
675 um Silicon
500 nm

(b)

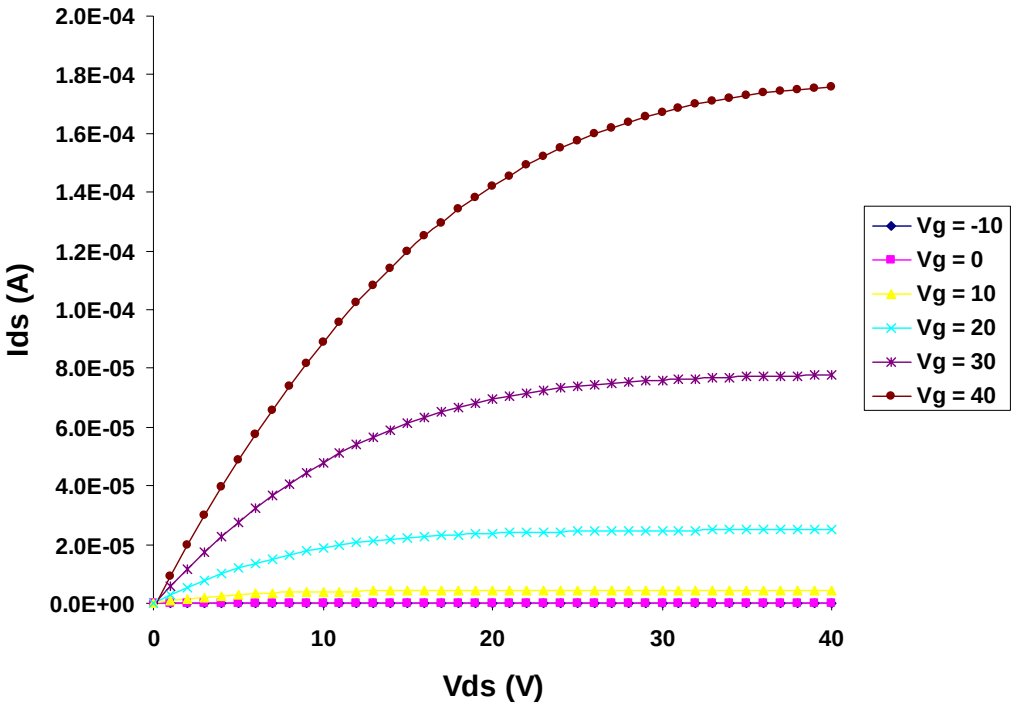
2.0E-04
1.8E-04
1.6E-04
1.4E-04
1.2E-04
1.0E-04
8.0E-05
6.0E-05
4.0E-05
2.0E-05
0.0E+00
Ids (A)
0
10
20
30
40
Vds (V)
Vg = -10
Vg = 0
Vg = 10
Vg = 20
Vg = 30
Vg = 40

(c)

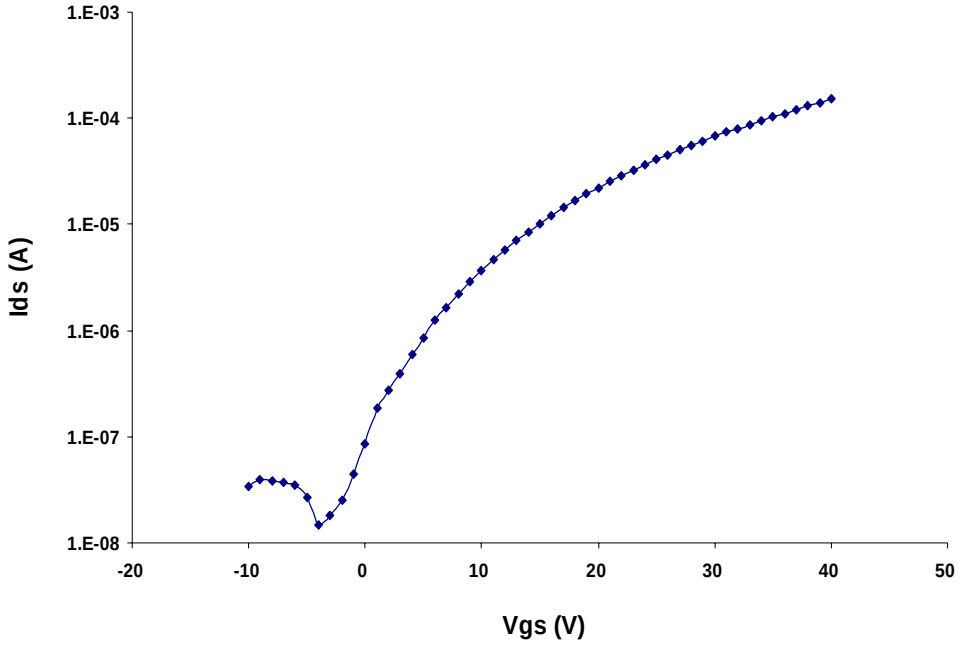
1.E-03
1.E-04
1.E-05
1.E-06
1.E-07
1.E-08
Ids (A)
-20
-10
0
10
20
30
40
50
Vgs (V)

(d)

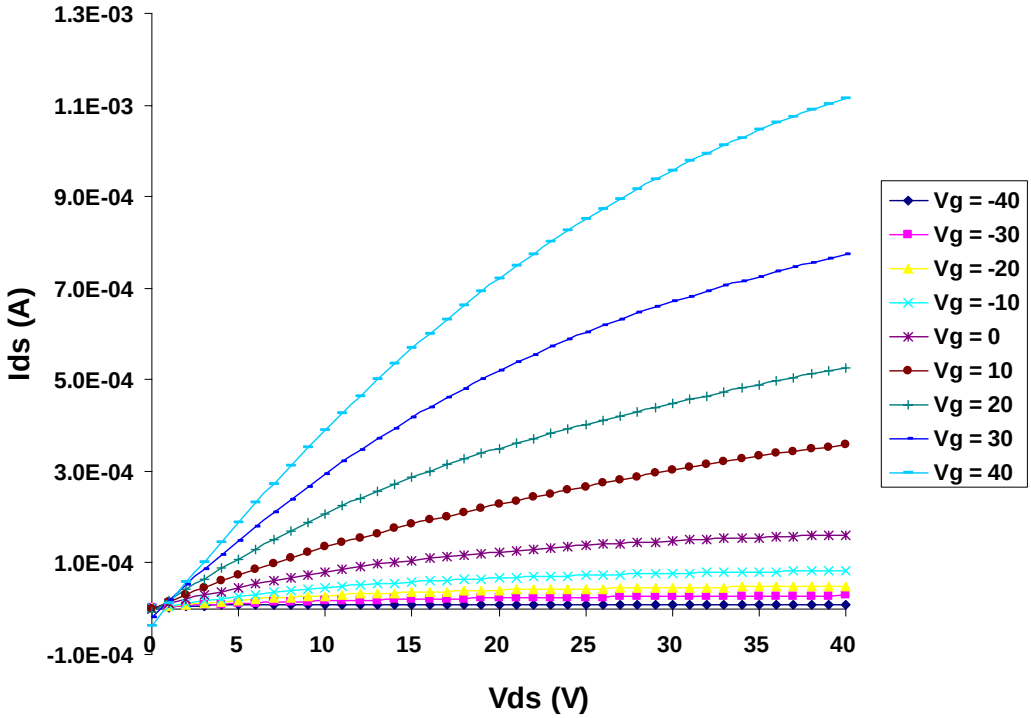
1.3E-03
1.1E-03
9.0E-04
7.0E-04
5.0E-04
3.0E-04
1.0E-04
-1.0E-04
Ids (A)
0
5
10
15
20
25
30
35
40
Vds (V)
Vg = -40
Vg = -30
Vg = -20
Vg = -10
Vg = 0
Vg = 10
Vg = 20
Vg = 30
Vg = 40

Figure 6.6 (a) Schematic cross-sectional view of the In_2O_3 MISFET structure (b) Drain current-drain voltage (I_{DS}-V_{DS}) output characteristics of as-deposited In_2O_3 MISFET for a channel width-to-length ratio of 7 (c) Drain current on-to-off ratio determination at V_{DS} = 40 V (d) Drain current-drain voltage (I_{DS}-V_{DS}) output characteristics of annealed In_2O_3 MISFET for a channel width-to-length ratio of 12.

CHAPTER 7

CONCLUSIONS AND FUTURE RECOMMENDATIONS

Conclusions

In this dissertation, the recent progress in fabricating Cadmium Sulfide (CdS) thin film transistors (TFTs) using Chemical Bath Deposition (CBD) to deposit the well known II-VI semiconductor CdS channel layers was reported. Device characteristics of an enhancement-mode CdS metal insulator semiconductor field-effect transistor (MISFET) with a field-effect mobility of ~1.5 cm^2/V s, a threshold voltage of V_T ~14 V and a current on-to-off ratio of ~10^6 were achieved using CdS films deposited by a batch process and subjected to 500 ^oC rapid thermal annealing in an Ar atmosphere. Though CBD has many advantages, it suffers from some major drawbacks. For a better understanding and optimization of the CBD process, a continuous flow microreactor was used to overcome the drawbacks associated with conventional chemical bath deposition and have implemented it for the deposition of CdS thin films was developed.

This novel reactor provides the benefit of introducing a constant flux of reactant solutions to the system (continuous process) through an interdigital micromixer (IMM) to achieve efficient mixing of the reactant streams in a short residence time. It also provides the temporal resolution to control the homogeneous reaction of the chemical solution before it impinges on the substrate surface. This capability was used to decouple the homogeneous particle formation

and deposition from the molecular level heterogeneous surface reaction. Transmission electron microscopy (TEM) analysis indicated an impinging flux without the formation of nanoparticles which could be obtained from this reactor at short residence times. An impinging flux without the formation of nanoparticles enabled us to deposit extremely smooth and highly oriented nanocrystalline CdS semiconductor thin films at a low temperature of 80 ^{o}C. Enhancement-mode functional thin film transistors with an effective mobility of μ_{eff} =1.46 cm^2/V s, drain current on-to-off ratio of approximately 10^5 and turn-on voltage at 0 V were fabricated from the as-deposited films without any post annealing process. In addition, the reactor could be operated in a homogeneous particle formation regime. Size increasing CdS nanoparticles grown by homogeneous reaction were clearly observed from TEM and corresponding SEM micrographs by increasing the residence time from 1 to 280 sec using pre-heated precursor solutions. The formation of CdS nanorods and arrayed nanorod bundle structures using the CBD recipe were also observed in certain area and reported here for the first time.

An impinging flux without the homogeneous particle formation can be obtained from a short residence time of 1 sec with the solution temperature maintained at 80 ^{o}C based on the TEM characterization. By using this particle-free flux, the study of the CdS growth kinetics can be simplified by focusing on the heterogeneous surface reaction through a molecule-by-molecule growth mechanism. These results suggest that the HS^- ions formed through the thiourea

hydrolysis reaction are the dominant sulfide ion source responsible for the CdS deposition rather than the thioura itself that had widely been discussed in almost all of the previous literature. Growth experiments using the pre-mixed $SC(NH_2)_2$ and NH_4OH and $CdCl_2$ and Na_2S systems provide additional supports for this hypothesis. This finding can not be found previously by a conventional CBD batch setup because all the reactant solutions were sequentially pulled into the reaction beaker and mixed all at once. However, using our reactor, we were able to control the mixing elements and sequence based on the design of our experiments.

The low value of activation energy (~44 KJ/mol) obtained from the 1-sec residence time could be contributed to the heterogeneous surface reaction of the rate limiting step for CdS thin film formation based on our newly proposed growth mechanism when very low HS^- concentration was formed at this processing condition. When increasing the residence time from 3.5 to 70 sec, the values of activation energy increased from ~60 to 64 KJ/mol. At these reaction conditions, the higher HS^- concentration was formed; therefore, the higher activation energy could be responsible for the combination of thiourea hydrolysis reaction and reaction of the rate limiting step for CdS thin film formation.

This microreactor could be adapted for the deposition of other compound semiconductor thin films at low temperatures using chemical solution deposition and opens a low-cost avenue to fabricate thin film flexible electronics on polymeric substrates. Due to environmental safety issues, other cadmium free

semiconductor materials using solution-based deposition process were carried out. A newly developed precursor solution was used to deposit highly transparent amorphous Indium Oxide (In_2O_3) thin films through a solution-based deposition process at a low-temperature of ~70 ^oC. Depletion-mode In_2O_3 metal–insulator-semiconductor field-effect transistors (MISFETs) with the field-effect mobility (μ_{FE}) as high as 18.71 and 2.23 cm^2/V s were obtained for devices with and without postannealing processes performed in the air for 1 hour at 300 ^oC, respectively. This demonstrated a promising way that is capable of fabricating transparent flexible electronics on polyethylene terephthalate (PET) or polyimide (Kapton) polymeric substrates using the solution-processed Indium Oxide (In_2O_3) thin films as the active channel layers.

Future Recommendations

Three categories for future research studies are discussed here in order to better understand and optimize the CdS thin film deposition by the continuous flow microreactor.

1. The alternative chemical for ammonia:

Due to the volatility of ammonia, its concentration will be influenced by the surrounding environment. The variation of ammonia concentration will further influence the pH value and the cadmium complex concentration as well. Using low

volatile ethylenediamine as the complexing agent to replace the ammonia might be an alternative choice, and this had been discussed in recent published literature [97].

2. The material selection for the reactor tube:

CdS thin films could deposit inside the wall of the PEEK tube (hydrophilic material) during the deposition process. However, after a certain period of time, those deposited films could be washed away by the forthcoming reactant streams resulting in the pilling-off of thin films set on the surface of the substrate. In order to solve this problem, a selected hydrophobic material such as Teflon to replace PEEK for the tube could potentially prevent the CdS deposition in side the tube.

3. The experimental measurement:

Based on the experiences and experimental results, three different measurements are discussed in order to obtain the precise experimental values.

First is the in-situ growth rate measurement. The Quartz Crystal Microbalance (QCM) connected with a flow cell was initially tried to obtain the in-situ growth rate data for continuous flow microreactor. However, some difficulties were experienced. For example, due to the flow directly impinging (perpendicularly) on the quartz crystal, the force of the stream will cause the sudden increase of the growth rate right at the beginning and sometimes experience the problem for continuing reading the experimental data. The quartz

crystal cannot be pre-heated directly and acts as a cold surface which cannot exactly simulate the continuous flow deposition process. Therefore, the thickness of the thin films was measured directly by a surface profiler. To solve these encountered problems, a new setup with the capability of measuring the growth rates of the thin films in real time is needed. This new setup should have the ability to control the temperature of the quartz crystal and allow the continuous flow passing through the crystal horizontally with a well defined fluid flow. Therefore, the precise film thickness for the continuous flow microreactor can be measured in real time.

Second is the induction time measurement. The conductivity measurement was initially tried to determine the value of the precipitation induction time based on the measurement of conductivity changes in supersaturated solutions [64,98]. However, the time resolution for commercial available conductivity probe is still considerably low (~1 sec). In order to obtain the precise value of the precipitation induction time, a new experimental setup for the conductivity measurement with the time resolution down to the microsecond is required. One possible approach would be having the mixture solutions from the continuous flow microreactor (after passing through the interdigital micromixer for rapid mixing) pass through two electrodes (opposite to each other within a certain distance) which connect to Impedance/Gain-Phase Analyzer (Solartron, SI 1260). Therefore, the precise value of conductivity changes in real time could be obtained from converting the resistivity data versus time characterized by the impedance analyzer.

Third is the concentration measurement of HS^- and S^{2-}. Based on experimental results, when a 70-sec residence time was used, the decrease of the growth rate was observed. The decrease of the growth rate could be contributed to higher S^{2-} concentration was formed through equation 2.5 that further consumed the HS^- concentration and resulting to lower growth rate and lower film thickness. The possible explanation of those experimental results mentioned above could be attributed to the real HS^- and S^{2-} concentrations which are different from the calculated values shown in Table 5.8. Therefore, experimentally determined HS^- and S^{2-} concentrations in real time are needed.

BIBLIOGRAPHY

[1] *Flexible flat panel displays*, edited by G. P. Crawford, John Wiley & Sons, New York (2005).

[2] H. E. A. Huitema, G. H. Gelinck, J. B. P. H. van der Putten, K. E. Kuijk, C. M. Hart, E. Cantatore, P. T. Herwig, A. J. J. M. van Breemen, and D. M. de Leeuw, *Nature*, **414**, 599 (2001).

[3] Y. Chen, J. Au, P. Kazlas, A. Ritenour, H. Gates, and M. McCreary, *Nature*, **423**, 136 (2003).

[4] Y.-J. Chang C. L. Munsee, G. S. Herman, J. F. Wager, P. Mugdur, D.-H. Lee, and C.-H. Chang, *Surf. Interface Anal*., **37**, 398 (2005).

[5] C. Voss, Y.-J. Chang, S. Subramanian, S. O. Ryu, T.-J. Lee, and C.-H. Chang, *J. Electrochem. Soc*., **151**(10), C655 (2004).

[6] M. Froment, M. C. Bernaed, R. Cortes, B. Mokili, and D. Lincot, *J. Electrochem. Soc*., **142**(8), 2642 (1995).

[7] M. Isshiki, T. Endo, K. Masumoto, and Y. Usui, *J. Electrochem. Soc*., **137**(9), 2697 (1990).

[8] P.K. Nair, M.T. S. Nair, V. M. Garcia, O. L. Arenas, Y. Pena, A. Castillo, I.T. Ayala, O. Gomez-daza, A. Sanchez, J. Campos, H. Hu, R. Suarez, M. E. Rincon, *Sol. Energy Mater. Sol. Cells*, **52**, 313 (1998).

[9] O. Savadogo, *Sol. Energy Mater. Sol. Cells*, **52,** 361 (1998).

[10] Y.-J. Chang, P. H. Mugdur, S-.Y. Han, A. A. Morrone, S. O. Ryu, T.-J. Lee, and C.-H. Chang, *Electrochem. Solid-State Lett*., **9**(5), G174 (2006).

[11] S.-Y. Han, Y.-J. Chang, D.-H. Lee, S.-O. Ryu, T.-J. Lee, and C.-H. Chang, *Electrochem. Solid-State Lett*., **10**(1), K1 (2007).

[12] J. Liebig, *Ann. Pharmaz*., **14**, 134 (1835).

[13] C. Puscher, *Dingl. J.*, **190**, 421 (1869).

[14] E. Beutel, Z. Angew, *Chem*., **26**, 700 (1913).

[15] E. Beutel, A. Kutzelnigg, *Z. Elektrochem*., **36**, 523 (1930).

[16] E. Beutel, A. Kutzelnigg, *Monats*., **58**, 295 (1931).

[17] J. E. Reynolds, *J. Chem. Soc*., **45**, 162 (1884).

[18] G. Rosenheim,W. Stadler, V. J. Mayer, *Z. Anorg. Chem.*, **49**, 1 (1906).

[19] G. Rosenheim,W. Stadler, V. J. Mayer, *Z. Anorg. Chem.*, **49**, 13 (1906).

[20] S. G. Mokrushin,Y. V. Tkachev, *Kolloidn Zh.*, **23**, 438 (1961).

[21] R.A.Zingaro, D.O.Skovlin, *J. Electrochem. Soc*., **11**, 42 (1964).

[22] K. L. Chopra, R.C. Kainthla, D. K. Pandya, A. P. Thakoor, In: *Physics of Thin Films*, Academic Press, New York and London, **12**, 167 (1982).

[23] P. K. Nair, M. T. S. Nair, J. Campos, L. E. Sansores, *Solar cells*, **22**, 211 (1987).

[24] P. K. Nair, M. T. S. Nair, *Solar Energy Mater.*, **15**, 431 (1987).

[25] C. D. Lokhande, *Mater. Chem. Phys*., **28**, 1 (1991).

[26] D. Lincot, R. Ortega-Borges, *J. Electrochem. Soc.,* **139**(7), 1880 (1992).

[27] R. Ortega-Borges, D. Lincot, *J. Electrochem. Soc.,* **140**(12), 3464 (1993).

[28] D. Lincot, M. Froment, H. Cachet, In: Alkire RC, Kolb DM. *Eds. Adv. Electrochem. Sci. Eng*., New York: Wiley-VCH, **6**, 165 (1998).

[29] M. Froment, M. Claude Bernard, R. Cortes, *J. Electrochem. Soc*., **142**(8), 2642 (1995).

[30] H. Uda, H. Taniguchi, M. Yoshida, T. Yamashita, *Jpn. J. Appl. Phys.*, **17**, 585 (1978).

[31] R. W. Birkmire, B. E. McCandless, W. N. Shafarman, R. D. Varrin Jr. In: 9th ECPV Solar Energy Conf., Freiberg, Germany, 134 (1989).

[32] R. H. Mauch, M. Ruckh, J. Hedström, D. Lincot, J. Kessler, R. Klinger, L. Stolt, J. Vedel, H.-W. Schock. In: 10th ECPV Solar Energy Conf., Lisbon, Portugal, 1415 (1991).

[33] T. L. Chu, S. S. Chu, C. Ferekides, C. Q. Wu, J. Britt, C. Wang, *J. Appl. Phys*., **70**, 7608 (1991).

[34] T. L. Chu, S. S. Chu, N. Schultz, C. Wang, C. Q. Wu, *J. Electrochem. Soc*., **139**, 2443 (1992).

[35] A. P. Alivisatos, *Science*, **271**, 933 (1996).

[36] M. V. Rama, Krishna, R. A. Friesner, *J. Chem. Phys*., **95**(11), 8309 (1991).

[37] G. Hodes, A. Albu-Yaron, F. Decker, P. Motisuke, *Phys. Rev. B*., **36**, 4215 (1987).

[38] S. Gorer, G. Hodes, *J. Phys. Chem*., **98**, 5338 (1994).

[39] G. A. Kitaev, A. A. Uritskarya, S. G. Morkrushin, *Russ. J. Phys. Chem*., **39**, 1101 (1965).

[40] G. A. Kitaev, Y. N. Makurin, V. I. Dvoinin, *Russ. J. Phys. Chem*., **50**, 1828 (1976).

[41] N. D. Betenekov, V. P. Medvedev, A. S. Zhukovskaya, G. A. Kitaev, *Sov. Radiochem.*, **20**, 524 (1978).

[42] I. Kaur, D. K. Pandya, K. L. Chopra, *J. Electrochem. Soc.*, **140**, 943 (1980).

[43] P. C. Rieke, S. B. Bentjen, Chem. Mater., **5**, 43 (1993).

[44] J. M. Dona, J. Herrero, *J. Electrochem. Soc*., **144**(11), 4081 (1997).

[45] P. K. Nair, P. Parmananda, M. T. S. Nair, *J. Cryst. Growth*, **206**, 68 (1999).

[46] M. Kostoglou, N. Andritsos, A. J. Karabelas, *Ind. Eng. Chem. Res*., **39**, 3272 (2000).

[47] M. Kostoglou, N. Andritsos, A. J. Karabelas, *Thin Solid Films*, **387**, 115 (2001).

[48] J. A. Dirksen, T. A. Ring, *Chem. Eng. Sci*., **46**(10), 2389 (1991).

[49] R. G. Carbonell, D. T. Riley, *J. Colloid Interface Sci*., **158**, 274 (1993).

[50] M. Kostoglou, N. Andritsos, A. J. Karabelas, *J. Colloid Interface Sci*., **263**, 177 (2003).

[51] P. K. Weimer, "*An Evaporated Thin-Film Triode*" presented at the IRE-AICE Device Res. Conf., Stanford Univ., Stanford, CA (1961).

[52] M. Shur, M. Hack, *J. Appl. Phys.,* **55**, 3831 (1984).

[53] M. Shur, M. Hack, J. G. Shaw, *J. Appl. Phys.,* **66**, 3371 (1989).

[54] R. L. Hoffman, *J. Appl. Phys*., **95**, 5813 (2004).

[55] D. K. Schroder, *Semiconductor Material and Device Characterization,* 2nd ed., John Wiley & Sons, Inc., New York (1998).

[56] R. F. Pierret, *Field Effect Devices,* 2nd ed., Addison-Wesley Publishing Company, Inc., New York (1990).

[57] F. Y. Gan, I. Shih, *IEEE Transactions on Electron Devices*, **49,** 15 (2002).

[58] F. Y. Gan, I. Shih, *Journal of Vacuum Science & Technology, A: Vacuum, Surface and Films*; **20**, 1365 (2002).

[59] C. Voss, S. Subramanian, C.-H. Chang, *J. Appl. Phys*., **96**(10), 5819 (2004).

[60] B. Mereu, G. Sarau, E. Pentia, V. Draghici, M. Lisca, T. Botila, L. Pintilie, *Materials Science & Engineering, B: Solid-State Materials for Advanced Technology*; **109,** 260 (2004).

[61] S. M. Sze, *Physics of Semiconductor Devices* (2^{nd} edn), appendix G, John Wiley, 849 (1981).

[62] P. K. Nair, V. M. Garcia, O. Gomez-Daza, M. T. S. Nair, *Semicond. Sci. Technol*., **16**, 855 (2001).

[63] P. H. Mugdur, Y.-J. Chang, S-.Y. Han, A.A. Morrone, S. O. Ryu, T.-J. Lee, and C.-H. Chang, *J. Electrochem. Soc*., revising (2007).

[64] J. W. Mullin, *Crystallization*, chapter 5, Butterworth-Heinemann, Oxford, 206 (2001).

[65] H. Löwe, W. Ehrfeld, V. Hessel, T. Richter, J. Schiewe, Proceedings of the 4th International Conference on Microreaction Technology, IMRET 4, 31 (2000).

[66] D. Bökenkamp, A. Desai, X. Yang, Y.-C. Tai, E. M. Marzluff, S. L. Mayo., *Anal. Chem.*, **70**, 232 (1998).

[67] Institut für Mikrotechnik Mainz, Germany, *Operating manual for SSIMM* (2004).

[68] JCPDS card numbers: 80-0019, 75-0581, 42-1411, 75-1546.

[69] H. Zhang, D. Yang, X. Ma, Y. Ji, S. Li and D. Que, *Mater. Chem. & Phys.*, **93**, 65 (2005).

[70] H. Zhang, D. Yang, X. Ma, and D. Que, *Mater. Lett.*, **59**, 3037 (2005).

[71] C.-S. Yang, D. D. Awschalom, and G. D. Stucky, *Chem. Mater.*, **13**, 594 (2001).

[72] C. Bao, M. Jin, R. Lu, P. Xue, Q. Zhang, D.Wang, and Y. Zhao, *J. of Solid State Chemistry*, **175**, 322 (2003).

[73] W. Wang, and F. Bai, *Chem. Phys. Chem.*, **4**, 761 (2003).

[74] Y.-W. Jun, S.-M. Lee, N.-J. Kang, and J. Cheon, *J. Am. Chem. Soc.*, **123**, 5150 (2001).

[75] J. A. Ascencio, P. Santiago, L. Rendón, and U. Pal, *Appl. Phys. A*, **78**, 5 (2004).

[76] F. Gao, Q. Lu, S. Xie, and D. Zhao, *Adv. Mater.*, **14**(21), 1537 (2002).

[77] P. Yan, Y. Xie, Y. Qian, and X. Liu, *Chem. Commun.*, 1293 (1999).

[78] A. P. Alivisatos, *Science*, **271**, 933 (1996).

[79] G. Marcotrigiano, G. Peyronel, R. Battistuzzi, *J. Chem. Soc., Perkin Trans*., 2, 1539 (1972).

[80] G. Hodes, *Chemical Solution Deposition of Semiconductor Films*, Marcel Dekker, Inc., New York (2003).

[81] *Transparent Conducting Oxides*, *MRS Bulletin***, 25**(8), 22 (2000).

[82] K. L. Chopra, S. Major, and D. K. Pandya, *Thin Solid Films,* **102**, 1 (1983).

[83] R. L. Hoffman, B. J. Norris, and J. F. Wager, *Appl. Phys. Lett.*, **82**, 733 (2003).

[84] S. Masuda, k. Kitamura, Y. Okumura, S. Miyatake, and T. Kawai, *J. Appl. Phys*., **93**, 1624 (2003).

[85] B. J. Norris, J. Anderson, J. F. Wager, and D. A. Keszler, *J. Phys. D: Appl. Phys*., **36**, L105 (2003).

[86] B. Sun and H. Sirringhaus, *Nano Lett*., **5**(12), 2408 (2005).

[87] R. E. Presley, C. L. Munsee, C.-H. Park, D. Hong, J. F. Wager, and D. A. Keszler, *J. Phys. D: Appl. Phys.*, **37**, 2810 (2004).

[88] J. F. Wager, *Science*, **300**, 1245 (2003).

[89] T. Minami, *J. Vac. Sci. Technol. A*., **17**(4), 1765 (1999).

[90] T. Minami, S. Tsukada, Y. Minamino, and T. Miyata, *J. Vac. Sci. Technol. A*., **23**(4), 1128 (2005).

[91] T. Minami, T. Miyata, and T. Yamamoto, *Surf. Coat. Technol*., **108-109**, 583 (1998).

[92] L. Wang, M.-H. Yoon, G. Lu, Y. Yang, A. Facchetti, and T. J. Marks, *Nature*, **5**, 893 (2006).

[93] Y.-C. Shih, C. X. Qiu, I. Shih, and C. Qiu, U. S. patent 20050275038.

[94] Y.-J. Chang, D.-H. Lee, G. S. Herman, and C.-H. Chang, *Electrochem. Solid-State Lett.*, in press (2007).

[95] D.-H. Lee, Y.-J. Chang, G. S. Herman, C.-H. Chang, *Adv. Mater.*, in press (2007).

[96] N. L. Dehuff, E. S. Kettenring, D. Hong, H. Q. Chiang, and J. F. Wager, *J. Appl. Phys.*, **97**, 064505 (2005).

[97] M. D. Archbold, D. P. Halliday, K. Durose, T. P. A. Hase, D. S. Boyle, S. Mazzamuto, N. Romeo, and A. Bosio, *Thin Solid Films*, **515**(5), 2954 (2007).

[98] O. Söhnel, J. W. Mullin, *J. Crystal. Growth*, **44**, 377 (1978).

APPENDICES

APPENDIX A

Experimental Data for Activation Energy

A1 Activation Energy for 3.5 sec Residence Time

Table A1.1 Average CdS thin film thicknesses deposited at different temperatures and deposition times for a 3.5-sec residence time.

	Average CdS thin film thicknesses (Å) at different temperatures				
Deposition time (min)	60 ^{o}C	65 ^{o}C	70 ^{o}C	75 ^{o}C	80 ^{o}C
1	70	100	130	180	200
3	220	350	500	760	850
5	400	550	900	1100	1300
10	900	1200	1600	2300	3000

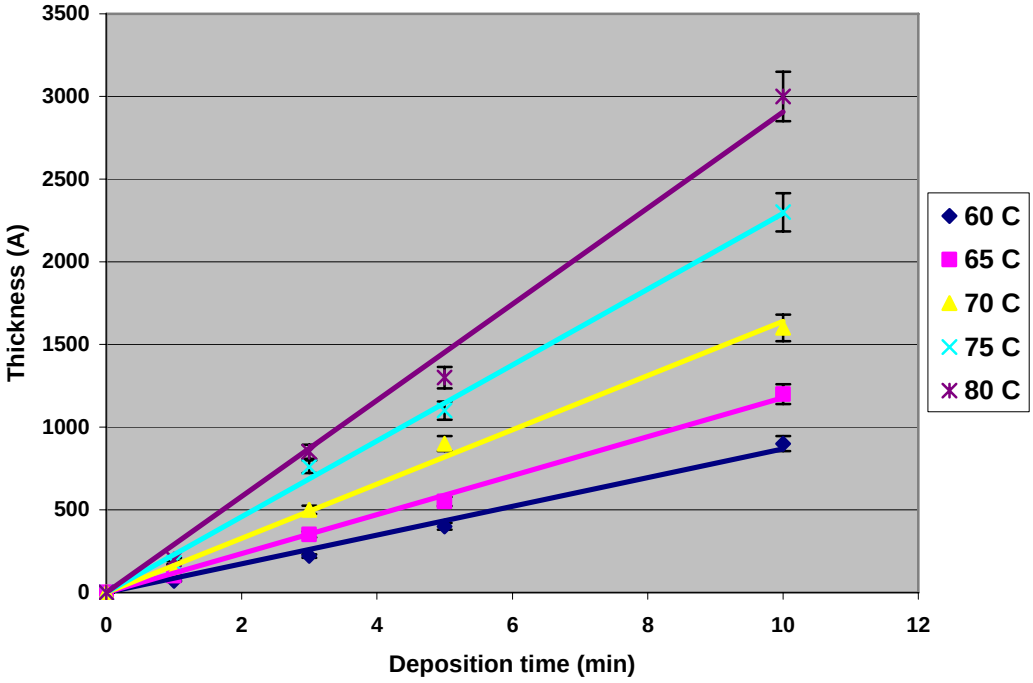

Figure A1.1 CdS thin film thickness versus deposition time at different operating temperatures for a 3.5-sec residence time.

Table A1.2 CdS thin film growth rates obtained from a 3.5-sec residence time at different operating temperatures.

Temperature (^{o}C)	60	65	70	75	80
Growth rate (Å/min)	86.889	117.78	163.93	229.33	290.74

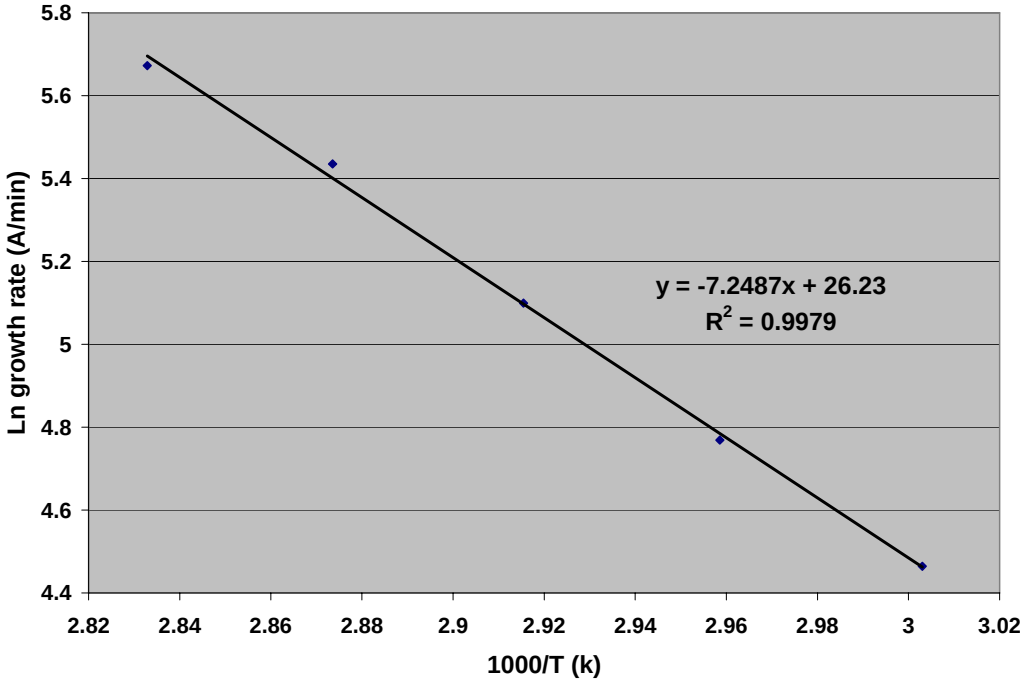

Figure A1.2 Neperian logarithm of the growth rate as a function of 1000/T (k) obtained from a 3.5-sec residence time at different operating temperatures.

Activation Energy = 60.27 KJ/mol

A2 Activation Energy for 7 sec Residence Time

Table A2.1 Average CdS thin film thicknesses deposited at different temperatures and deposition times for a 7-sec residence time.

	Average CdS thin film thicknesses (Å) at different temperatures				
Deposition time (min)	60 °C	65 °C	70 °C	75 °C	80 °C
1	80	110	180	220	250
3	250	400	600	900	1000
5	450	600	1000	1300	1500
10	1000	1300	1900	2600	3400

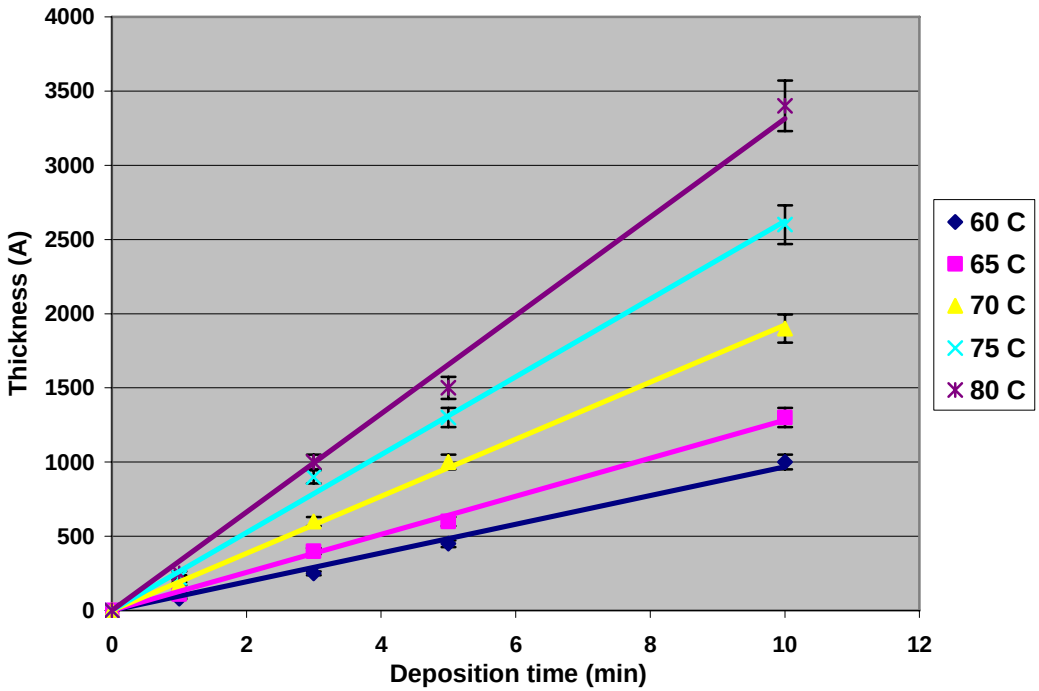

Figure A2.1 CdS thin film thickness versus deposition time at different operating temperatures for a 7-sec residence time.

Table A2.2 CdS thin film growth rates obtained from a 7-sec residence time at different operating temperatures.

Temperature (^{o}C)	60	65	70	75	80
Growth rate (Å/min)	96.889	128.22	192.44	262.37	331.48

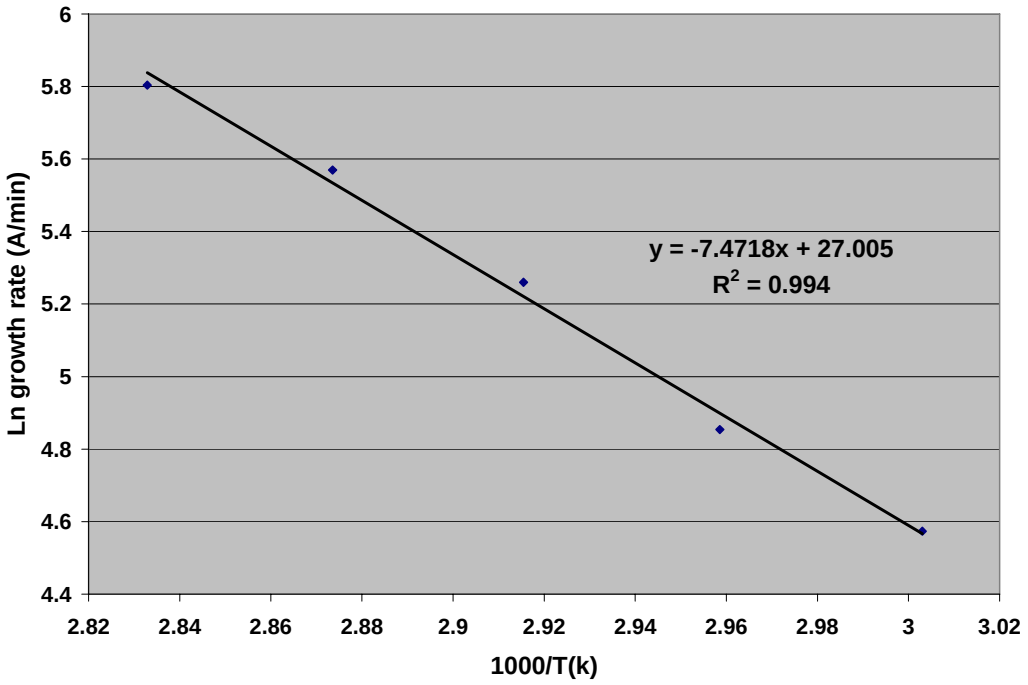

Figure A2.2 Neperian logarithm of the growth rate as a function of 1000/T (k) obtained from a 7-sec residence time at different operating temperatures.

Activation Energy = 62.12 KJ/mol

A3 Activation Energy for 35 sec Residence Time

Table A3.1 Average CdS thin film thicknesses deposited at different temperatures and deposition times for a 35-sec residence time.

	Average CdS thin film thicknesses (Å) at different temperatures				
Deposition time (min)	60 °C	65 °C	70 °C	75 °C	80 °C
1	100	150	250	380	400
3	300	500	700	1000	1200
5	550	720	1100	1500	1800
10	1100	1450	2100	3000	3800

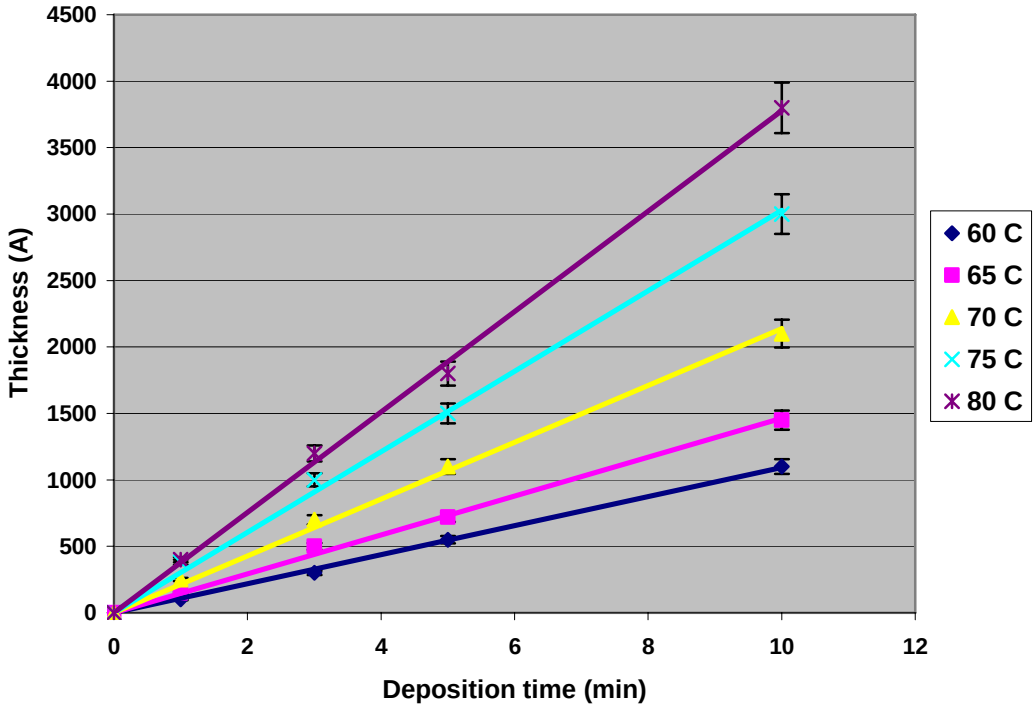

Figure A3.1 CdS thin film thickness versus deposition time at different operating temperatures for a 35-sec residence time.

Table A3.2 CdS thin film growth rates obtained from a 35-sec residence time at different operating temperatures.

Temperature (^{o}C)	60	65	70	75	80
Growth rate (Å/min)	109.26	146.3	213.7	302.81	377.78

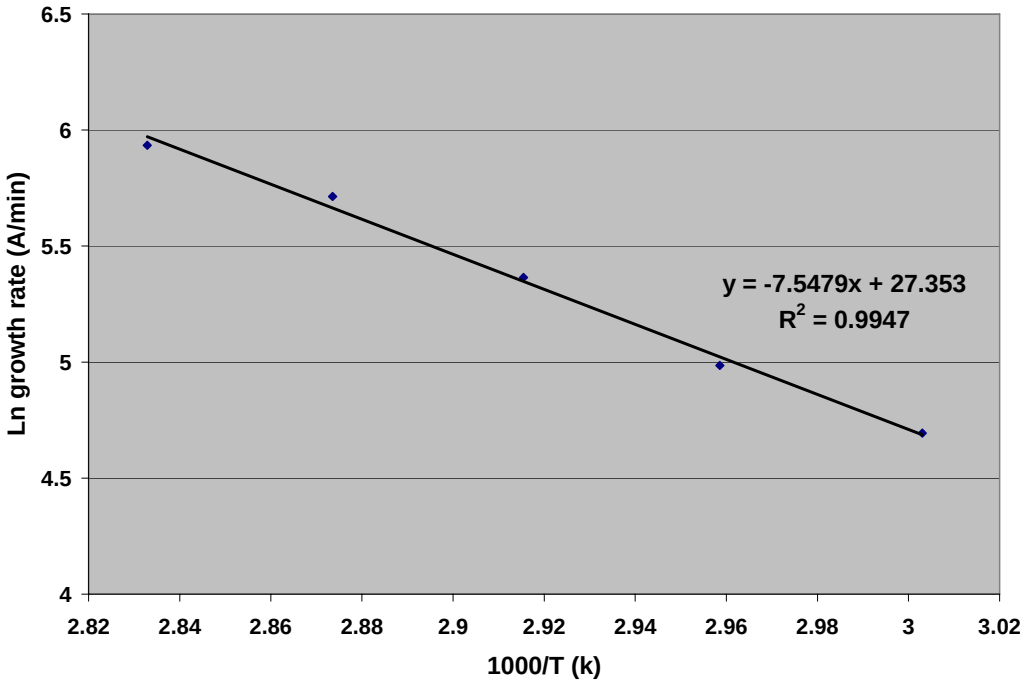

Figure A3.2 Neperian logarithm of the growth rate as a function of 1000/T (k) obtained from a 35-sec residence time at different operating temperatures.

Activation Energy = 62.75 KJ/mol

A4 Activation Energy for 70 sec Residence Time

Table A4.1 Average CdS thin film thicknesses deposited at different temperatures and deposition times for a 70-sec residence time.

	Average CdS thin film thicknesses (Å) at different temperatures				
Deposition time (min)	60 °C	65 °C	70 °C	75 °C	80 °C
1	150	230	350	440	480
3	240	370	600	750	800
5	430	550	950	1200	1400
10	900	1200	1800	2500	3300

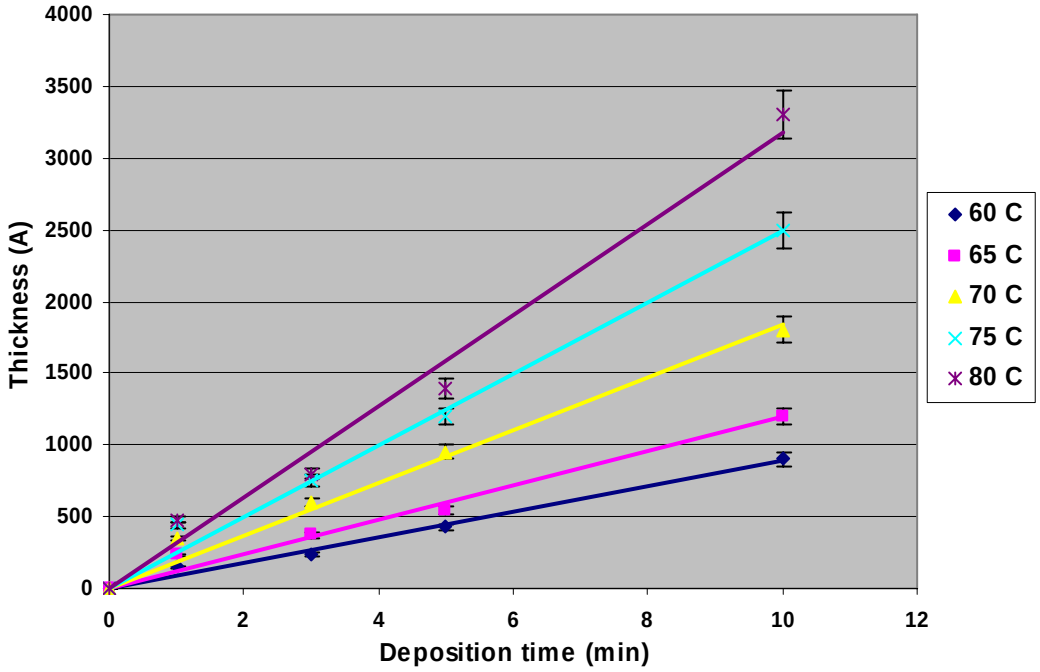

Figure A4.1 CdS thin film thickness versus deposition time at different operating temperatures for a 70-sec residence time.

Table A4.2 CdS thin film growth rates obtained from a 70-sec residence time at different operating temperatures.

Temperature (^{o}C)	60	65	70	75	80
Growth rate (Å/min)	89.037	119.19	184.44	249.56	317.63

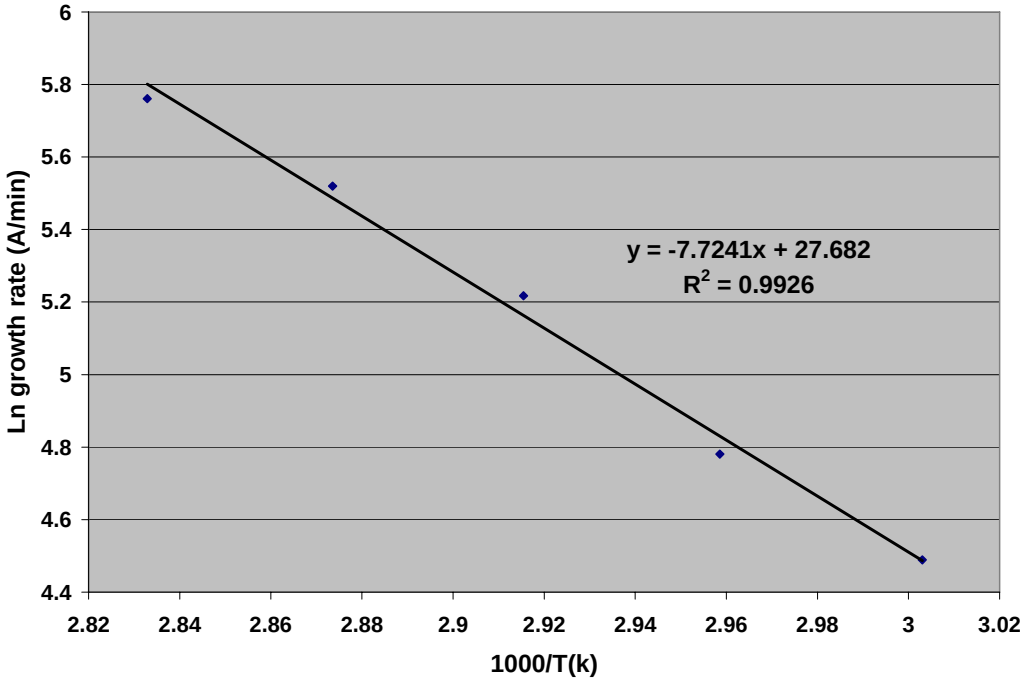

Figure A4.2 Neperian logarithm of the growth rate as a function of 1000/T (k) obtained from a 70-sec residence time at different operating temperatures.

Activation Energy = 64.22 KJ/mol

APPENDIX B

Referred Publications

1. P. H. Mugdur, **Y.-J. Chang**, S.-Y. Han, A. A. Morrone, S.-O. Ryu, T.-J. Lee and C.-H. Chang, "*A Comparison of Chemical Bath Deposition of CdS from a Batch Reactor and a Continuous Flow Microreactor*", Journal of The Electrochemical Society, revising, 2007.

2. **Y.-J. Chang**, D.-H. Lee, G. S. Herman, and C.-H. Chang, "*High-Performance Spin-Coated Zinc Tin Oxide Thin-Film Transistors*", Electrochemical and Solid-State Letters, in press, 2007.

3. D.-H. Lee, **Y.-J. Chang**, G. S. Herman, C.-H. Chang, "*A General Route to Printable High-Mobility Transparent Amorphous Oxide Semiconductors*", Advanced Materials, in press, 2007.

4. S.-Y. Han, **Y.-J. Chang**, D.-H. Lee, S.-O. Ryu, T.-J. Lee, and C.-H. Chang, "*Chemical Nanoparticle Deposition of Transparent ZnO Thin Films*", Electrochemical and Solid-State Letters, 10(1), K1-K5, 2007.

5. D.-H. Lee, **Y.-J. Chang**, G. S. Herman, C.-H. Chang, "*A General and Low-cost Route to Printable High-Mobility Inorganic Thin Film Transistors*", Digital Fabrication, 27-30, 2006.

6. S.-Y. Han, D.-H. Lee, **Y.-J. Chang**, S.-O. Ryu, T.-J. Lee, and C.-H. Chang, "*The Growth Mechanism of Nickel Oxide Thin Films by Room-Temperature Chemical Bath Deposition*", Journal of The Electrochemical Society, 153(6), C382-C386, 2006.

7. **Y.-J. Chang**, P. H. Mugdur, A. A. Morrone, S.-Y. Han, S.-O. Ryu, T.-J. Lee and C.-H. Chang, "*Nanocrystalline CdS MISFETs Fabricated by a Novel Continuous Flow Microreactor*", Electrochemical and Solid-State Letters, 9(5), G174 -G177, 2006.

8. P. H. Mugdur, A. A. Morrone, S.-Y. Han, **Y.-J. Chang**, S.-O. Ryu, T.-J. Lee and C.-H. Chang, "*Micro-and Nano Characterizations of Nanocrystalline CdS Thin Films from a Continuous Impinging Flow Microreactor*", Microscopy and Microanalysis 11, (Suppl. 2), 1954 -1955, 2005.

9. **Y.-J. Chang**, C. L. Munsee, G. S. Herman, J. F. Wager, P. H. Mugdur, D.-H. Lee and C.-H. Chang, ”*Growth, Characterization and Application of CdS Thin Films Deposited by Chemical Bath Deposition*”, Surface and Interface Analysis, 37(4), 398-405, 2005.

10. C.-H. Chang, **Y.-J. Chang**, D.-H. Lee, S.-O. Ryu, T.-J. Lee, ”*Characterization and Application of Semiconductor Thin Films Deposited by Chemical Bath Deposition*”, Microscopy and Microanalysis 10, (Suppl. 2), 610-611, 2004.

11. C. Voss, **Y.-J. Chang**, S. Subramanian, S.-O. Ryu, T.-J. Lee and C.-H. Chang, ”*Growth Kinetics of Thin Film Cadmium Sulfide by Ammonia-Thiourea Based Chemical Bath Deposition (CBD)*”, Journal of The Electrochemical Society, 151(10), C655-C660, 2004.

APPENDIX C

Conference Presentations

1. C.-H. Chang, **Y.-J. Chang**, D.-H. Lee, S.-O. Ryu, T.-J. Lee, "*Investigation of CdS Thin Film Deposition Kinetics Using a Continuous Flow Microreactor*", Reaction Kinetics in Electronic Materials Processing, 45b, The 2006 American Institute of Chemical Engineers (AICHE) Annual Meeting, San Francisco, CA, November 2006.

2. **Y.-J. Chang**, P. H. Mugdur, and C.-H. Chang, "*A Continuous Flow Microreactor for Chemical Bath Deposition*", The 17th Annual Symposium of the Pacific Northwest Chapter of the AVS Science and Technology Society, Forest Grove, OR, September, 2006.

3. S.-Y. Han, **Y.-J. Chang**, Y.-W. Su, D.-H. Lee, J.-Y. Jung, N.-K. Park, S.-O. Ryu, T.-J. Lee and C.-H. Chang, "*Chemical Nanoparticle Deposition of Oxide Nanostructured Thin Films*", Poster Session, The 17th Annual Symposium of the Pacific Northwest Chapter of the AVS Science and Technology Society, Forest Grove, OR, September, 2006.

4. P. H. Mudgar, **Y.-J. Chang**, S.-Y. Han, A. A. Morrone, S.-O. Ryu and T.-J. Lee, C.-H. Chang, "*A Continuous Flow Microreactor for Chemical Bath Deposition*" Topic 4: Materials Aspects, Nanostructures and Nanoparticles, Poster Programme, The 9th International Conference on Microreaction Technology (IMRET), Potsdam/Berlin, Germany, September, 2006.

5. **Y.-J. Chang**, D.-H. Lee, G. S. Herman, C.-H. Chang, "*Inkjet Printing of Functional Micro- and Nanostructured Materials*", Symposium T5.13: Nanomanufacturing, The 2006 Materials Research Society (MRS) Spring Meeting, San Francisco, CA, April 2006.

6. **Y.-J. Chang**, D.-H. Lee, C.-H. Chang, D. T. Punsalan, G. S. Herman, "*Inkjet Printed Inorganic Channel Materials for Thin Film Transistors*", Symposia M8.6: Flexible and Printed Electronics, Photonics, and Biomaterials, The 2005 Materials Research Society (MRS) Fall Meeting, Boston, MA, November 2005.

7. **Y.-J. Chang,** P. H. Mudgar, D.-H. Lee, C.-H. Chang, S.-Y. Han, S.-O. Ryu and T.-J. Lee, "*Continuous Flow Microreactor for Chemical Bath Deposition*" 08000 MESD Poster Session, The 2005 American Institute of Chemical Engineers (AICHE) Annual Meeting, Cincinnati, OH, October 2005.

8. **Y.-J. Chang**, P. H. Mugdur, S-.Y. Han, A. A. Morrone, S. O. Ryu, T-J. Lee, and C.-H. Chang, "*Nanocrystalline CdS Thin Films Deposited by a Novel Continuous Flow Microreactor*" Poster Session, The 16th Annual Symposium of the Pacific Northwest Chapter of the AVS Science and Technology Society, Troutdale, OR, September, 2005.

9. Doo-Hyoung Lee, **Y.-J. Chang**, C.-H. Chang, and G. S. Herman," *Microcrystal Formation in a Microwave Oven*" Poster Session, The 16th Annual Symposium of the Pacific Northwest Chapter of the AVS Science and Technology Society, Troutdale, OR, September, 2005.

10. **Y.-J. Chang**, P. H. Mugdur, S-.Y. Han, A. A. Morrone, S. O. Ryu, T-J. Lee, and C.-H. Chang, "*Nanocrystalline CdS Thin Films Deposited by a Novel Continuous Flow Microreactor*" Poster Session, The 2005 Microscopy & Microanalysis Conference, Honolulu, HI, July 2005.

11. S.-Y. Han, D.-H. Lee, **Y.-J. Chang**, S.-O. Ryu, T.-J. Lee, and C.-H. Chang, "*Room Temperature Deposition of Nickel Oxide Thin Films by Chemical Bath Deposition*", The 2005 American Institute of Chemical Engineers (AICHE) Regional Conference, Corvallis, OR, April, 2005.

12. **Y.-J. Chang**, D.-H. Lee, P. H. Mudgar, S. O. Ryu, T-J. Lee, C.-H. Chang, "*Growth Kinetics of Thin Film Electronic Materials via Soft Solution Processes*", The 2004 American Institute of Chemical Engineers (AICHE) Annual Meeting, Austin, TX, November, 2004.

13. C.-H. Chang, **Y.-J. Chang**, D.-H. Lee, S. O. Ryu, T-J. Lee, "*Characterization and Application of Semiconductor Thin Films Deposited by Chemical Bath Deposition*", Microscopy and Microanalysis 2004, Savannah, GA, August, 2004.

14. **Y.-J. Chang**, D.-H. Lee, C. Munsee, J. F. Wager, S. O. Ryu, T-J. Lee, C.-H. Chang, "*Growth, Characterization, and Application of Semiconductor Thin Films Deposited by Chemical Bath Deposition*", Surface Analysis 04, Richland, WA, June 2004.

15. **Y.-J. Chang**, C. L. Munsee, J. Anderson, J. F. Wager, D. A. Keszler, G. S. Herman, and C.-H. Chang, "*Flexible CdS MISFETs Fabricated by Low Temperature Solution-based Deposition Technique*", The 12th Annual Graduate Student Conference, Oregon State University, Corvallis, OR, May 2004.

16. **Y.-J. Chang**, C. L. Munsee, J. Anderson, J. F. Wager, D. A. Keszler, G. S. Herman and C.-H. Chang, "*Flexible CdS MISFET Fabricated by Low Temperature Solution-based Deposition Technique*", Session I7.1: Flexible Materials and Device Technology II, The 2004 Materials Research Society (MRS) Spring Meeting, San Francisco, CA, April 2004.

17. **Y.-J. Chang**, C. Voss, D.-H. Lee, A. Massey, J. Kroon, S. O. Ryu, T.-J. Lee and C.-H. Chang, "*Chemical Bath Deposition: A Soft Solution Route to Electronics*", The 14th Annual Symposium of the Pacific Northwest Chapter of the American Vacuum Society (AVS), Troutdale, OR, September 2003.

18. **Y.-J. Chang**, C. Voss, S. Subramanian, S. O. Ryu, T.-J. Lee and C.-H. Chang, "*Growth Kinetics of Thin Film Cadmium Sulfide by Ammonia-Thiourea Based Chemical Bath Deposition*", The 11th Annual Graduate Student Conference, Oregon State University, Corvallis, OR, May 2003.

19. **Y.-J. Chang**, C. Voss, S. Subramanian, S. O. Ryu, T.-J. Lee and C.-H. Chang, "*Growth Kinetics of Thin Film Cadmium Sulfide by Ammonia-Thiourea Based Chemical Bath Deposition*". Symposia H1, Chemical Solution Deposition of Semiconducting and Non-Metallic Films, The 203rd Meeting of The Electrochemical Society (ECS), Paris, France, April 2003.

20. C. Voss, **Y.-J. Chang**, C.-H. Chang, S. Subramanian, "*Cadmium Sulfide Thin Film Transistors Fabricated by Low Temperature Chemical Bath Deposition*", The 13th Annual Symposium of the Pacific Northwest Chapter of the American Vacuum Society (AVS), Vancouver, WA, September 2002.